主論文

(2)

学位申請論文

Numerical and Theoretical Studies on Thermal Convection in a Rotating Annulus of Fluid

菅田 誠治

Contents

1 Introduction

1.1 Rotating annulus experiments

In the field of geophysical fluid dynamics, rotating annulus experiments have been done to investigate thermal convection in a rotating system (see, *e.g.*, Hide and Mason, 1975). The experiment is usually done as follows. Water or water–glycerol solution is filled as a working fluid into a container made of two coaxial cylinders and a thermally insulated bottom which is usually horizontal. A temperature difference between the cylinders is maintained and all of the system are rotated about the vertical axis of the cylinders at a constant rotation rate. A driven thermal convection is observed in a rotating frame with the system.

(a) (b) (c)

Figure 1: Surface flow patterns (Hide and Mason, 1975). (a) Axisymmetric flow, (b) steady wave, (c) irregular flow.

Generally, the flow observed in the experiment is classified into four regimes: steady axisymmetric flow, steady waves, vacillation, and irregular flow. Flow patterns at the top surface are shown in Fig. 1 for these regimes except for vacillation. Selection of the regime depends on several experimental parameters, such as the rotation rate Ω, the temperature difference between the cylinders ΔT, physical properties of the fluid, and the dimensions of the container. Fowlis and Hide (1965) listed all the physical variables and the dimensional experimental parameters required to specify the system in their Table 1 and defined a practical set of sixteen independent dimensionless parameters required to specify the system in their Table 2. The selection of the regime is usually described on a regime diagram which shows the dependence on two important dimensionless parameters: Taylor number (Ta) and thermal Rossby number (Ro_T). These numbers are defined as

$$Ta \equiv 4\Omega^2(b-a)^5/\nu^2 d, \tag{1}$$

$$Ro_T \equiv g d \alpha \Delta T/\Omega^2(b-a)^2, \tag{2}$$

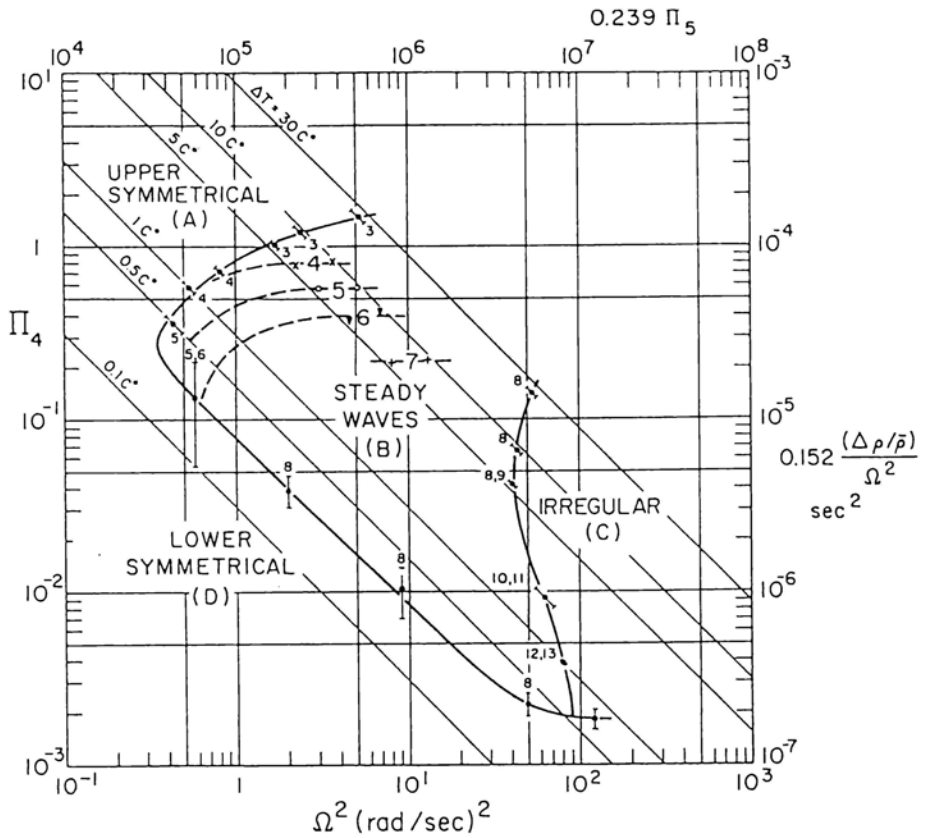

Figure 2: Typical regime diagram for water. $\Pi_4 = Ro_T$ and $\Pi_5 = Ta$ (Fowlis and Hide, 1965).

where a is the radius of the inner cylinder, b the radius of the outer cylinder, d the depth of the fluid, ν the kinematic viscosity, α the coefficient of volume expansion, and g the acceleration due to gravity.

Figure 2 is a well-known regime diagram for water obtained by Fowlis and Hide (1965). Steady axisymmetric flow, which is often called as the Hadley regime, occupies a region on the lefthand side of the anvil-shaped transition curve. The axisymmetric regime is subdivided into upper symmetric regime above the transition curve and lower symmetric regime below the curve. On the other hand, non-axisymmetric flow called as the Rossby regime occupies on the righthand side of the curve, where steady waves appear near the transition curve and vacillation and irregular flows appear at higher values of Ta.

In some experiments, a hysteresis phenomenon is observed at the regime transition between the axisymmetric flow and the steady wave; the criterion for the disappearance of an established flow differs from that for the onset of the flow. Hysteresis is also observed within the steady waves of different wavenumber. Hysteresis is interpreted as the result of presence of two or more stable solutions for the same experimental condition.

1.2 Theoretical and numerical studies

Fluid motion in a rotating annulus can be described by the Navier-Stokes equations for the Boussinesq fluid. A large number of theoretical (analytic) and numerical studies have

been done with the equations.

The analytic study is limited to the investigation of highly symmetric phenomena, such as the axisymmetric flow and linear stability analysis of the flow, because of mathematical difficulties of handling the equations. Hunter (1967) analytically obtained the axisymmetric flow in the lower symmetric regime assuming that the heat transfer is purely conductive. On the other hand, McIntyre (1968) analytically obtained the axisymmetric flow in the upper symmetric regime assuming the predominance of heat convection.

Regime transitions are essentially explained by instability of the flow. One flow regime gives way to another when the flow becomes unstable for perturbation at given external parameters. Linear stability analysis of a baroclinic basic state has been done to study the transition from the axisymmetric flow to the steady wave. Barcilon (1964) obtained the anvil-shaped transition curve by modifying the Eady problem with friction in the top and bottom boundary layers.

Numerical experiments are great help to study the result obtained in the laboratory experiments. A little discrepancy between the results in numerical experiments and those in the laboratory experiments exists owing to inevitable imperfection included in each experiment, such as finite difference approximations, Boussinesq approximations, limited number of grids, and neglect of the variation of the physical properties of the fluid with temperature in the former, and leak of the heat from the *insulated* top and bottom boundaries, fluctuation of the temperature at side boundaries, and distortion of the apparatus in the latter. However, the numerical experiments provide many data of the number of grids for each computed variable without suffering the disturbance due to measurement probes. This advantage outweighs the disadvantage mentioned above. Williams (1967a, b) investigated the axisymmetric flow by numerical time integrations of the two-dimensional nonlinear Navier-Stokes equations for Boussinesq fluid. He also studied the steady waves with a similar three dimensional model (Williams, 1969, 1971, 1972). Tokioka (1970) numerically investigated the linear stability of the axisymmetric flow obtained by the two-dimensional model and showed that the flow is unstable in the wave regime. Recently, Miller and Butler (1991) reproduced the hysteresis phenomenon by using a nonlinear semi-spectral model including zonal flow and a dominant wave. Ukaji and Tamaki (1990) simulated a tilted trough vacillation with a full three-dimensional model.

1.3 Purpose of this thesis

Understanding of the thermal convection in the rotating annulus of fluid provides a starting-point for understanding of the basic dynamics on the general circulation of the atmosphere, because both fluid motions in the experiment and in the atmosphere are essentially thermal convection due to horizontal differential heating under influence of the rotation of each system. Despite a large number of previous studies described in the preceding subsections, lots of subjects on the thermal convection in the rotating annulus

have not yet been solved, particularly on its nonlinear dynamics. Studies in this thesis were intended to investigate some of the unsolved subjects mainly by numerical approach to understand the thermal convection more deeply.

Transition of the flow regime is one of the most attractive and important subject on the thermal convection in the rotating annulus and has been discussed by a large number of analytic and numerical studies. Although the transition of solution has been investigated by stability and bifurcation analyses in some simplified systems of the rotating annulus of fluid, few numerical studies have been done on realistic flow systems in the rotating annulus. In section 3, stability of the axisymmetric flow is numerically investigated for highly viscous fluid. This part has appeared as a paper in the Journal of Fluid Mechanics (Sugata and Yoden, 1991). In section 4, stepwise transition from the axisymmetric flow to vacillation via steady waves is investigated numerically. This part has appeared as a paper in the Journal of the Meteorological Society of Japan (Sugata and Yoden, 1993a).

Individual flow regime, in itself, is also important to be understood. Fields of velocity, temperature, and pressure are balanced with each other in each steady flow depending on given external conditions. The flow transports momentum, heat, and so on, and these transports must be also consistent with the fields and the boundary conditions. In this thesis, heat transport is particularly focused because the horizontal temperature difference between the cylinders is essential to induce the flow. An attractive subject is to understand how much of heat is transported toward inward to keep balance with the flow fields and the boundary conditions at the walls. In section 5, dependence of the axisymmetric flow on the experimental parameters is numerically investigated, and a simple diagnostic model is constructed to understand the dependence intuitively. This part has appeared as a paper in the Journal of the Meteorological Society of Japan (Sugata and Yoden, 1992). In section 6, Lagrangian motion of a fluid particle is investigated in a steady wave solution, and a new interpretation of heat transport is proposed from a Lagrangian viewpoint. This part will be published in the Journal of the Meteorological Society of Japan.

2 Numerical models

The fluid motion in the rotating annulus can be described by the Navier-Stokes equations, the heat equation, and the continuity equation for Boussinesq fluid:

$$u_t + uu_r + \frac{vu_\lambda}{r} + wu_z - \frac{v^2}{r} - 2\Omega v = -p_r + \nu[\nabla^2 u - \frac{u}{r^2} - \frac{2v_\lambda}{r^2}] + \epsilon\frac{\rho}{\rho_0} r\Omega^2, \tag{3}$$

$$v_t + uv_r + \frac{vv_\lambda}{r} + wv_z + \frac{uv}{r} + 2\Omega u = -\frac{p_\lambda}{r} + \nu[\nabla^2 v - \frac{v}{r^2} + \frac{2u_\lambda}{r^2}], \tag{4}$$

$$w_t + uw_r + \frac{vw_\lambda}{r} + ww_z = -p_z + \nu\nabla^2 w - \frac{\rho}{\rho_0} g, \tag{5}$$

$$\theta_t + u\theta_r + \frac{v\theta_\lambda}{r} + w\theta_z = \kappa\nabla^2\theta, \tag{6}$$

$$\nabla \cdot \boldsymbol{u} = u_r + \frac{u}{r} + \frac{v_\lambda}{r} + w_z = 0, \tag{7}$$

$$\rho = \rho_0[1 - \alpha\Delta T\theta], \tag{8}$$

where

$$\nabla^2 = \frac{\partial^2}{\partial r^2} + \frac{1}{r}\frac{\partial}{\partial r} + \frac{1}{r^2}\frac{\partial^2}{\partial \lambda^2} + \frac{\partial^2}{\partial z^2},$$

(r, λ, z) are cylindrical coordinates, and t time. The corresponding velocity components are (u, v, w). Dimensionless temperature θ is defined as $\theta \equiv (T - T|_{\text{inner wall}})/\Delta T$, where T is the temperature and ΔT the imposed temperature difference between the inner and outer cylinders. Density is denoted by ρ, and p is pressure divided by the mean density ρ_0. Parameter ϵ is an index of the treatment of the centrifugal force term; the index was set as $\epsilon = 0$ in almost of previous numerical studies since the effect of the term is commonly negligible. However, computations with $\epsilon = 1$ are done in a part of this thesis to consider the effect. Physical parameters of the fluid, ν, κ and α, are assumed to be constant, where ν is the kinematic viscosity, κ the thermometric diffusivity, and α the coefficient of volume expansion of the fluid. All of these assumptions and approximations are justified as far as ΔT is not so large.

Three different numerical models were developed in this study by transforming the governing equations into a finite difference form with each approximation of different levels. The first one is a two-dimensional model for seeking the axisymmetric flow on the assumption that all variables do not depend on the azimuth λ (see Sugata and Yoden, 1991, 1992). Another one is a model for linear stability analysis, which examines the linear stability of the axisymmetric flow with respect to wave perturbations as an initial-value problem of the linearized perturbation equations (see Sugata and Yoden 1991). The analysis clarifies where the transition from axisymmetric flow to steady waves occurs. The last one is a three-dimensional semi-spectral model, in which zonal component, dominant wave, and its first harmonics are considered (see Sugata and Yoden, 1993a). The model can describe steady waves and some types of vacillation in addition to the axisymmetric flow. The set of these models almost covers phenomena observed in the rotating annulus of fluid from the axisymmetric flow to steady waves and partly to vacillation.

3 Transition from axisymmetric flow to steady waves for highly viscous fluid

Fein and Pfeffer (1976) did an experiment using two different fluids from popular working fluid, mercury ($Pr \equiv \nu/\kappa = 0.0246$) and silicone oil ($Pr = 63$), and obtained regime diagrams for each fluid. The shape of the transition curve for silicone oil is not an

anvil-shape but is rather independent of thermal Rossby number. It is believed that the Prandtl number Pr is the key parameter to explain this dependence of the transition curve on the working fluid. However, an anvil-shaped transition curve is obtained even for the parameters of silicone oil if we use the Barcilon's model. Fein and Pfeffer (1976) suggested the possibility that the slope of the geopotentials due to the centrifugal force, the effects of which are neglected in the Barcilon's model, plays a vital role. However, no numerical studies have yet been done to support their suggestion.

Transition from the axisymmetric regime to the wave regime for silicone oil was studied by a linear stability analysis of the steady axisymmetric flow with respect to wave perturbations. If the analysis is done with the centrifugal force term, which has been neglected in the previous numerical studies, the transition curve is similar to that obtained in the laboratory experiment. However, if the term is neglected, the transition curve is not similar, but it shows an anvil-shape. This difference indicates the importance of the centrifugal force in determining the transition curve for highly viscous fluids. A further numerical experiment shows that the centrifugal force term in the axisymmetric flow is important in obtaining a transition curve similar to the laboratory experiment for large ΔT while the term in the perturbation equations is important for small ΔT.

Moreover, it is pointed out that a dimensionless parameter $\nu^2(a+b)/8g(b-a)^4$, which equals the ratio of the centrifugal force to the gravity force divided by the Taylor number, is a fundamental parameter instead of the Prandtl number in describing the dependence of the shape of the transition curve on the working fluid.

4 Stepwise transitions from axisymmetric flow to vacillation

Some of the laboratory experiments show stepwise transitions of flow regimes from steady axisymmetric flow to vacillation via steady wave regime as the rotation rate increases. The transition from axisymmetric flow to wave regime was firstly investigated by Lorenz (1962) with a low-order model of a two-layer quasi-geostrophic fluid system. Lorenz (1963) modified the model to explore further transitions of regimes. Numerical solutions of vacillations and irregular flows were obtained by time integrations in addition to analytic solutions of axi-symmetric flows and steady waves in the low-order model. Detailed analysis of the regime transitions in Lorenz's model was done by Ghil and Childress (1987) with bifurcation theories. The sequence of bifurcations leads to solutions of increasing spatial and temporal complexity, as the simpler solutions lose their stability.

In this study, stepwise regime transitions was numerically investigated with the semi-spectral model, and the results were interpreted with bifurcation theories. The transition between axisymmetric flow and steady wave regime is characterized by hysteresis; the

criterion for the disappearance of an established steady wave differs from the criterion for the onset of the steady wave. Branch of the steady wave solution does not bifurcate from that of the axisymmetric flow at the point where the axisymmetric flow becomes unstable. Instead, the steady wave branch has another type of critical point (interpreted as a "limit point") at which it disappears. The transition from steady wave to vacillation is interpreted as a Hopf bifurcation; a periodically fluctuating solution bifurcates from the steady wave branch when the steady wave solution loses its stability.

5 Steady axisymmetric flow – Dependence of the flow on the experimental parameters –

Since the steady axisymmetric flow has the highest spatial symmetry in the flow regimes, the governing equations for the flow are simpler than those for other flow regimes and easier to handle because of its symmetry. Some analytic studies have been done with assuming the dominance of the conduction or the advection in heat transfer (Hunter, 1967 and McIntyre, 1968).

On the assumption that the heat transfer is purely conductive, Hunter (1967) analytically obtained the axisymmetric flow in the lower symmetric regime. The temperature field is primarily determined as a solution of the heat equation. Zonal flow is in the thermal wind balance with the temperature field in the interior region. The Ekman layer is formed in contact with the top and bottom boundaries, while the flow in the side boundary layers is determined as a balance among the viscosity, buoyancy, and Coriolis forces.

On the assumption that the convection is predominant in the heat transfer, on the other hand, McIntyre (1968) analyzed the axisymmetric flow in the upper symmetric regime. Flow in the top and bottom Ekman layers and in the side boundary layers is determined separately, if two integral constants on the temperature field and a constant on the circulation are given appropriately. In determining the constants, he used the thermal wind relation in the interior region and assumed that the top and bottom of the interior are isothermal, respectively.

These analytic studies dealt with the governing equations precisely with mathematical technique and obtained solutions corresponding well to the numerically obtained ones (Williams, 1967a,b). However, it is not easy to understand intuitively how the balance of the flow field is kept in each flow. In this study, therefore, a simple diagnostic model of the steady axisymmetric flow was constructed to understand intuitively how the velocity and temperature fields are determined for given external parameters. The model consists of three equations: the equation of the thermal wind relation, the equation relating the mass flux in the Ekman layers with the zonal velocity in the interior by the Ekman boundary

theory, and the equation for the heat flux across the annulus. The last equation is derived from the fact that the inward heat flux integrated from the bottom to the top at any radius must be equal in an equilibrium state, which equation has not been used in previous analytic studies. The model gives relationships between three important quantities characterizing the axisymmetric flow: intensity of the meridional circulation, intensity of the zonal flow and horizontal temperature difference in the interior. The model is applicable to both the conduction-dominated flow and convection-dominated flow, and explains qualitatively how the heat transport process is determined in each flow. The results of the three important quantities and total inward heat transport in the simple model agree well with those obtained in the full-nonlinear two-dimensional model for a wide range of external parameters.

6 Steady wave – Lagrangian motion and heat transport –

Detailed structure of the steady wave has been investigated numerically with several nonlinear models based on the Navier-Stokes equations for Boussinesq fluid (Williams, 1969, 1971, 1972, Ukaji and Tamaki, 1989). Williams (1972) showed that the structure of the steady wave is characterized by quasi-geostrophic and quasi-hydrostatic balances nearly everywhere and that the spatial structure is similar in some respects to that of a linear baroclinic wave of unstable two-dimensional axisymmetric flows. Inward heat transport in the steady wave, or the baroclinic annulus wave is commonly explained by correlation between a warm (cold) temperature and inward (outward) velocity in the azimuthal direction. It has been widely expected that heat is transported in every one cycle of the wavy motion in a jet stream; a particle in the jet stream obtains heat near the warm boundary, moves inward along the jet stream, releases the heat near the cold boundary, and moves outward again along the jet stream. However, no study has been done on the heat transport based on Lagrangian motion of particles in the steady wave.

In this study, Lagrangian motion of a fluid particle in a three-dimensional flow in the steady wave regime was computed for a long time interval. Obtained trajectory shows a chaotic nature but has several typical organized behavior depending on its position in the wavy flow. The annulus of fluid is divided into seven regions according to the particle behavior: an upper-level jet, a lower-level jet, a cyclonically trapped-region, an anticyclonically trapped-region, an inner boundary layer, an outer boundary layer, and a lower boundary layer. Cores of the cyclonically trapped-region and the anticyclonically trapped-region are found to be nearly isolated from the other regions.

Residence time of a fluid particle in each region and frequency of the transition between the regions were investigated. A cyclic route of transition which is remarkably

preferred was found: the outer boundary layer → the upper-level jet → the inner boundary layer → the lower-level jet *or* the lower boundary layer → the outer boundary layer.

Temperature of a fluid particle changes largely in both the inner boundary layer and the outer boundary layer during it has a large vertical motion. On the other hand, it changes little in the other regions, that is, temperature is nearly conserved following the Lagrangian motion. Lagrangian description of the horizontal heat transport in the steady wave is that a fluid particle which obtained heat during the upward motion in the outer boundary layer is advected nearly adiabatically across the interior region of the fluid and releases the heat during the downward motion in the inner boundary layer. Inward heat flux estimated from the Lagrangian description accounts for more than four-fifth of the total inward heat flux obtained in conventional Eulerian description.

7 Conclusions

In this thesis, thermal convection in the rotating annulus of fluid was investigated systematically from axisymmetric flow to vacillation mainly with numerical approaches and partly with analytic ones. Some new insights were obtained for problems which had not yet been solved by previous studies.

Numerical experiments were done on the transitions of flow regimes in sections 3 and 4 to assess the propriety of hypotheses in previous theoretical studies; some of them were justified and others were overthrown. As was suggested by the theoretical studies, it was clarified that the transition from the axisymmetric flow to the steady wave is largely influenced by the effect of the centrifugal force for highly viscous fluid. Moreover, stepwise transitions from axisymmetric flow to vacillation via steady wave were investigated with a three-dimensional numerical model and the present result shows that some previous results obtained by simplified system are spurious.

Individual flow field itself was investigated in sections 5 and 6. Clues to understanding each flow was to regard it as a heat transport system. Considering explicitly the heat transport in addition to the thermal wind balance in the interior and the Ekman boundary layers at the top and bottom boundaries gave us intuitive understanding of the balance kept in the axisymmetric flow for wide parameter ranges. Moreover, new interpretation of the heat transport was presented for a steady wave from Lagrangian viewpoint, which result is consistent with conventional knowledge of nearly adiabatic motion of particle in the quasi-geostrophic flow.

All of the studies in this thesis were made through intensive discussions with the author's supervisor, Dr. S. Yoden. Therefore, it is rather difficult to separate the author's original contribution in each study. However, most part of the simple diagnostic model in section 5 was developed by the author and basic idea on the Lagrangian description of the horizontal heat transport in section 6 was got by himself. All of the computation

were done by the author.

Acknowledgments

The author greatly wishes to thank Dr. S. Yoden for his persevering guidance. The author also wishes to thank Professor I. Hirota for his valuable comments and encouragement. Thanks are due to Drs. S. Sakai, M. Shiotani, K. Sato, and A. Numaguchi, and Mr. K. Ishioka, and colleagues in the author's previous and present affiliations for their helpful discussions and technical support.

References

Barcilon, V., 1964 : Role of the Ekman layers in the stability of the symmetric regime obtained in a rotating annulus. *J. Atmos. Sci.*, **21**, 291–299.

Fein, J. S. and R. L. Pfeffer, 1976 : An experimental study of the effects of Prandtl number on thermal convection in a rotating, differentially heated cylindrical annulus of fluid. *J. Fluid Mech.* **75**, 81–112.

Fowlis, W. W. and R. Hide, 1965 : Thermal convection in a rotating annulus of liquid: effect of viscosity on the transition between axisymmetric and non-axisymmetric flow regimes. *J. Atmos. Sci.*, **22**, 541–558.

Ghil, M. and S. Childress, 1987 : *Atmospheric dynamics, dynamo theory, and climate dynamics.* Springer-Verlag, 73–124.

Hide, R. and P. J. Mason, 1975 : Sloping convection in a rotating fluid. *Adv. in Phys.*, **24**, 47–100.

Hunter, C., 1967 : The axisymmetric flow in a rotating annulus due to a horizontally applied temperature gradient. *J. Fluid Mech.*, **27**, 753–778.

Lorenz, E. N., 1962 : Simplified dynamic equations applied to the rotating-basin experiments. *J. Atmos. Sci.*, **19**, 39–51.

Lorenz, E. N., 1963 : The mechanics of vacillation. *J. Atmos. Sci.*, **20**, 448–464.

McIntyre, M. E., 1968 : The axisymmetric convective regime for a rigidly bounded rotating annulus. *J. Fluid Mech.*, **32**, 625–655.

Miller, T. L. and K. A. Butler, 1991 : Hysteresis and the transition between axisymmetric flow and wave flow in the baroclinic annulus. *J. Atmos. Sci.*, **48**, 811–823.

Sugata, S. and S. Yoden, 1991 : The effects of centrifugal force on the stability of axisymmetric viscous flow in a rotating annulus. *J. Fluid Mech.*, **229**, 471–482.

Sugata, S. and S. Yoden, 1992 : Steady axi-symmetric flow due to differential heating in a rotating annulus and its dependence on experimental parameters. *J. Meteor. Soc. Japan*, **70**, 1005–1017.

Sugata, S. and S. Yoden, 1993a : A numerical study on regime transitions of the rotating annulus flow with a semi-spectral model. *J. Meteor. Soc. Japan*, **71**, 491–501.

Sugata, S. and S. Yoden, 1993b : Lagrangian motion and heat transport in a steady baroclinic annulus wave. submitted to *J. Meteor. Soc. Japan.*

Tokioka, T., 1970 : A stability of axisymmetric flows in a rotating annulus. *J. Meteor. Soc. Japan*, **48**, 293–314.

Ukaji, K. and K. Tamaki, 1989 : A comparison of laboratory experiments and numerical simulations of steady baroclinic waves produced in a differentially heated rotating fluid annulus. *J. Meteor. Soc. Japan*, **67**, 359–374.

Ukaji, K. and K. Tamaki, 1990 : A numerical study of tilted-trough vacillation observed in a differentially heated rotating fluid annulus. *J. Meteor. Soc. Japan*, **68**, 447–460.

Williams, G. P., 1967a : Thermal convection in a rotating fluid annulus: part 1. The basic axisymmetric flow. *J. Atmos. Sci.*, **24**, 144–161.

Williams, G. P., 1967b : Thermal convection in a rotating fluid annulus: part 2. Classes of axisymmetric flow. *J. Atmos. Sci.*, **24**, 162–174.

Williams, G. P., 1969 : Numerical integration of the three-dimensional Navier-Stokes equations for incompressible flow. *J. Fluid Mech.*, **37**, 727–750.

Williams, G. P., 1971 : Baroclinic annulus waves. *J. Fluid Mech.*, **49**, 417–449.

Williams, G. P., 1972 : The field distributions and balances in a baroclinic annulus wave. *Mon. Wea. Rev.*, **100**, 29–41.

The effects of centrifugal force on the stability of axisymmetric viscous flow in a rotating annulus

Seiji Sugata and Shigeo Yoden

J. Fluid Mech. (1991), *vol.* 229, *pp.* 471–482
Printed in Great Britain

The effects of centrifugal force on the stability of axisymmetric viscous flow in a rotating annulus

By SEIJI SUGATA AND SHIGEO YODEN
Department of Geophysics, Kyoto University, Kyoto 606, Japan

(Received 16 October 1990)

Axisymmetric flow in a rotating annulus with differential heating is computed for a high-kinematic-viscosity fluid, such as silicone oil, by numerical integration of the Navier–Stokes equations. Linear stability analysis of the steady axisymmetric flow with respect to a wave perturbation gives a transition curve from the axisymmetric regime to the wave regime; the transition curve is similar to that obtained experimentally by Fein & Pfeffer (1976). However, if we neglect the centrifugal force term, the transition curve is not similar, but it resembles the curve for water (a familiar 'anvil shape' in the regime diagram). A dimensionless parameter $\nu^2(a+b)/8g(b-a)^4$ (where a and b are the radii of the inner and outer cylinders, d the depth of the fluid, ν the kinematic viscosity, g the acceleration due to gravity), which equals the ratio of the centrifugal force to the gravity force divided by the Taylor number, is more fundamental than the Prandtl number in determining the shape of the transition curve.

1. Introduction

Rotating annulus experiments with horizontal differential heating have been done to investigate the fundamental dynamics of sloping convection (see e.g. Hide & Mason 1975). Several flow regimes appear, which depend mainly on the following dimensionless parameters: Taylor number ($Ta = 4\Omega^2(b-a)^5/\nu^2 d$), thermal Rossby number ($Ro_T = gd\alpha\,\Delta T/\Omega^2(b-a)^2$), Prandtl number ($Pr = \nu/\kappa$) and the aspect ratio ($\Gamma = (b-a)/d$), where a and b are the radii of the inner and outer cylinders, d the depth of the fluid, g the acceleration due to gravity, Ω the rotation rate of the annulus, ΔT the imposed radial temperature difference, α the coefficient of volume expansion of the fluid, κ the thermometric diffusivity, ν the kinematic viscosity. In a regime diagram plotted in the $(\log_{10} Ta, \log_{10} Ro_T)$-plane, axisymmetric flow is found outside the anvil-shaped region (broken line in figure 1) for the case of water ($Pr = 7.16$). Barcilon (1964) obtained the anvil shape for the transition curve separating the axisymmetric regime and the wave regime by adding top and bottom Ekman layers to Eady's baroclinic instability theory. Introduction of the Ekman-layer friction is necessary to obtain the lower axisymmetric regime at small Ta and small Ro_T.

Fein & Pfeffer (1976) did an experiment using two different fluids – mercury ($Pr = 0.0246$) and silicone oil ($Pr = 63$) – and obtained regime diagrams for each fluid. The shape of the transition curve for silicone oil is not an anvil shape, as shown by the heavy solid line in figure 1. It is believed that the Prandtl number is the key parameter to explain the difference between the transition curves. However, an anvil-shaped transition curve is obtained even for the parameters of silicone oil if we

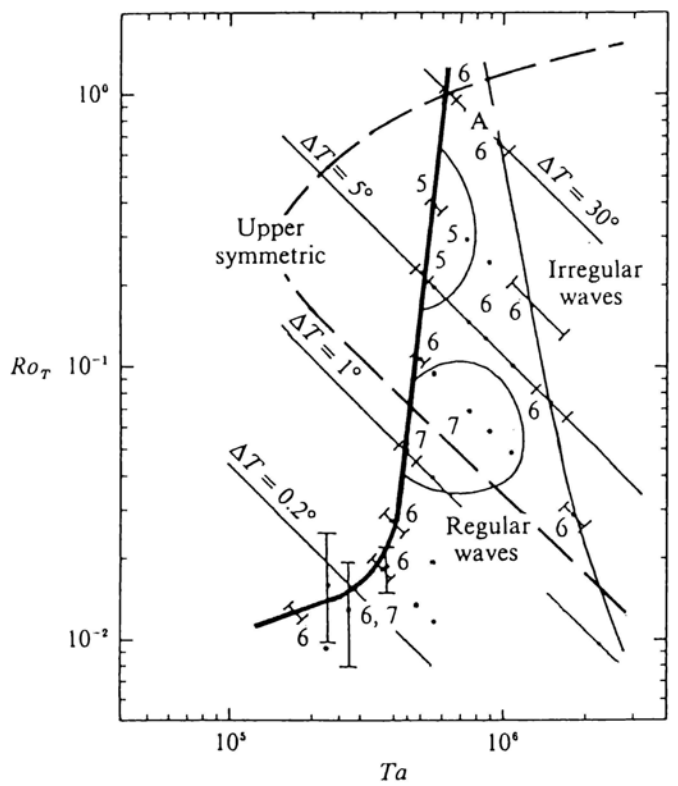

FIGURE 1. Regime diagram for silicone oil (after Fein & Pfeffer 1976). The broken line is the transition curve for water. The numbers indicate the wavenumbers observed in the laboratory experiment.

use Barcilon's model. Fein & Pfeffer suggested the possibility that the slope of the geopotentials due to the centrifugal force, the effects of which are neglected in Barcilon's model, plays a vital role. In the case of silicone oil, the centrifugal force must be about 30 times as large as that for water to get the same Taylor number, because the value of the kinematic viscosity of silicone oil is 5.4 times larger. In order to support their suggestion, they referred to some theoretical studies which take the effects of the slope of the geopotentials into account by sloping the top and bottom boundaries (Hide & Mason 1975). However, simplification and modification of the experimental situations leave some ambiguity.

In this study, we evaluate numerically the effects of the centrifugal force on the transition for silicone oil. We compute steady axisymmetric flow in a two-dimensional parameter space of (Ta, Ro_T) by time integration of two-dimensional nonlinear Navier–Stokes equations. Linear stability of the axisymmetric flow with respect to wave perturbations is examined as an initial-value problem of the linearized perturbation equations. A transition curve separating the axisymmetric regime and the steady-wave regime is obtained from these linear stability analyses. We then repeat the computation of the axisymmetric flow and the stability analysis without the centrifugal force term. Comparison of the results clarifies qualitative and quantitative differences due to the centrifugal force in an axisymmetric flow, the transition curve and the structure of unstable wave disturbances.

2. The model

The governing equations are

$$u_t + uu_r + \frac{vu_\lambda}{r} + wu_z - \frac{v^2}{r} - 2\Omega v = -p_r + \nu\left[\nabla^2 u - \frac{u}{r^2} - \frac{2v_\lambda}{r^2}\right] + \epsilon\frac{\rho}{\rho_0} r\Omega^2, \tag{1}$$

$$v_t + uv_r + \frac{vv_\lambda}{r} + wv_z + \frac{uv}{r} + 2\Omega u = -\frac{p_\lambda}{r} + \nu\left[\nabla^2 v - \frac{v}{r^2} + \frac{2u_\lambda}{r^2}\right], \tag{2}$$

$$w_t + uw_r + \frac{vw_\lambda}{r} + ww_z = -p_z + \nu\nabla^2 w - \frac{\rho}{\rho_0} g, \tag{3}$$

$$\theta_t + u\theta_r + \frac{v\theta_\lambda}{r} + w\theta_z = \kappa\nabla^2\theta, \tag{4}$$

$$\nabla\cdot\boldsymbol{u} = u_r + \frac{u}{r} + \frac{v_\lambda}{r} + w_z = 0, \tag{5}$$

$$\rho = \rho_0[1 - \alpha\,\Delta T\theta], \tag{6}$$

where

$$\nabla^2 = \frac{\partial^2}{\partial r^2} + \frac{1}{r}\frac{\partial}{\partial r} + \frac{1}{r^2}\frac{\partial^2}{\partial\lambda^2} + \frac{\partial^2}{\partial z^2},$$

(r, λ, z) are cylindrical coordinates, and t time. The corresponding velocity components are (u, v, w). Dimensionless temperature θ is defined as $\theta \equiv (T' - T'|_{\text{inner wall}})/\Delta T'$, where T' is the temperature and $\Delta T'$ the imposed temperature difference between the inner and outer cylinders. Density is denoted by ρ, and p is pressure divided by the mean density ρ_0. We modify the traditional Boussinesq approximation by retaining the density variation in the centrifugal force term in the radial momentum equation (1). Parameter ϵ is an index of the treatment of the centrifugal force term: $\epsilon = 1$ when we include the term in the computation, or $\epsilon = 0$ when we neglect it. Physical parameters of the fluid, ν, κ and α are assumed to be constant: $\nu = 5.5\times10^{-2}$ cm^2 s^{-1}, $\kappa = 8.8\times10^{-4}$ cm^2 s^{-1} and $\alpha = 1.05\times10^{-3}$ K^{-1} for silicone oil.

The size of the annulus and boundary conditions are the same as those in Fein & Pfeffer (1976). The dimensions are $a = 3.48$ cm, $b = 6.02$ cm and $d = 5.00$ cm. All four bounding surfaces are rigid and the surface of the fluid is in direct contact with the lid. The top and bottom boundaries are thermally insulating. The inner and outer walls are held at different constant temperatures, T_a and T_b ($T_a < T_b$), to maintain the difference ΔT.

The numerical method developed by Williams (1967*a*) is used to obtain the axisymmetric flow. A stream function $\psi(u = -(1/r)\psi_z,\ w = (1/r)\psi_r)$ and vorticity $\zeta(= -\{(1/r)\psi_{zz} + [(1/r)\psi_r]_r\})$ are introduced to describe the flow in the vertical (r, z)-plane. If we adopt the same notation for the finite difference as in Williams (1967*a*), the vorticity equation for the meridional circulation in finite-difference form is

$$\delta_t\zeta^t + J_A\left(\frac{\zeta}{r}\right) = -g\alpha\,\Delta T\delta_r\bar{\theta}^{rzz} + 2\Omega\delta_z v^z + \frac{1}{r}\delta_z\overline{(v^2)}^z + \nu\left[\delta_{zz}\zeta + \delta_r\left(\frac{1}{r}\delta_r(r\zeta)\right)\right]_{\text{lag}} - \epsilon r\Omega^2\alpha\,\Delta T\delta_z\bar{\theta}^z. \tag{7}$$

The last term is an additional term due to the centrifugal force; vertical stratification generates the vorticity. The computed flow is regarded as steady state when variables converge to satisfy the following condition:

$$\left(\frac{\sum_{\text{all grids}} (\partial\theta/\partial t)^2}{\sum_{\text{all grids}} \theta^2} \right)^{\frac{1}{2}} < 10^{-6}. \tag{8}$$

In the linear stability analysis, a small wave perturbation is added to the steady axisymmetric flow:

$$u(r, \lambda, z, t) = U(r, z) + u'(r, z, t)\, e^{im\lambda}, \tag{9}$$

with corresponding notation for v, w, p and θ. Substituting these into (1)–(5) and neglecting terms quadratic in the perturbation, we obtain linearized perturbation equations. Following Williams (1969), we integrate the perturbation equations for each wavenumber m with his staggered grid system. If perturbations of any wavenumber decay with time, the basic axisymmetric flow is stable. On the other hand, it is unstable if at least one of the perturbations grows.

The grid resolution is determined after a convergence test of the solutions. A resolution of 32(r-direction) $\times$ 64(z-direction) is adopted for $\Delta T \leqslant 5$ K and 64×128 for $\Delta T > 5$ K. These grids give equal grid intervals ($\Delta r = \Delta z$) because the aspect ratio of the annulus is 1:2.

We use the temperature difference ΔT and the rotation rate Ω as controllable experimental parameters, and plot the results on the (Ta, Ro_T)-plane (a familiar regime diagram like those in figure 1). The dimensional parameters ΔT and Ω are transformed into the dimensionless parameters Ta and Ro_T with the constants a, b, d, g, α and ν.

3. Results

First, we show the result for the case with the centrifugal force term ($\epsilon = 1$). Figure 2 shows an example of the steady axisymmetric flow of silicone oil obtained at the point marked A in figure 1, where $\Delta T = 30$ K and $\Omega = 5.5$ rad s^{-1} ($Ta = 8.46 \times 10^5$, $Ro_T = 0.791$). The stream function (figure 2a) shows strong meridional circulation in the boundary layers, which flows counterclockwise and transports heat inward. In the side boundary layers, the temperature field (figure 2b) has a large radial gradient and indicates 'the overshoot' of the temperature past its interior value as pointed out by McIntyre (1968). The zonal flow (figure 2c) also has a large vertical shear in the top and bottom boundary layers. In the interior, the meridional circulation is very weak, and the temperature and zonal flow are almost at the thermal wind balance: the buoyancy torque due to the radial temperature gradient is balanced by the Coriolis torque due to the vertical shear of the zonal flow.

Most of these characteristics of the axisymmetric flow are similar to the results for water. Figure 3 is the steady axisymmetric flow for water at the same Ta and Ro_T as in figure 2 ($\Delta T = 5.16$ K and $\Omega = 1.01$ rad s^{-1} for the same annulus). Here the physical parameters of water are: $\nu = 1.01 \times 10^{-2}$ cm^2 s^{-1}, $\kappa = 1.41 \times 10^{-3}$ cm^2 s^{-1} and $\alpha = 2.06 \times 10^{-4}$ K^{-1}. The meridional circulation and the zonal flow are qualitatively similar to those for silicone oil (figure 2). Quantitatively, the intensity of the meridional circulation for silicone oil is about twice that for water. The maximum value of the zonal flow is also about twice as large. Moreover, the thickness of the side

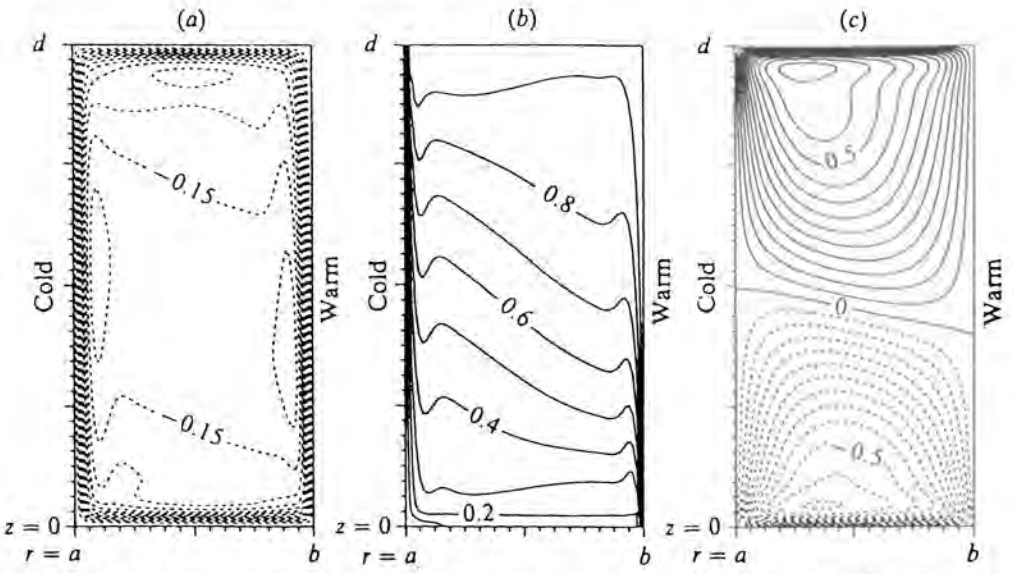

FIGURE 2. Steady axisymmetric flow for silicone oil at $\Delta T = 30$ K and $\Omega = 5.5$ rad s^{-1} ($Ta = 8.46 \times 10^5$, $Ro_T = 0.791$): (*a*) stream function of meridional circulation (cm^3 s^{-1}), (*b*) normalized temperature and (*c*) zonal velocity (cm s^{-1}). The centrifugal force term is retained in the computations.

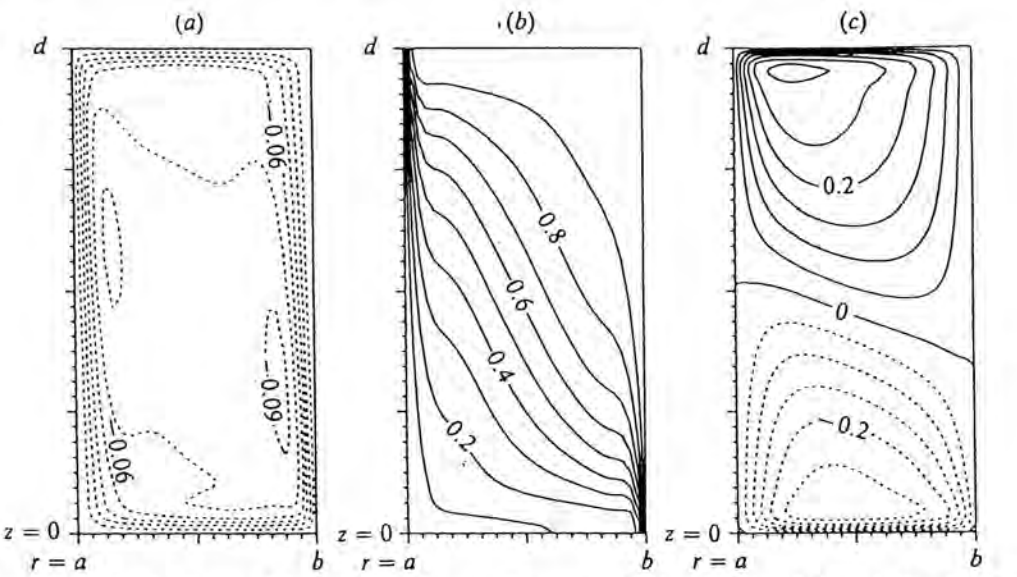

FIGURE 3. As in figure 2 but for water at the same Ta ($= 8.46 \times 10^5$) and Ro_T ($= 0.791$), or $\Delta T = 5.16$ K and $\Omega = 1.01$ rad s^{-1}.

boundary layers for water is 1.5–2 times larger than that for silicone oil, although the thickness of the top and bottom boundary layers is almost the same. These are consistent with McIntyre's (1968) estimation of the thickness of the boundary layers: the thickness of the side boundary layers is proportional to $(\nu\kappa/\alpha\,\Delta T)^{\frac{1}{4}}$, and the ratio is 1 : 1.72 for the present comparison between silicone oil and water. For the top and bottom boundary layers, on the other hand, the thickness of the Ekman layer is proportional to $(\nu/\Omega)^{\frac{1}{2}}$, and has the same value for silicone oil and water at the same Taylor number. In the temperature field, the slope of the isotherms in the interior for water is larger than that for silicone oil. Moreover, there is no 'overshoot' of the temperature for water because of the weaker meridional circulation. These characteristics of the temperature field reflect the relative importance of convective

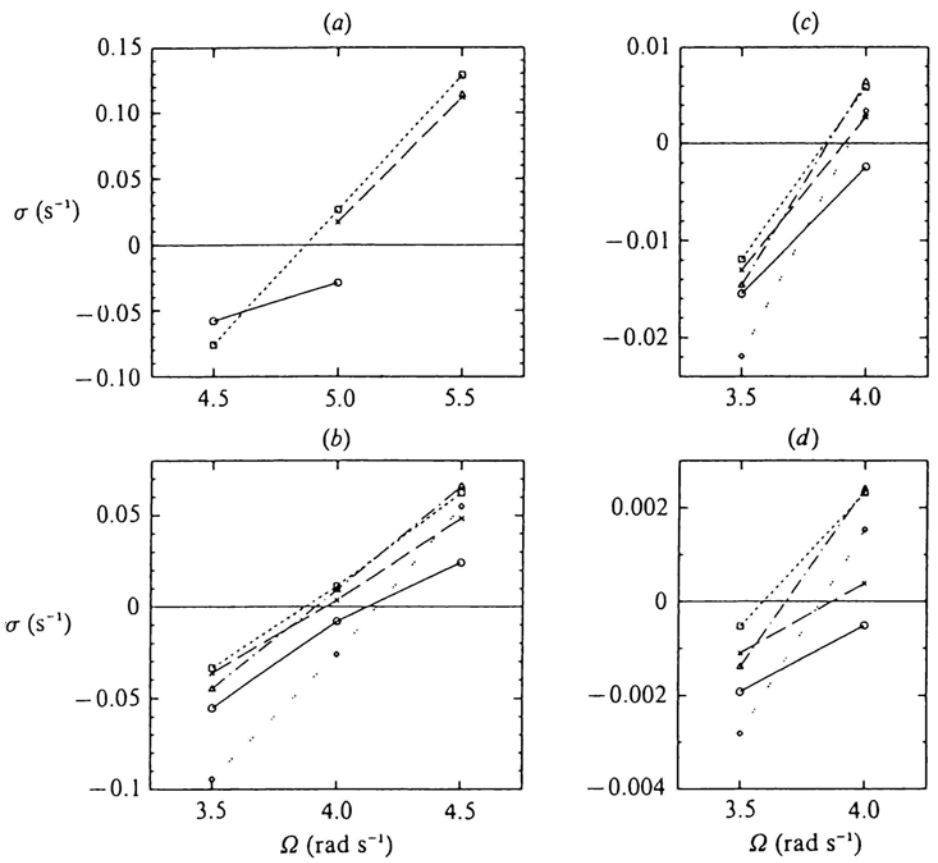

FIGURE 4. Growth rates of wave perturbations as a function of the rotation rate Ω. (*a*) $\Delta T = 30$ K, (*b*) $\Delta T = 5$ K, (*c*) $\Delta T = 1$ K and (*d*) $\Delta T = 0.2$ K. ——○, $m = 4$; — — −×, $m = 5$; ------□, $m = 6$; —·—··△, $m = 7$; ·· ··◇, $m = 8$.

and conductive transport of heat (Williams 1967*b*). However, the question of how the temperature distribution is determined for a given external condition remains.

Steady axisymmetric flows are computed for several values of Ω at $\Delta T = 30$ K, 5 K, 1 K and 0.2 K. The lines of constant ΔT are the diagonal ones sloping from upper left to lower right in figure 1. A linear stability analysis is done for each steady flow. Time integration of the perturbation equations gives an averaged growth rate σ (s^{-1}) during the time interval $[t_1, t_2]$:

$$\sigma \equiv \frac{\log\left(E(t_2)/E(t_1)\right)}{t_2 - t_1}, \tag{10}$$

where $E(t)$ is the kinetic energy of the wave perturbation. In this study, σ is calculated after $\partial E(t)/\partial t$ has attained an almost constant value (or oscillates around a constant value) for more than 30 s.

The growth rate for each wavenumber as a function of the rotation rate Ω is shown in figure 4 for (*a*) $\Delta T = 30$ K, (*b*) 5 K, (*c*) 1 K and (*d*) 0.2 K. In each figure, the growth rate σ increases with Ω and $\partial\sigma/\partial\Omega$ increases with the wavenumber m. With a linear interpolation, we can determine a transition point Ω_0 at which one of σ values becomes positive with increasing Ω. For example, in figure 4(*a*), the axisymmetric flow becomes unstable for the perturbation with $m = 6$ at $\Omega_0 = 4.85$ rad s^{-1}. The absolute value of σ and $\partial\sigma/\partial\Omega$ become large for large ΔT (note that the scale of the ordinate is different among figures 4(*a*)–4(*d*).

We obtain a transition curve joining the transition points in the regime diagram shown in figure 5. The transition curve is very close to the curve obtained

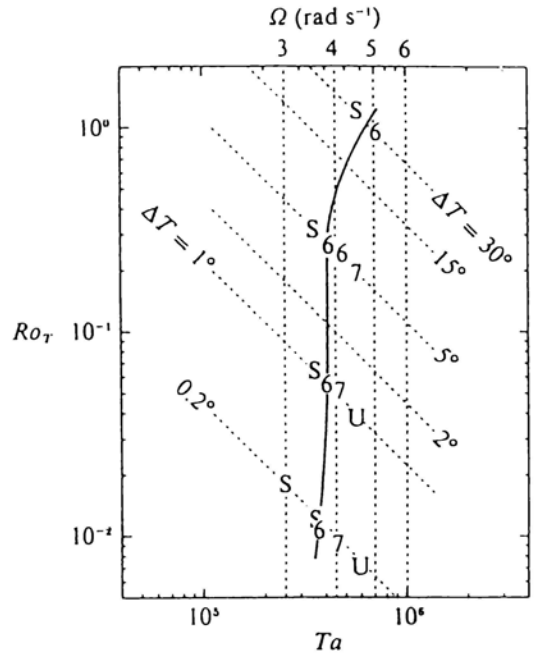

FIGURE 5. Transition curve between the axisymmetric regime and the wave regime obtained from the linear stability analysis. S indicates that the basic flow is stable for perturbations for all wavenumbers computed at the point and U indicates that it is unstable for at least one of the wave perturbations. Each number indicates the most unstable wavenumber.

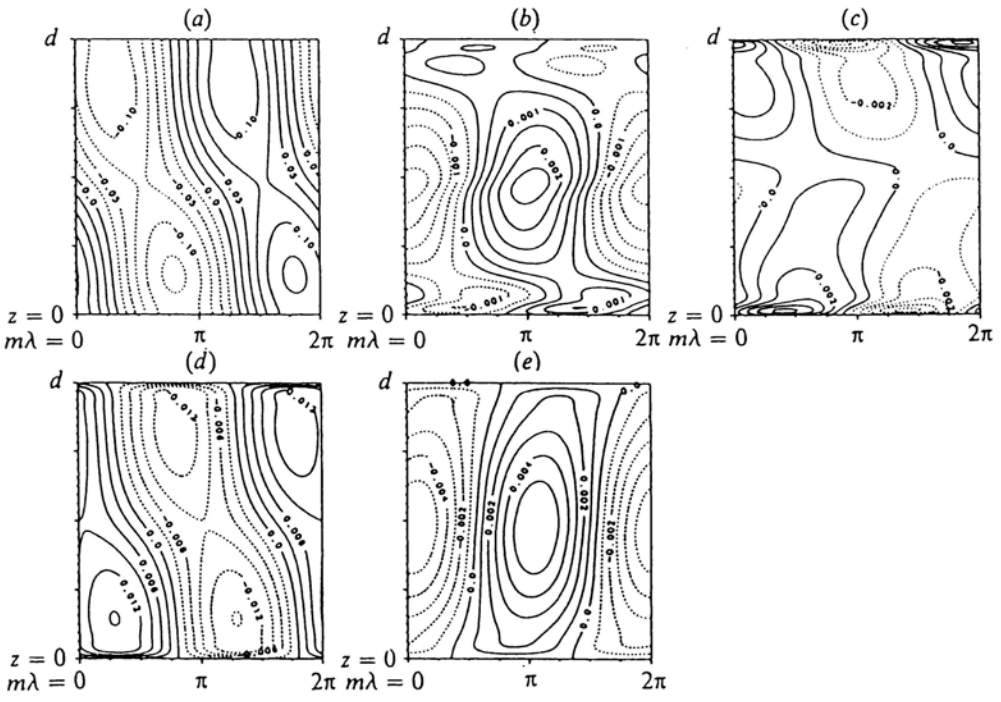

FIGURE 6. Vertical section of the most unstable wave perturbation ($m = 6$) at $(r-a)/(b-a) = 0.5$ for $\Delta T = 30$ K and $\Omega = 5.5$ rad s^{-1}: (*a*) pressure, (*b*) temperature, (*c*) zonal velocity, (*d*) radial velocity and (*e*) vertical velocity.

experimentally for silicone oil (figure 1) except for the region where $\Delta T \leqslant 0.2$ K. The perturbation that destabilizes the axisymmetric flow at the transition point has the same wavenumber as observed in the laboratory experiment near the transition curve (figure 1).

The structure of an unstable perturbation is shown in figure 6, which is a vertical-zonal section at the mean radius of the annulus for $m = 6$ at $\Delta T = 30$ K and $\Omega =$

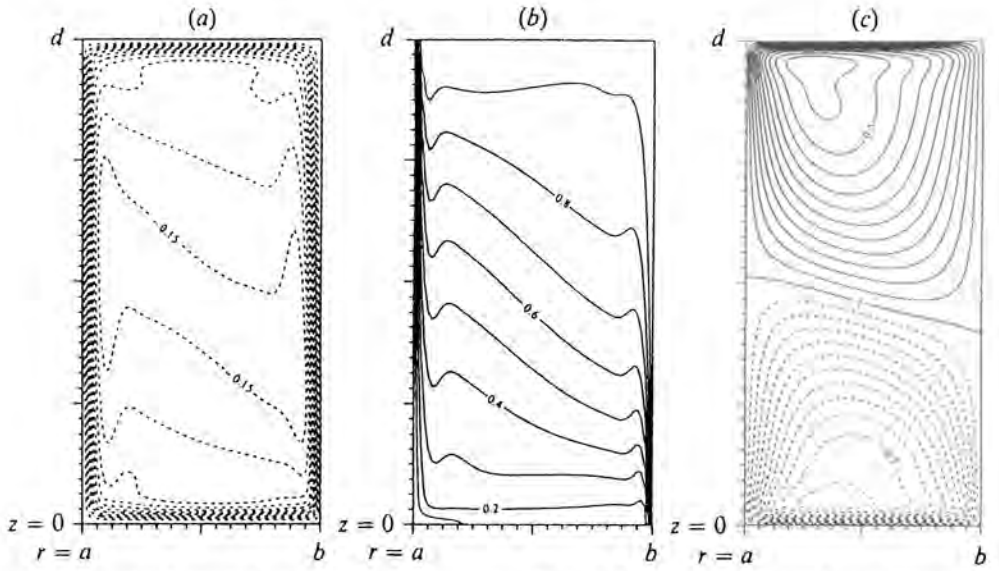

FIGURE 7. As in figure 2 except that the centrifugal force term is neglected in computations.

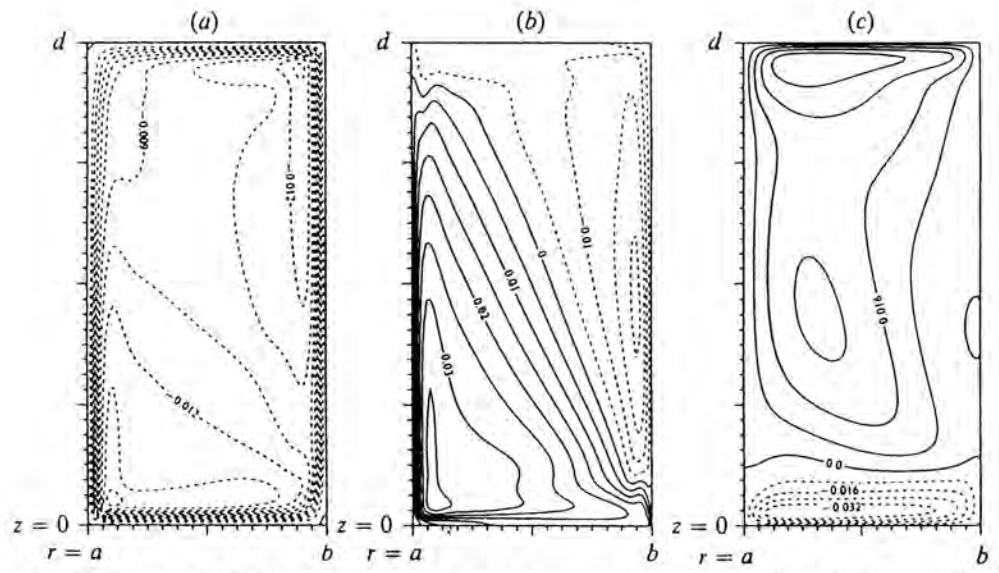

FIGURE 8. Difference of the two steady axisymmetric flows at $\Delta T = 30$ K and $\Omega = 5.5$ rad s^{-1} subtracting the value in figure 7 from that in figure 2. (*a*) Stream function, (*b*) normalized temperature and (*c*) zonal velocity. Units are the same as in figure 2.

5.5 rad s^{-1}. Mutual phase relations of the variables are similar to those obtained for water (Tokioka 1970). The structure is basically that of Eady's wave. However, there is disorder of the structure near the top and bottom boundaries, particularly in the temperature field (figure 6*b*) and the zonal velocity field (figure 6*c*). The disorder near the boundaries is small for small ΔT.

In order to investigate the dynamical role of the centrifugal force, we did a calculation neglecting the centrifugal force term ($\epsilon = 0$). Figure 7 shows the steady axisymmetric flow under the same external conditions as in figure 2 ($\Delta T = 30$ K, $\Omega = 5.5$ rad s^{-1}). The two axisymmetric flows for $\epsilon = 0$ and $\epsilon = 1$ are similar to each other: the difference, shown in figure 8, is less than 10%. In the case of $\epsilon = 1$, the radial gradient of temperature is weaker and the vertical shear of the zonal velocity is larger. These differences in the temperature and the zonal velocity can be understood by a torque balance in the interior region. When $\epsilon = 0$, the buoyancy

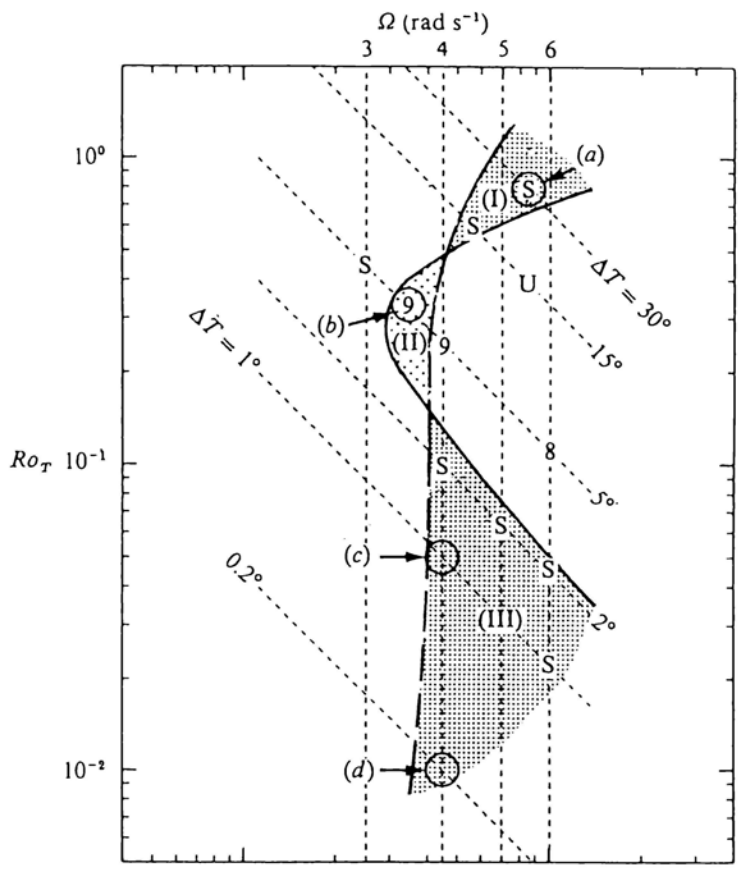

FIGURE 9. As in figure 5 except that the centrifugal force term is neglected in the analysis. The broken line is the transition curve for the case with the centrifugal term (taken from figure 5).

torque (anticlockwise in the (r, z)-plane) is balanced with the Coriolis torque (clockwise). When $\epsilon = 1$, the vertical difference of the centrifugal force due to the density stratification makes an anticlockwise torque. To compensate for the centrifugal torque, it is necessary that the thermally driven torque becomes small and/or the Coriolis torque becomes large.

A linear stability analysis of the axisymmetric flows under $\epsilon = 0$ gives a transition curve for the case without the centrifugal force (solid line in figure 9). The transition curve has an anvil shape similar to that for water, but its position shifts to large Taylor number compared with that for water (broken line in figure 1). The curve intersects the transition curve for $\epsilon = 1$ (broken line in figure 9) twice. There are three regions where the stability of the axisymmetric flow is different for the cases of $\epsilon = 0$ and $\epsilon = 1$ (shaded regions (I), (II) and (III) in figure 9). In regions (I) and (III), the basic flow is unstable for $\epsilon = 1$ and stable for $\epsilon = 0$. On the other hand, in region (II), it is stable for $\epsilon = 1$ and unstable for $\epsilon = 0$. The structure of unstable wave perturbations is not very different for $\epsilon = 1$ and $\epsilon = 0$.

We further investigate the role of the centrifugal force terms in the equations for axisymmetric flows and wave perturbations. Two additional linear stability analyses are done in the three regions in figure 9: one is a stability analysis of the basic axisymmetric flow with $\epsilon = 1$ to a wave perturbation with $\epsilon = 0$; and the other is an analysis of the basic flow with $\epsilon = 0$ to a perturbation with $\epsilon = 1$. Table 1 show the result for all these combinations of ϵ in the analyses at the four points (a)–(d) in figure 9. At the two points (a) and (b) in regions (I) and (II), the stability depends on the

(a) $\Delta T = 30$ K, $\Omega = 5.5$ rad s^{-1}
$Ta = 8.46 \times 10^5$, $Ro_T = 0.791$

	Linear stability	
Basic flow	$\epsilon = 1$	$\epsilon = 0$
$\epsilon = 1$	unstable	unstable
$\epsilon = 0$	stable	stable

(b) $\Delta T = 5$ K, $\Omega = 3.5$ rad s^{-1}
$Ta = 3.43 \times 10^5$, $Ro_T = 0.326$

	Linear stability	
Basic flow	$\epsilon = 1$	$\epsilon = 0$
$\epsilon = 1$	stable	stable
$\epsilon = 0$	unstable	unstable

(c) $\Delta T = 1$ K, $\Omega = 4.0$ rad s^{-1}
$Ta = 4.47 \times 10^5$, $Ro_T = 4.98 \times 10^{-2}$

	Linear stability	
Basic flow	$\epsilon = 1$	$\epsilon = 0$
$\epsilon = 1$	unstable	stable
$\epsilon = 0$	unstable	stable

(d) $\Delta T = 0.2$ K, $\Omega = 4.0$ rad s^{-1}
$Ta = 4.47 \times 10^5$, $Ro_T = 9.97 \times 10^{-3}$

	Linear stability	
Basic flow	$\epsilon = 1$	$\epsilon = 0$
$\epsilon = 1$	unstable	stable
$\epsilon = 0$	unstable	stable

TABLE 1. Results of the stability analysis for combinations of ϵ between the computation of the axisymmetric flow and the linear stability analysis

basic axisymmetric flow. The centrifugal force term in the perturbation equations does not change the stability. As shown in figures 2 and 7, the two basic flows for (a) are very similar to each other but the small difference results in different stability; the basic flow in figure 2 is unstable while that in figure 7 is stable. On the other hand, at (c) and (d) in region (III), the stability depends on the perturbation equations. The centrifugal force term in the basic axisymmetric flow does not change the stability. For large ΔT the centrifugal force term in the basic axisymmetric flow is important in obtaining a transition curve similar to the experiment, while that term in the perturbation equations is important for small ΔT.

4. Discussion

The centrifugal force term has been neglected in previous numerical studies for water (e.g. Williams 1967a, b; Tokioka 1970). Since the centrifugal acceleration is much smaller than the gravitational acceleration, it is justified to neglect the centrifugal force term in numerical studies for water. However, in this study, we clarified that the term is necessary for a stability analysis of fluid with large kinematic viscosity. Although it is believed that the Prandtl number is the key parameter, it is not the most appropriate parameter to describe the difference in the shape of the transition curves for water and silicone oil. A transition curve with an anvil shape could be obtained even for fluids with high Prandtl number, if the kinematic viscosity is similar to that of water but the thermometric diffusivity is very small.

Instead of the Prandtl number, a relevant dimensionless parameter is $\Pi_3 = \Omega^2(b^2-a^2)/2gd$ (see table 2 in Fowlis & Hide 1965). The parameter Π_3 is the ratio of the centrifugal force term to the pressure gradient term when we do a scale analysis by assuming geostrophy. In other words, Π_3 is the ratio of the centrifugal acceleration to the gravitational acceleration (multiplied by the aspect ratio). If we illustrate the regime diagrams for different fluids in the three-dimensional parameter space (Ta, Ro_T, and a third parameter), as figure 21 in Fein & Pfeffer (1976), it is more appropriate to introduce a dimensionless parameter $\nu^2(a+b)/8g(b-a)^4\,(=\Pi_3/Ta)$ as

the third parameter, because this parameter depends only on the fluid and the apparatus (on the other hand, Π_3 depends on Ω). Note that, even for water, large mean radius of the annulus would produce the same effect as for a highly viscous fluid.

5. Conclusion

We have done a numerical experiment for sloping convection in a rotating annulus with a highly viscous fluid, such as silicone oil. The centrifugal force terms were retained in the computation because these are not negligibly small for silicone oil. The axisymmetric flows obtained are qualitatively similar to those for water. However, the intensity of the meridional circulation and the zonal flow is larger than that for water at the same Ta and Ro_T, while the slope of isotherms in the interior is smaller. A linear stability analysis of the axisymmetric flows with a wave perturbation gives a transition curve similar to that obtained in the laboratory experiment. Moreover, the unstable wavenumber on the transition curve in the linear stability analysis corresponds to that obtained in the laboratory experiment.

Experiments without the centrifugal force term were done to investigate the dynamical role of the term. Axisymmetric flow without the centrifugal force term is not very different from that with the term. However, the transition curve obtained has an anvil shape similar to that for water with low viscosity. The difference in the shape of the transition curve is caused only by a change of the treatment of the centrifugal force term, namely the inclination of the geopotentials due to the centrifugal force strongly affects stability property of the axisymmetric flows. The centrifugal force term must be retained in studying the dynamics of high-kinematic-viscosity fluid.

We further investigated the role of the centrifugal force term in the axisymmetric flow and in the wave perturbation separately. For large ΔT, the centrifugal force term in the axisymmetric flow is important in obtaining a transition curve similar to the laboratory experiment. On the other hand, the term in the perturbation equations are important for small ΔT.

Fein & Pfeffer (1976) pointed out that the regime diagram depends on the working fluid. Our numerical experiments show the importance of the centrifugal force in determining the transition curve for highly viscous fluids. If we illustrate the regime diagrams for different fluids in the three-dimensional parameter space of the Taylor number, the thermal Rossby number and the third parameter, it is more appropriate to use a dimensionless parameter $\nu^2(a+b)/8g(b-a)^4$ ($= \Pi_3/$Taylor number) as the third parameter instead of the Prandtl number.

The authors wish to thank Professor I. Hirota and Dr S. Sakai for their valuable comments during the work. This work was supported in part by Grant-in-Aid for Scientific Research from the Ministry of Education.

REFERENCES

Barcilon, V. 1964 Role of the Ekman layers in the stability of the symmetric regime obtained in a rotating annulus. *J. Atmos. Sci.* **21**, 291–299.

Fein, J. S. & Pfeffer, R. L. 1976 An experimental study of the effects of Prandtl number on thermal convection in a rotating, differentially heated cylindrical annulus of fluid. *J. Fluid Mech.* **75**, 81–112.

FOWLIS, W. W. & HIDE, R. 1965 Thermal convection in a rotating annulus of liquid: effect of viscosity on the transition between axisymmetric and non-axisymmetric flow regimes. *J. Atmos. Sci.* **22**, 541–558.

HIDE, R. & MASON, P. J. 1975 Sloping convection in a rotating fluid. *Adv. Phys.* **24**, 47–100.

MCINTYRE, M. E. 1968 The axisymmetric convective regime for a rigidly bounded rotating annulus. *J. Fluid Mech.* **32**, 625–655.

TOKIOKA, T. 1970 A stability of axisymmetric flows in a rotating annulus. *J. Met. Soc. Japan* **48**, 293–314.

WILLIAMS, G. P. 1967*a* Thermal convection in a rotating fluid annulus: part 1. The basic axisymmetric flow. *J. Atmos Sci.* **24**, 144–161.

WILLIAMS, G. P. 1967*b* Thermal convection in a rotating fluid annulus: part 2. Classes of axisymmetric flow. *J. Atmos Sci.* **24**, 162–174.

WILLIAMS, G. P. 1969 Numerical integration of the three-dimensional Navier–Stokes equations for incompressible flow. *J. Fluid Mech.* **37**, 727–750.

Steady axi-symmetric flow due to differential heating in a rotating annulus and its dependence on experimental parameters

Seiji Sugata and Shigeo Yoden

Steady Axi-symmetric Flow due to Differential Heating in a Rotating Annulus and Its Dependence on Experimental Parameters

By Seiji Sugata and Shigeo Yoden

Department of Geophysics, Kyoto University, Kyoto 606-01, Japan
(Manuscript received 30 April 1992, in revised form 18 August 1992)

Abstract

Steady axi-symmetric flow in a rotating annulus with differential heating is computed with a high-resolution full-non-linear model in two dimensions. The velocity and temperature fields are investigated for a wide range of external parameters, and their dependence on the parameters is discussed.

A simple diagnostic model of the steady axi-symmetric flow is constructed to understand intuitively how the velocity and temperature fields are determined for given external parameters. The model is applicable to both the conduction-dominated flow and convection-dominated flow, and explains qualitatively how the heat transfer process is determined in each flow. Moreover, the model gives several important quantities characterizing the axi-symmetric flow, such as the intensity of the meridional circulation, that of the zonal flow and the horizontal temperature difference in the interior, for a wide range of the parameters. The results in the simple model agree well with those obtained in the full-non-linear model.

1. Introduction

Schneider and Lindzen (1977) studied axi-symmetric flows on a rotating sphere driven by radiation and heat sources due to cumulus convection using a linearized numerical model. They showed that the cumulus heating and friction drive an axi-symmetric meridional circulation in the tropics comparable to the observed Hadley cell circulation. Schneider (1977) introduced a simple approximation to evaluate the intensity and the meridional extent of the Hadley circulation. Held and How (1980) explored Schneider's approach in a wide range of parameters and showed that detailed numerical results could be replicated by the application of some simple balances for the zonal angular momentum and the thermal energy. These studies of axi-symmetric flow give fundamental insights into the nature of the general circulation of the atmosphere.

Rotating annulus experiments with differential heating in the radial direction have been done to understand the basic dynamics of the general circulation of the atmosphere (*e.g.*, Hide and Mason, 1975). Some of the essential factors which determine the general circulation of the atmosphere are included in the rotating annulus experiments, such as rotation, differential heating and gravity, although other factors, such as spherical geometry, surface topography and radiative cooling, are not. These exclusions of the factors make it easier to understand the basic dynamics of the thermal convection in a rotating fluid with the differential heating. In addition, the flow is more tractable over a wide range of experimental parameters and its pattern is more reproducible in the laboratory experiment.

Several régimes of flow are observed in the experiment; steady axi-symmetric flow, steady waves, vacillation and irregular flow. The axi-symmetric flow has the same spatial symmetry as the external forcing (the axi-symmetric heating), while other régimes have zonal (azimuthal) dependence. Selection of the régimes depends on the experimental parameters. On a régime diagram with a logarithm of Taylor number (Ta) as the abscissa and that of thermal Rossby number (Ro_T) as the ordinate, the axi-symmetric flow is found outside the anvil-shaped region (heavy solid line in Fig. 1) for the case of water (Fowlis and Hide, 1965). The axi-symmetric régime is divided into upper and lower symmetric régimes.

Some theoretical studies of the axi-symmetric flow in the experiment have been done with a top boundary condition of a rigid lid. Hunter (1967) analytically obtained the axi-symmetric flow in the lower symmetric régime, where both of Ta and Ro_T are

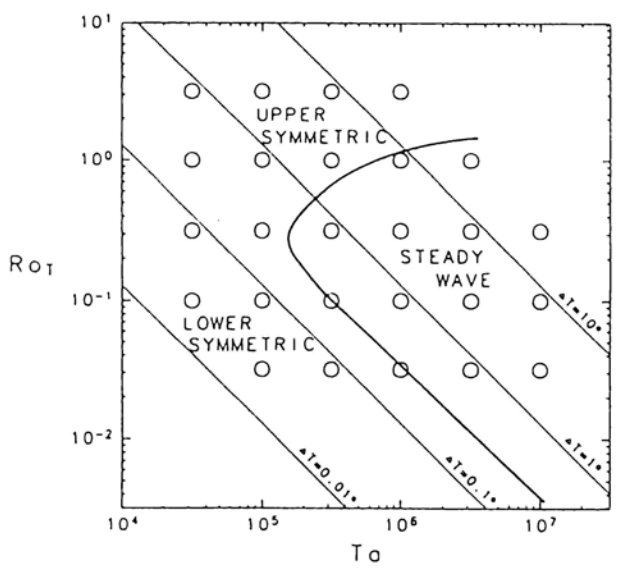

Fig. 1. Régime diagram obtained by Fowlis and Hide (1965) experimentally. The heavy solid line is the transition curve from an axi-symmetric flow régime to a wave régime. Circles indicate the points where axi-symmetric flows are computed.

small, on the assumption that the heat transfer is purely conductive. From this assumption, the temperature field is primarily determined as a solution of the thermal equation. In the interior region, zonal flow is in the thermal wind balance with the temperature field. On the other hand, viscosity plays an important rôle near the boundaries. The Ekman layer is formed in contact with the top and bottom boundaries, while the flow in the side boundary layers is determined as a balance among the viscosity, buoyancy, and Coriolis forces.

McIntyre (1968) analyzed the axi-symmetric flow in the upper symmetric régime on the assumption that the convection is predominant in the heat transfer. Flow in the top and bottom Ekman layers and in the side boundary layers is determined separately, if two integral constants on the temperature field and a constant on the circulation are given appropriately. In determining the constants, he used the thermal wind relation in the interior region and assumed that the top and bottom of the interior are isothermal, respectively. The flow he obtained is quantitatively similar to the numerical results of Williams (1967a, b), who computed the axi-symmetric flows at five points near the transition curve in the régime diagram by integrating the full-non-linear two-dimensional Navier-Stokes equations.

In this study, we compute steady axi-symmetric flows following Williams (1967a, b) for a wide range of the parameters, Ta and Ro_T, to investigate the velocity and temperature fields and their dependence on the parameters. The parameter range covers both the upper and lower symmetric régimes, and the wave régime as well. Although the axi-symmetric flow in the wave régime is unstable to wave perturbations (Lorenz, 1962, 1963), it is worth studying to understand the selection of flow régimes. It remains for our future study to compare such axi-symmetric solutions with wave solutions using the same parameters. Moreover, we construct a simple diagnostic model for the axi-symmetric flow in order to understand how the flow field is in equilibrium for given external parameters and how the heat transfer processes depend on the parameters. The simple model is applicable to both the conduction-dominated flow and the convection-dominated flow. Under the constraints of the heat balance, the momentum balance and the thermal wind balance, the model describes relationships among three variables which characterize the axi-symmetric flow: intensity of meridional circulation, zonal flow, and radial temperature difference across the interior. We investigate how the variables depend on the experimental parameters and to what degree their dependence agrees with those of the numerical results.

2. Non-linear steady solutions

We consider a fluid, water in this study, contained between two coaxial cylinders of inner and outer radii a and b, and two parallel horizontal planes of depth H. The dimensions are $a=3.48$ cm, $b=6.02$ cm and $H=5.00$ cm, which are the same as those in the laboratory experiment by Fowlis and Hide (1965). All four bounding surfaces are rigid and the surface of the fluid is in direct contact with the upper lid. The container rotates at a constant rate Ω. The inner and outer walls are held at different constant temperatures, T_a and T_b ($T_a<T_b$), to maintain the difference ΔT. The top and bottom boundaries are thermally insulating. Controllable experimental parameters are Ω and ΔT. Physical parameters of water are assumed to be constant: the kinematic viscosity, $\nu=1.01\times10^{-2}\,\mathrm{cm^2\,sec^{-1}}$; the thermometric conductivity, $\kappa=1.41\times10^{-3}\,\mathrm{cm^2\,sec^{-1}}$; the coefficient of volume expansion, $\alpha=2.06\times10^{-4}\mathrm{K^{-1}}$. Traditionally the following non-dimensional parameters have been used for the study of rotating annulus experiments: Taylor number, $Ta=4\Omega^2(b-a)^5/\nu^2H$; thermal Rossby number, $Ro_T=gH\alpha\Delta T/\Omega^2(b-a)^2$; Prandtl number, $Pr=\nu/\kappa$; and the aspect ratio $\Gamma=(b-a)/H$, where g is the acceleration of the gravity.

The numerical method described in Sugata and Yoden (1991) is used to obtain steady axi-symmetric flows. The method is basically the same as that in Williams (1967a), except for the modified Boussinesq approximation with an effect due to centrifugal force, although this effect is negligibly small in the present study. The number of grid points used in this study is 65 (horizontal direction) × 129 (verti-

cal direction). The flow is regarded as steady state when variables converge to satisfy the following condition:

$$\left(\frac{\sum_{\text{all grids}}(\partial\theta/\partial t)^2}{\sum_{\text{all grids}}\theta^2}\right)^{1/2} < 10^{-6}.$$

The time required to converge is 30 minutes in physical time at the most. The obtained steady flow at one point in the parameter space is used as an initial condition for the next computation at a neighboring point.

Axi-symmetric flow is obtained for 26 cases at $Ta = 10^{4.5} \sim 10^{7}$ and $Ro_T = 10^{-1.5} \sim 10^{0.5}$ except for some points with unrealistically large or small values of ΔT, which are shown in the régime diagram of Fig. 1. The heavy solid line in the figure is the transition curve from the axi-symmetric flow régime to the wave régime (Fowlis and Hide, 1965). Although the curve was obtained in the experiment with a free surface, the transition curve for a rigid lid is expected to be similar to this curve, as shown by Tokioka (1970) theoretically. Therefore, nearly half of the axi-symmetric flows we obtained are expected to be unstable with respect to wave perturbations.

The spatial structure of the velocity field is shown in Figs. 2 and 3. Figure 2 shows streamfunctions of the meridional circulation for 26 cases; strong direct meridional circulation is confined in boundary layers and motion is weak in the interior region. The thickness of the top and bottom (Ekman) boundary layers depends on Ta and that of the side boundary layers mainly depends on ΔT. The intensity of the meridional circulation depends on both Ta and Ro_T; the circulation is intensive for large Ta and large Ro_T. (Note that the scaling factor is different among the cross sections and indicated above each one). As for the circulation in the interior, two secondary cells and a weak but clear indirect cell are observed for the cases of large Ta and small Ro_T. Two secondary cells are observed for the cases of medium and large Ro_T, and a single direct cell for the cases of small Ta. (See cases D1, A2 and C2 in Williams, 1967b.)

Figure 3 shows cross sections of the zonal velocity for 26 cases. For large Ta and large Ro_T, the zonal flow is strong, and therefore both vertical shear and horizontal shear are also large. (Again be careful of the scaling factor.) In each cross section, the maximum value of positive zonal flow near the top boundary is larger than that of negative zonal flow near the bottom, and the position of the former is closer to the inner wall than that of the latter. As Ta increases, positions of the extremes shift inward and slope of the zero line becomes large.

A couple of measures which characterize the intensity of the axi-symmetric flow are introduced; the maximum value of the streamfunction at the mean radius is used as a measure of the meridional circulation, and the maximum value of zonal velocity as a measure of its intensity. Quantitative dependence of these measures on the two parameters, Ta and Ro_T, is shown in Fig. 4. Isolines of the measure of meridional circulation (a) have negative gradient in the ($\log Ta$, $\log Ro_T$)-plane, which is less steep ($= -1/2 \sim -1/5$) than that of constant ΔT ($= -1$). The gradient increases with increasing Ta or increasing Ro_T. The intensity also increases as Ta and Ro_T increase, and the increment is roughly exponential of $\log Ta$ and $\log Ro_T$. (Note that the contour interval is in geometrical proportion.) As for the measure of the zonal flow (b), isolines have similar dependence but steeper gradient than those in (a). The gradient is nearly equal to that of constant ΔT for large Ro_T, while it is roughly $-1/2$ for small Ro_T.

Figure 5 shows normalized temperature fields for 26 cases; the normalized temperature is defined as $\theta = (T - T_a)/\Delta T$. The thermal structure largely depends on Ro_T. For example, slope of the isotherms in the interior is steep for small Ro_T, which is indicative of the predominance of heat conduction, while it is gentle for large Ro_T, indicative of the predominance of heat convection. Overshoot of the temperature near the side boundary layers at large Ro_T is also indicative of strong convection, or meridional circulation. For large Ro_T, the radial gradient of the temperature at the side boundaries is large, particularly in the upper part of the inner wall and the lower part of the outer wall. Therefore the radial heat flux at the walls is large for large Ro_T.

Quantitative characteristics of the heat transfer processes are shown in Fig. 6: (a) the Nusselt number Nu, which is defined as the ratio of the obtained total heat flux to the ideal purely-conductive heat flux, and (b) fraction of the real heat conduction to the total heat flux. The dependence of Nu on Ta and Ro_T is similar to that of the measure of the meridional circulation in Fig. 4a. That is, isolines have a gradient of $-1/3 \sim -1/4$ for small Ro_T in the ($\log Ta$, $\log Ro_T$)-plane, but $-1/2$ or steeper for large Ro_T. The magnitude of Nu has a nearly exponential increment with $\log Ta$ and $\log Ro_T$. Figure 6b shows the percentage of the conduction at the mean radius, which is less dependent on Ta than (a). It is large for small Ro_T, and the heat transfer is nearly conductive at $Ro_T = 10^{-1.5}$. On the other hand, convection is predominant at $Ro_T = 10^{0.5}$.

We also investigated the balance in the vorticity equation for the meridional circulation; each term of the vorticity equation (Eq. (7) in Sugata and Yoden (1991)) was computed in the meridional section for 26 cases (figures are not shown). The interior region of the fluid is almost in a thermal wind balance; the buoyancy torque due to radial gradient of the temperature is balanced with the Coriolis torque due to the vertical shear of the zonal flow. The interior

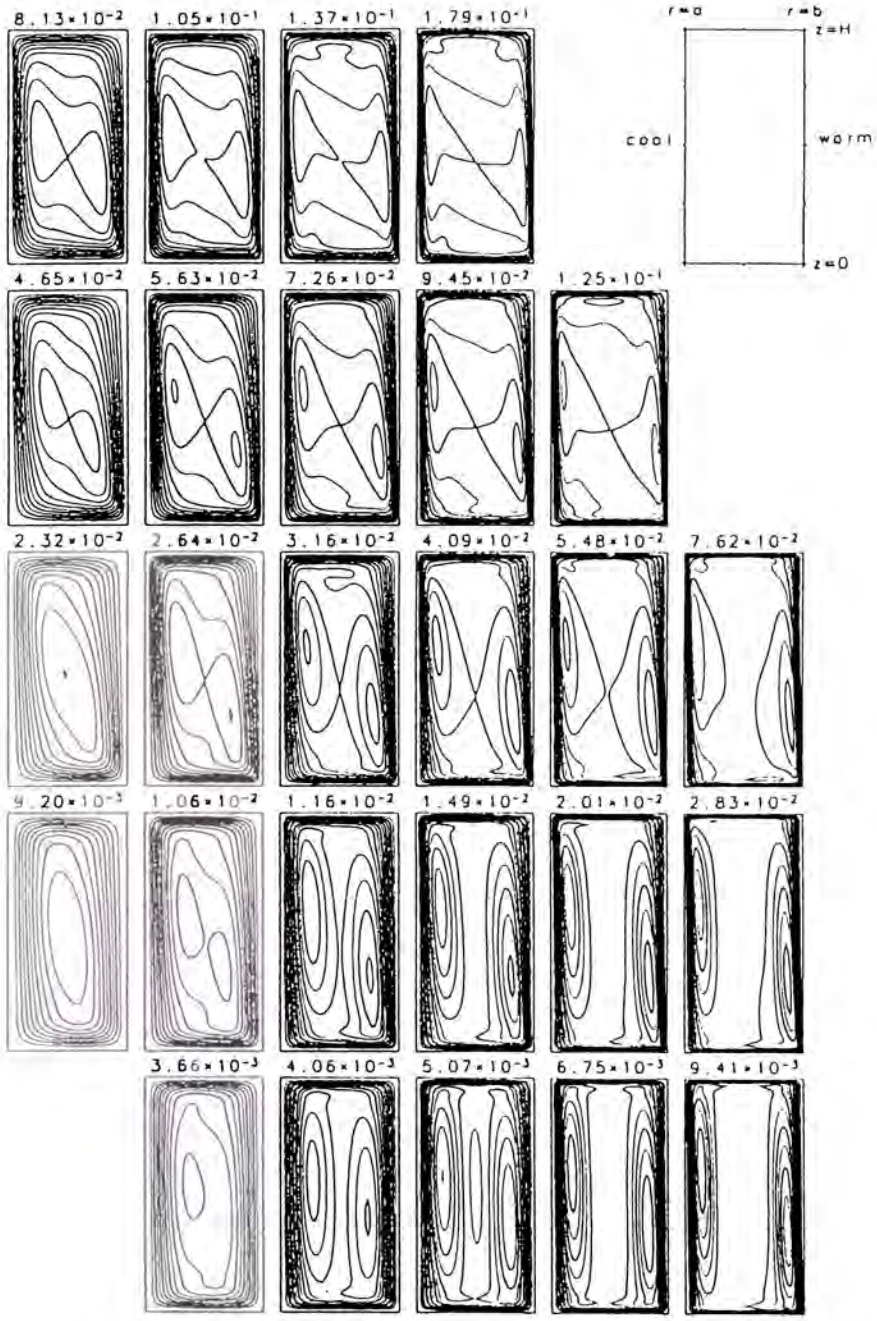

Fig. 2. Streamfunction of the meridional circulation of steady axi-symmetric flows for 26 cases, scaled by its maximum value at the mean radius $r_c=(a+b)/2$. The maximum value is indicated above each cross section with a unit of [cm^3/s]. The contour interval is 0.1. The arrangement of cross sections corresponds to that of circles in Fig. 1.

region is small for small ΔT. In the top and bottom boundary layers, the viscosity term is mostly balanced with the Coriolis term, which is indicative of the nature of the Ekman layer. In the side boundary layers, on the other hand, the viscosity term is essentially balanced with the buoyancy term, although the Coriolis term is also significant in the balance for small Ro_T.

3. Simple diagnostic model

3.1 Balance requirements

A simple diagnostic model is constructed in order to understand intuitively how the flow field obtained in the previous section is determined for given external parameters and how the heat transfer processes depend on the parameters. Several quantities which characterize the flow field are introduced, and their relationships are obtained from rough estimations.

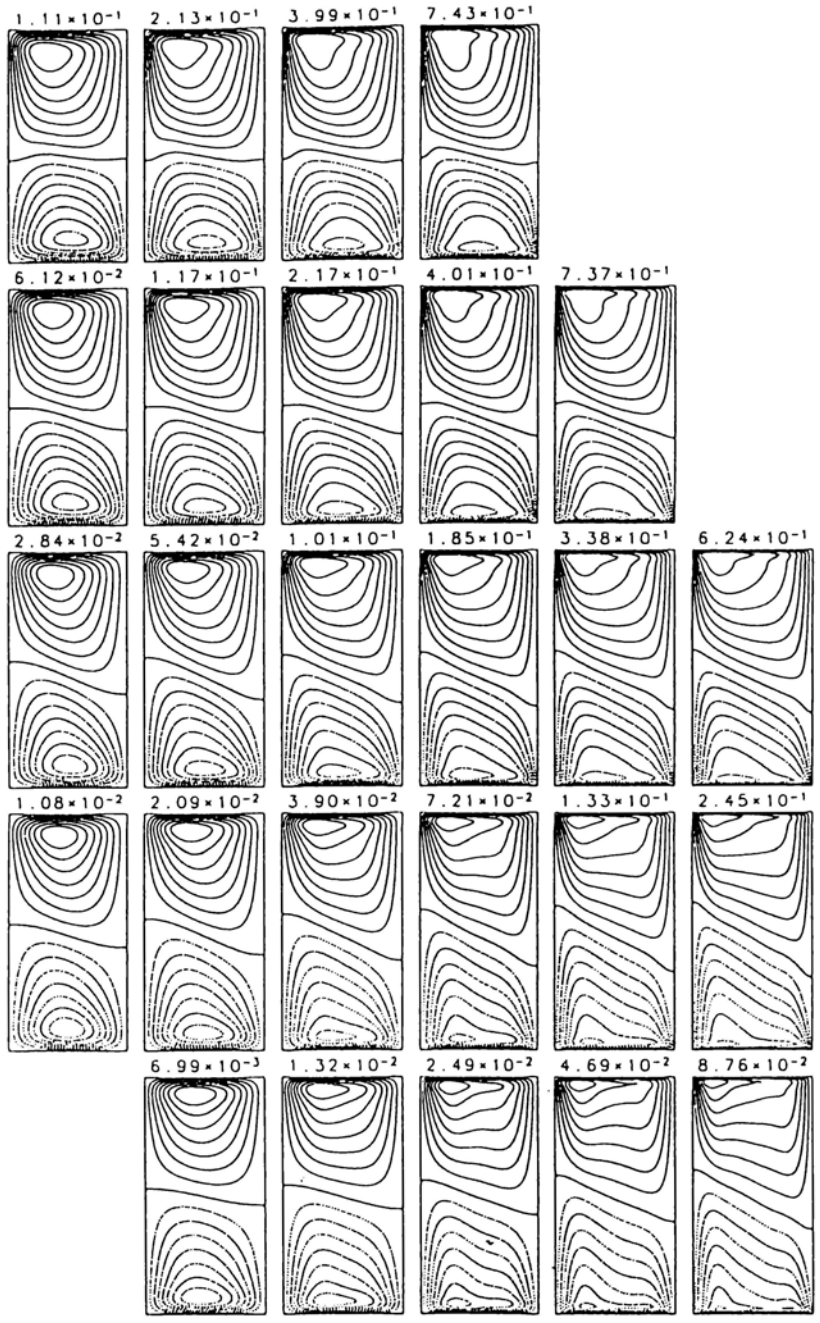

Fig. 3. As in Fig. 2, but for zonal velocity scaled by its maximum value. The maximum value is indicated above each cross section with a unit of [cm/s]. The contour interval is 0.125. Negative values are plotted with dotted lines.

Moreover, the dependence of the quantities on the parameters is discussed in the resulting simple system.

We consider an equilibrium state of the axi-symmetric flow in Cartesian coordinates (x, y, z) instead of the cylindrical coordinates (r, λ, z) neglecting the curvature of the annulus: $x=r$, and $y=r_c\lambda$, where $r_c=(a+b)/2$. The corresponding velocity components are (u, v, w), and the meridional circulation is expressed with a streamfunction Ψ as $(u, w)=\frac{1}{r_c}\left(\frac{\partial\Psi}{\partial z}, -\frac{\partial\Psi}{\partial x}\right)$, where the factor $1/r_c$ is useful in comparing the result with that in the previous section. The flow field in the meridional plane of height H and width $L(=b-a)$ is divided into five sections; the top and bottom boundary layers with depth h, the inner and outer side boundary layers with width l, and the interior region, of which height is then $H_I=H-2h$ and width is $L_I=L-2l$.

Now we introduce several variables which characterize the fundamental properties of the steady axi-symmetric flow. The axi-symmetric flow for the

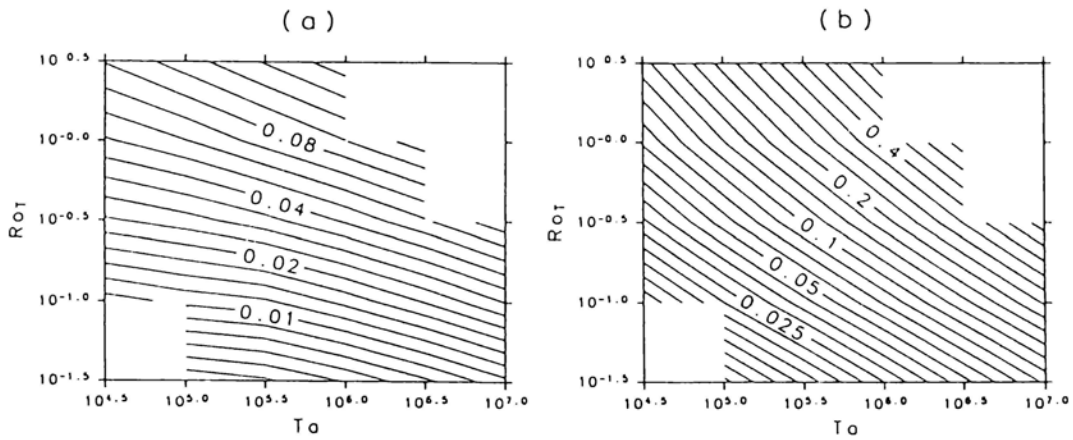

Fig. 4. (a) Dependence of the intensity of meridional circulation of $\log Ta$ and $\log Ro_T$; maximum value of streamfunction [cm^3/s] at the mean radius $r_c=(a+b)/2$ of the annulus is adopted as a measure of the intensity. Boundary value of the streamfunction is set to be zero. (b) Dependence of the maximum value of zonal flow [cm/s]. Both contour intervals are in geometrical proportion.

present parameter range is characterized as follows:

1. The meridional circulation is mostly confined to the boundary layers and its intensity is represented by Ψ_I, the value of the streamfunction just outside the boundary layers. The quantity Ψ_I/r_c represents the constant meridional volume flux per unit length in y direction.

2. The zonal flow field is characterized by the vertical shear and representative values of the zonal velocity at the top and bottom of the interior, $v_{(t)}$ and $v_{(b)}$, respectively, are introduced. The vertical shear has a magnitude of $(v_{(t)}-v_{(b)})/H_I$.

3. The normalized temperature field is characterized by three variables: an average temperature of the top boundary layer $\theta_{(t)}$, that of the bottom boundary layer $\theta_{(b)}$, and radial difference $\delta\theta$ across the interior region.

The quantities introduced here, h, l, Ψ_I, $v_{(t)}$, $v_{(b)}$, $\theta_{(t)}$, $\theta_{(b)}$ and $\delta\theta$, are determined for given external parameters.

Now we try to find relationships among these quantities and experimental parameters. The top and bottom boundary layers and the Ekman layer for the present parameter range of (Ta, Ro_T), because the Ekman number is sufficiently small; $\nu/2\Omega H^2 \leq 10^{-3}$. Therefore the depth h is given by the Ekman depth:

$$h=\sqrt{2}\pi h_0, \quad h_0=\sqrt{\nu/2\Omega}. \tag{1}$$

The depth is uniquely determined for a given rotation rate Ω. On the other hand, it is not straightforward to represent the width l of the side boundary layers with the external parameters. By a detailed analysis, McIntyre (1968) estimated the width, which depends on the temperature profile just outside the boundary layer. Here we leave the specification of l for a which. (Afterward we will make a crude assumption on l.)

To obtain a relationship between the zonal velocity and the temperature field, we use the thermal wind relation (*cf.* Eq. (4.4) in McIntyre (1968)), which approximately holds in the interior for the present parameter range;

$$\frac{v_{(t)}-v_{(b)}}{H_I}=\frac{g\alpha\Delta T}{2\Omega}\frac{\delta\theta}{L_I}. \tag{2}$$

From the theory of Ekman layer, $v_{(t)}$ and $v_{(b)}$ are related to the meridional circulation Ψ_I:

$$v_{(t)}=-v_{(b)}=\frac{\sqrt{2}\Psi_I}{h_0 r_c}. \tag{3}$$

This is the same as Eq. (5.3) in McIntyre (1968) except that radius r is replaced by the mean radius r_c. Elimination of $v_{(t)}$ and $v_{(b)}$ between (2) and (3) gives a relationship between Ψ_I and $\delta\theta$;

$$\frac{2\sqrt{2}}{H_I h_0 r_c}\Psi_I=\frac{g\alpha\Delta T}{2\Omega L_I}\delta\theta, \tag{4}$$

which means that the intensity of the meridional circulation is in proportion to the horizontal temperature difference in the interior if L_I is independent of Ψ_I and $\delta\theta$.

In order to obtain another relationship, we consider the heat transfer across the annulus. The inward heat flux integrated from the bottom to the top at any x must be equal in equilibrium states. For $x=a$ and r_c,

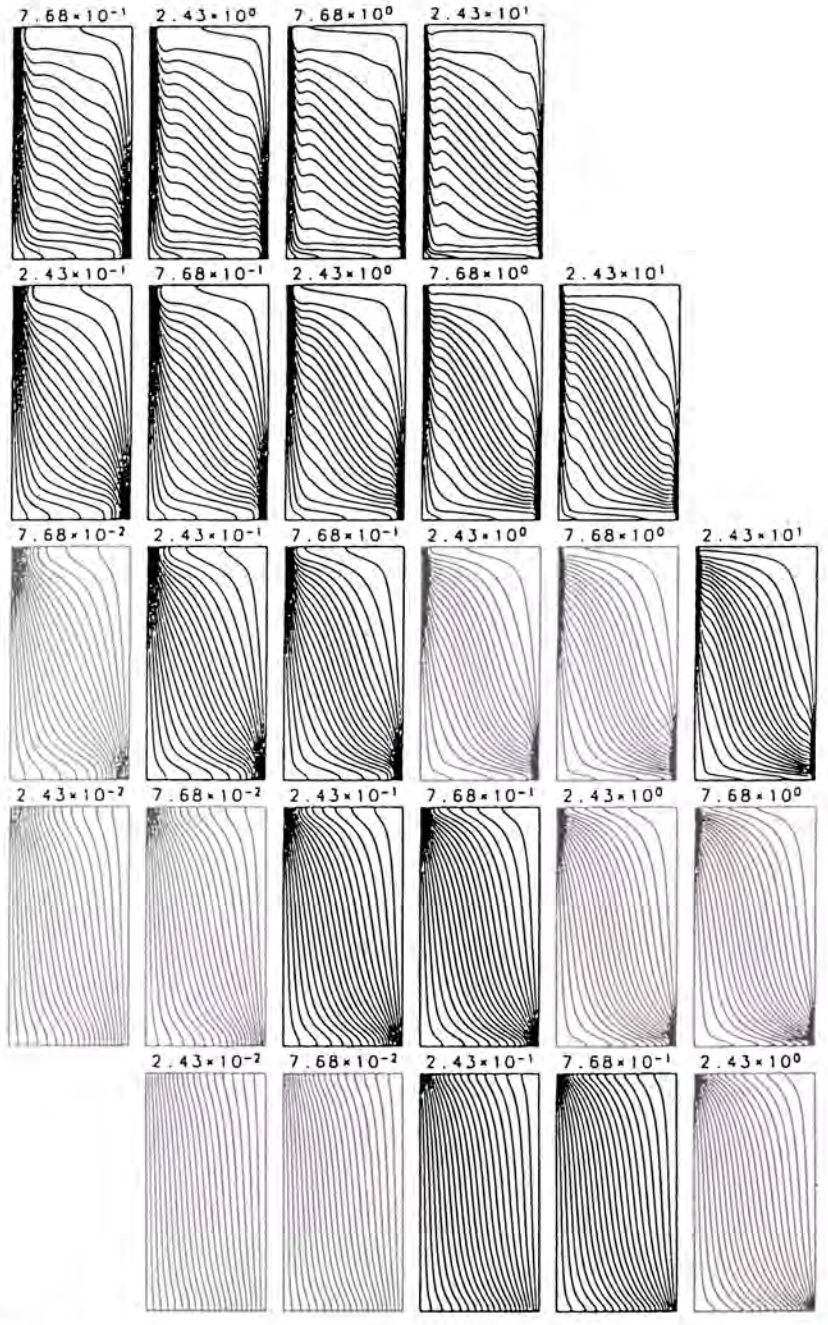

Fig. 5. As in Fig. 2 but for normalized temperature with a contour interval of 0.05. The value indicated above each cross section is ΔT [K].

$$\Delta T \int_0^H \kappa \left.\frac{\partial \theta}{\partial x}\right|_{x=a} dz = \Delta T \int_0^H \kappa \left.\frac{\partial \theta}{\partial x}\right|_{x=r_e} dz - \Delta T \int_0^H [u\theta]_{x=r_e} dz. \quad (5)$$

That is to say, the heat conduction at the inner wall is equal to the sum of conduction and convection at the mean radius. The heat conduction at the inner wall is estimated as

$$\Delta T \varepsilon \kappa \frac{1-\delta\theta}{2l} H, \quad (6)$$

where ε is a coefficient expressing the effect of the variation of horizontal temperature gradient in the side boundary layer, which gradually increases toward the wall. If the temperature gradient is constant throughout the layer, $\varepsilon=1$. The conduction term on the right-hand side (r.h.s.) of (5) is estimated as

$$\Delta T \kappa \frac{\delta\theta}{L_I} H, \quad (7)$$

while the convection term is estimated as

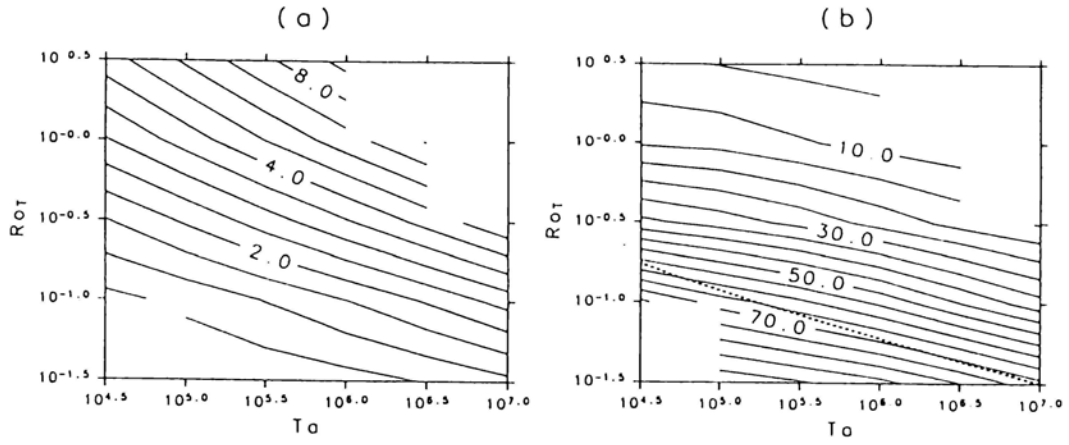

Fig. 6. As in Fig. 4, but for (a) the Nusselt number and (b) percentage of the conductive hear flux in the total heat flux at the mean radius. The contour interval is linear in (b). A thick dash-line in (b) indicates the 50 % line that is estimated from a simple diagnostic model described in Section 3.

$$\Delta T \frac{\Psi_I}{r_c}\left(\theta_{(t)}-\theta_{(b)}\right). \tag{8}$$

3y substituting (6)$\sim$(8) into (5), we obtain the fol-owing equation;

$$\varepsilon\kappa\frac{1-\delta\theta}{2l}H=\kappa\frac{\delta\theta}{L_I}H+\frac{\Psi_I}{r_c}\left(\theta_{(t)}-\theta_{(b)}\right), \tag{9}$$

vhich shows a relationship between Ψ_I and $\delta\theta$ op-)osite to Eq. (4); Ψ_I decreases with increasing $\delta\theta$ if)ther variables are assumed to be independent of Ψ_I ind $\delta\theta$.

The relative importance of the heat conduction ind the heat convection at the mean radius is given)y the ratio of two terms in the r.h.s. of (9). The 'atio γ becomes as follows with (4):

$$\gamma\equiv\frac{\text{(conductive heat flux)}}{\text{(convective heat flux)}}=\frac{4\sqrt{2}\kappa H\Omega}{H_I h_0 g\alpha\Delta T}\frac{1}{\theta_{(t)}-\theta_{(b)}}. \tag{10}$$

The ratio is inversely proportional to $\theta_{(t)}-\theta_{(b)}$, vhich is determined internally for given exter-ıal parameters. It is clear that $\theta_{(t)}-\theta_{(b)}\sim 0$ for :onduction-dominated flow and $\theta_{(t)}-\theta_{(b)}\sim 1$ for :onvection-dominated flow. In order to estimate the :elative importance in the ($\log Ta$, $\log Ro_T$)-plane, a ine of $\gamma=1$ is drawn in Fig. 6b (a dotted line) with $\theta_{(t)}-\theta_{(b)}=0.5$. The $\gamma=1$ line is not far from the :ontour of 50 % in Fig. 6b obtained from the non-inear results, which is indicative of the usefulness of the present simple model. From Eq. (10), it is :lear that convection is dominant ($\gamma\ll 1$) far above the dotted line in Fig. 6b, while conduction is dom-inant ($\gamma\gg 1$) far below the dotted line.

We need some other relationships or assumptions to close the system, because two Eqs. (4) and (9) still have the following variables; Ψ_I, $\delta\theta$, $\theta_{(t)}$, $\theta_{(b)}$ and L_I (or l). Now, we consider two extreme cases of convection-dominated flow and conduction-dominated flow, separately.

3.2 Convection-dominated flow

In the convection-dominated flow, the conduction term on the r.h.s. of (9) can be neglected, and temperature difference between the top and bottom boundary layers can be set to ΔT (*i.e.*, $\theta_{(t)}-\theta_{(b)}=1$). The latter assumption "linearizes" the heat convection term. Then the heat transfer equation (9) becomes

$$\frac{\Psi_I}{r_c}=\varepsilon\kappa\frac{1-\delta\theta}{2l}H. \tag{11}$$

Three variables Ψ_I, $\delta\theta$ and L_I (or l) still remain in (4) and (11).

To close the system, we further assume that the width l of the side boundary layers is determined only by the external parameters from balance requirements in the heat equation and the vorticity equation (see appendix for details):

$$l=2\left(\frac{\nu\kappa H}{g\alpha\Delta T}\right)^{1/4}. \tag{12}$$

Furthermore, the coefficient ε is set to be 2 in (11) because it is estimated from non-linear solutions that the horizontal temperature gradient at the boundary is about twice as large as that averaged in the boundary layer.

From the above assumptions and estimations, the system of (4) and (11) can be solved for Ψ_I and $\delta\theta$. That is, intensity of the meridional circulation and the temperature difference across the interior are determined for given external parameters. Figure 7a shows the two linear relations (4) and (11) for five values of Ro_T with fixed $Ta=10^6$ and Fig. 7b for

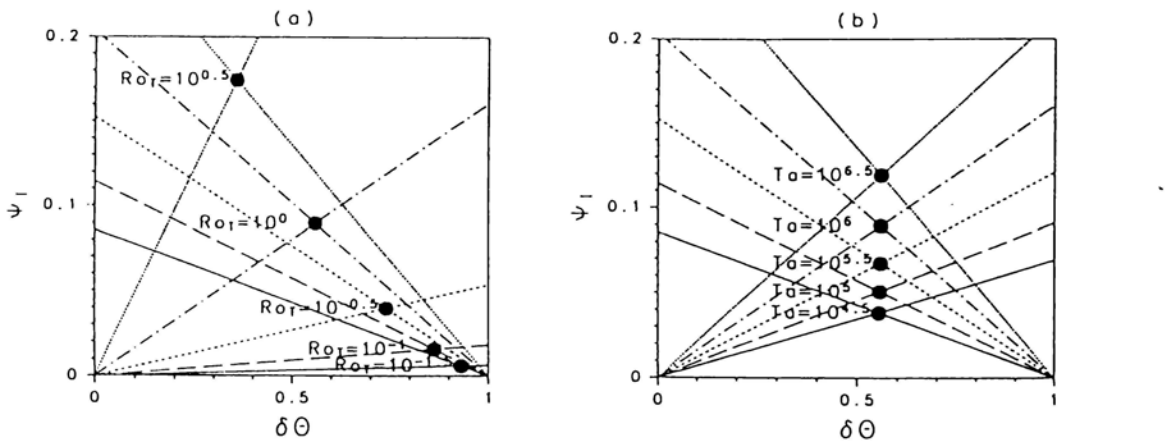

Fig. 7. Two linear relations between the radial temperature difference across the interior $\delta\theta$ and the intensity of meridional circulation Ψ_I [cm^3/s] for fixed Ta at 10^6 (a) and for fixed Ro_T at 10^0 (b). The intersection of the two lines indicated by • gives an equilibrium solution.

ive values of Ta with fixed $Ro_T = 10^0$. The intersection denoted by a closed circle gives the equilibrium solution Ψ_I and $\delta\theta$ in the present simple system. The gradient of a line of (4), which is drawn through the origin, depends mainly on the value of $\nu_0 \Delta T/\Omega (\propto \Delta T \Omega^{-3/2} \propto Ro_T Ta^{1/4})$, because H_I ($= H - 2h$) and L_I ($= L - 2l$) do not change very much owing to the smallness of the boundary layers. On the other hand, the gradient of a line of (11) depends only on l. Therefore, the negative gradient is nearly in proportion to $\Delta T^{1/4}$. If we fix Ta (, or Ω) and increase Ro_T (, or ΔT) as shown in Fig. 7a, the gradient of (4) increases much faster than that of (11) due to the 1/4-th power. As a result, Ψ_I of the equilibrium solution increases and $\delta\theta$ decreases. On the other hand, if we fix Ro_T and increase Ta, both lines of (4) and (11) increase their gradient as $\propto \Omega^{1/2}$ because $\Delta T \propto \Omega^2$ for Ro_T = constant. As a result, $\delta\theta$ of the equilibrium solution changes little and Ψ_I increases. The dependence of the two characteristic features on Ro_T and Ta corresponds well to the non-linear solutions in Section 2 (Figs. 2 and 5).

The simultaneous equations (4) and (11) are solved for Ψ_I and $\delta\theta$:

$$\Psi_I = \frac{\varepsilon \kappa H r_c}{2l} \frac{1}{1+f}, \tag{13}$$

$$\delta\theta = \frac{f}{1+f}, \tag{14}$$

where $f = 2\sqrt{2}\varepsilon\kappa H L_I \Omega / (l h_0 H_I g \alpha \Delta T)$. A measure of the zonal flow, $v_{(t)}$, is obtained from (3);

$$v_{(t)} = \frac{\varepsilon \kappa H}{\sqrt{2} l h_0} \frac{1}{1+f}. \tag{15}$$

Figure 8 shows the dependence of Ψ_I and $v_{(t)}$ on the two external parameters Ta and Ro_T. Note that the assumption of the predominance of convection and the estimation of (12) are valid in the upper part of each figure. The intensity of the meridional circulation Ψ_I shown in Fig. 8a is close to that in Fig. 4a for the non-linear solutions, particularly in the upper part. The intensity of the zonal flow $v_{(t)}$, which is shown in Fig. 8b, corresponds well to that of Fig. 4b. The Nusselt number is defined as $Nu = \Psi_I L / r_c \kappa H$ in this simple model, because the total heat flux equals $\Psi_I \Delta T / r_c$ from Eq. (8) and the ideal purely-conductive heat flux is $\kappa \Delta T H / L$. Hence the figure for Nu is identical to Fig. 8a except for the factor $L/r_c\kappa H$, and not shown here. The similarity between the contours of the intensity of meridional circulation and those of Nu was already pointed out in the previous section for the non-linear solutions (Figs. 4a and 6a). From these results, we conclude that our simple diagnostic model can represent the essential properties of the upper axi-symmetric flow reasonably well.

Now we further investigate the dependence of our solutions on the experimental parameters Ω and ΔT, or Ta and Ro_T. For the present parameter ranges, the boundary layers are estimated to be thin ($h \ll H$ and $l \ll L$) from (1) and (12), and then $L_I/H_I \sim L/H$, which is independent of Ω and ΔT. Therefore the quantity f in (13)$\sim$(15) is,

$$f = c_1 \Omega^{3/2} \Delta T^{-3/4} \tag{16}$$

where c_1 is a positive constant which is independent of the parameters Ω and ΔT. Equations (13)$\sim$(15) become as follows using the definitions of Ta and Ro_T;

$$\Psi_I = \frac{c_2 \Delta T^{1/4}}{1 + c_1 \Omega^{3/2} \Delta T^{-3/4}} = \frac{c_2' (Ta Ro_T)^{1/4}}{1 + c_1' Ro_T^{-3/4}}, \tag{17}$$

$$\delta\theta = \frac{c_1 \Omega^{3/2} \Delta T^{-3/4}}{1 + c_1 \Omega^{3/2} \Delta T^{-3/4}} = \frac{c_1' Ro_T^{-3/4}}{1 + c_1' Ro_T^{-3/4}}, \tag{18}$$

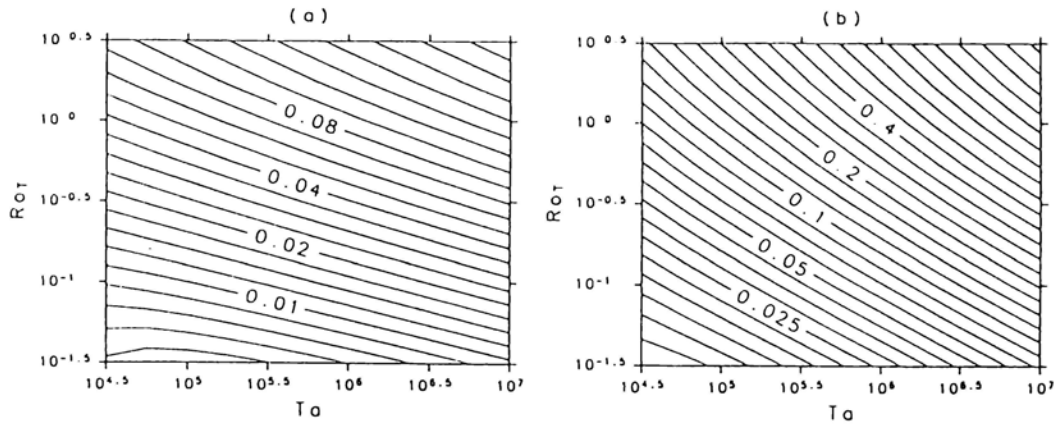

Fig. 8. As in Fig. 4, but for the present simple diagnostic model. (a) intensity of the meridional circulation, Ψ_I [cm^3/s]; (b) intensity of the zonal flow, $v_{(t)}$ [cm/s].

$$v_{(t)} = \frac{c_3 \Omega^{1/2} \Delta T^{1/4}}{1 + c_1 \Omega^{3/2} \Delta T^{-3/4}} = \frac{c_3' Ta^{1/2} Ro_T^{1/4}}{1 + c_1' Ro_T^{-3/4}} \propto Ta^{1/4} \Psi_I, \tag{19}$$

where all c_i and c_i' are positive constants. Numerator of the r.h.s. of (17) is constant along a line with $\log Ro_T = -\log Ta + \text{constant}$, which has a gradient of -1 in Fig. 8a, and increases from bottom-left to top-right in the figure. On the other hand, the denominator of the r.h.s. of (17) is constant along a horizontal line with $Ro_T = \text{constant}$, and increases from top to bottom. As a result, Eq. (17) gives an outline of the curved contours of Ψ_I shown in Fig. 8a. As for the measure of the zonal flow, Eq. (19) gives an outline of the curved contour shown in Fig. 8b, where gradient of each isoline is steeper than that of Ψ_I due to the factor $Ta^{1/4}$. As shown in Eq. (18), the temperature difference $\delta\theta$ depends only on Ro_T but not on Ta. This dependence explains the characteristic thermal structure shown in Fig. 5, where the slope of the isotherms in the interior depends mainly on Ro_T.

3.3 Conduction-dominated flow

In the conduction-dominated flow, the convection term on the r.h.s. of (9) can be neglected and the parameter ε can be set to 1. Then the heat transfer equation is reduced to

$$\frac{\delta\theta}{L_I} = \frac{1}{L}. \tag{20}$$

Therefore the side thermal boundary layers do not exist and the thermal wind relation holds across the annulus. The vertical shear is estimated from the thermal wind relation (2), and the zonal flow $v_{(t)}$ is obtained with (3) as follows;

$$v_{(t)} = \frac{g\alpha H_I}{4L} \frac{\Delta T}{\Omega}. \tag{21}$$

The Ekman layer theory gives the relationship (3) between Ψ_I and $v_{(t)}$,

$$\Psi_I = \frac{g\alpha H_I r_c \sqrt{\nu}}{8L} \frac{\Delta T}{\Omega^{3/2}}. \tag{22}$$

Plots of these quantities in the ($\log Ta$, $\log Ro_T$)-plane (not shown) correspond well to those in the lower part of Fig. 4a and 4b.

4. Discussion

In the previous section two diagnostic Eqs. (4) and (9) are derived from several balance requirements. They have opposite relation between the intensity of the meridional circulation, Ψ_I, and the radial temperature difference across the interior, $\delta\theta$. Here we summarize the physical meaning of the two equations. Equation (4) is based on the thermal wind balance (2) and the mass-transport requirement in the Ekman layer (3). From the thermal wind balance the zonal flow just outside the Ekman layer, $v_{(t)}$, is large for large $\delta\theta$. At the same time, Ψ_I must be large for large $v_{(t)}$ from the mass-transport requirement. As a result, *the intensity of the meridional circulation (Ψ_I) must be large for large radial temperature difference ($\delta\theta$)*. On the other hand, Eq. (9) is a balance requirement in the heat budget. If $\delta\theta$ is large, the heat conduction at the side boundaries is small because the temperature gradient in the side boundary layer, $(1-\delta\theta)/2l$, is small. Then the convective heat flux outside the side boundary layers, namely, the last term in (9), must be small because the l.h.s. of (9) is small and the first term in the r.h.s. is not negligible. That is, *the intensity of the meridional circulation (Ψ_I) must be small for large radial temperature difference ($\delta\theta$)*. These two balance requirements with opposite relation between Ψ_I and $\delta\theta$ determine Ψ_I and $\delta\theta$ uniquely for given external parameters as shown in Fig. 7 for convection-dominated flow.

The balanced flow that is obtained in this simple diagnostic model has dependence on the external parameters through the coefficients in Eqs. (4) and (11) for convection-dominated flow. The dependence can be divided into two parts; one is the term $\Delta T/\Omega$ in (4) and the other is the thickness of the boundary layers h and l, which depends on the external parameters as shown in (1) for the top and bottom boundary layers and (12) for the side boundary layers. Now we set the width and the depth of the boundary layers to be constant in order to focus on the term $\Delta T/\Omega$ in (4). Then Eqs. (17), (18) and (19) become as follows,

$$\Psi_I = \frac{d_2}{1 + d_1 Ta^{-1/2} Ro_T^{-1}}, \tag{23}$$

$$\delta\theta = \frac{d_1}{1 + d_1 Ta^{-1/2} Ro_T^{-1}}, \tag{24}$$

$$v_{(t)} = \frac{d_3}{1 + d_1 Ta^{-1/2} Ro_T^{-1}}, \tag{25}$$

where d_i are positive constants independent of Ω and ΔT. All of Ψ_I, $\delta\theta$ and $v_{(t)}$ depend only on $Ta^{1/2}Ro_T$. Isolines of these measures are straight lines in the ($\log Ta$, $\log Ro_T$)-plane and have a gradient of $-1/2$, which explains very essence of the dependence in Fig. 8, particularly good for Ψ_I (a). That is to say, the term $\Delta T/\Omega$ in the thermal wind relation essentially determines the dependence on the external parameters, and the variation of the boundary-layer thickness modifies it: Owing to the variation of the thickness, gradient of isolines of the meridional circulation becomes gentle, while that of the zonal flow becomes steep.

The simple diagnostic model introduced in this study is based on three equations; the thermal wind equation (2), the Eq. (3) for the mass transport in the Ekman layer, and the heat budget equation (9). It is worthy to point out that (3) is also an equation for the angular momentum budget. At the mean height $z=H/2$, upward angular momentum flux in the outer side boundary layer is estimated as $b^2\Omega \cdot \Psi_I/b$ and downward flux in the inner side boundary layer as $a^2\Omega \cdot \Psi_I/a$, because the zonal flow is almost zero at $z=H/2$. Therefore the net upward flux is $(b-a)\Omega\Psi_I$ at the mean height. In an equilibrium state, it must be compensated by the diffusion at the boundaries in the upper (or lower) half of the container. The diffusion of angular momentum at the upper lid is estimated as $\nu\frac{r_c v_{(t)}}{h}(b-a)$. Therefore $v_{(t)}=\pi\Psi_I/(\sqrt{2}r_c h_0)$ if we neglect the diffusion at the side boundaries, which is small compared with that at the upper lid (see Fig. 3). If we compare this with Eq. (3), only a factor of $\pi/2$ is different. Thus Eq. (3) can be interpreted as an equation for the angular momentum budget.

5. Conclusions

Steady axi-symmetric flow in a rotating annulus with differential heating was obtained by numerical time-integrations of the two-dimensional Navier-Stokes equations over a wide range of external parameters. The velocity field of the meridional circulation, the zonal flow and the temperature field are shown at 26 points around the anvil-shaped transition curve in the régime diagram (Figs. 2, 3, and 5). The meridional circulation is mostly confined to thin boundary layers and its intensity is large for large Taylor number (Ta) and large thermal Rossby number (Ro_T). The width of the side boundary layers and depth of the top and bottom boundary layers depend on these parameters separately. The vertical shear of the zonal flow is large for large Ta and large Ro_T. The temperature field is intimately related to the intensity of the meridional circulation, because the circulation has an important role in heat convection in the meridional heat transfer, particularly for large Ro_T. Moreover, the temperature field is in the thermal wind balance with the zonal flow in the interior region.

Several quantities which characterize these features of the steady axi-symmetric flow are selected and their dependence on the parameters is clarified quantitatively (Figs. 4 and 6). The intensity of the meridional circulation and the Nusselt number have similar dependence, while the zonal flow has a different dependence.

A simple diagnostic model was constructed to understand intuitively how the flow field is determined for given external parameters. The intensity of the meridional circulation and radial temperature difference across the interior are key variables to characterize the flow field. Two Eqs. (4) and (9), which are the essence of our model, give their relationships under appropriate assumptions; Eq. (4) is the thermal wind relation in the interior with the Ekman layer theory and (9) is the heat transfer equation. Our simple model reproduces the dependence of these quantities on Ta and Ro_T obtained in the full nonlinear computations.

The convection-dominated flow is essentially determined as follows: Zonal flow just outside the Ekman layer must be strong for large radial temperature difference across the interior from the thermal wind balance. At the same time, the meridional circulation must be strong for the strong zonal flow from the mass-transport relation in the Ekman layer. That is, the meridional circulation must be *strong* for a large radial temperature difference across the interior. On the other hand, the heat transfer equation gives an opposite relationship between these quantities. If the radial temperature difference across the interior is large, that across the side boundary layers is small, namely, the heat flux

at the side boundaries is small. Then the convective heat flux outside the side boundary layers must be small from the heat balance requirement. That is, the meridional circulation must be *weak* for a large radial temperature difference across the interior. These two balance requirements with opposite relationships determine the intensity of the meridional circulation and the radial temperature difference across the interior uniquely for given external parameters Ta and Ro_T.

On the other hand, the conduction-dominated flow is determined as follows: The temperature field is determined by the heat conduction. Therefore, the side thermal boundary layers do not exist. The zonal flow field is in thermal wind balance with the temperature field. By the Ekman layer theory, the intensity of the meridional circulation is related to the zonal flow at the top and bottom of the interior region.

Acknowledgments

The authors wish to thank Professor I. Hirota and Dr. S. Sakai for their valuable comments during the work. The GFD-DENNOU Library produced by Drs. M. Shiotani and S. Sakai was used for drawing the figures.

Appendix

Width of the side boundary layer

McIntyre (1968) showed that the width of the side boundary layer is not strictly determined only by the external parameters. However, it is possible to estimate the width l for the present simple model under several acceptable approximations.

The heat equation in the side boundary layer is approximated as follows (McIntyre, 1968):

$$\frac{\Delta T}{r_c}\left(\frac{\partial \Psi}{\partial z}\frac{\partial \theta}{\partial x}-\frac{\partial \Psi}{\partial x}\frac{\partial \theta}{\partial z}\right)=\kappa \Delta T\frac{\partial^2 \theta}{\partial x^2}, \tag{26}$$

where θ is the normalized temperature. From this equation a scale for Ψ is estimated with a scale of the boundary layer l_s,

$$\Psi \sim r_c \kappa H/l_s. \tag{27}$$

As pointed out in Section 2, the vorticity equation is essentially in a buoyancy-viscous balance in the side boundary layer:

$$-g\alpha \Delta T\frac{\partial \theta}{\partial x}=\frac{\nu}{r_c}\frac{\partial^4 \Psi}{\partial x^4}. \tag{28}$$

Again, a scale for Ψ is estimated from this equation,

$$\Psi \sim \frac{r_c}{\nu} g\alpha \Delta T\frac{1-\delta\theta}{2}l_s^3, \tag{29}$$

because the radial scale of θ is $(1-\delta\theta)/2$. Thus the scale l_s is obtained from (27) and (29):

$$l_s=\left(\frac{\nu\kappa H}{g\alpha \Delta T}\frac{2}{1-\delta\theta}\right)^{1/4}. \tag{30}$$

In this relation, dependence of the scale l_s on $\delta\theta$ is smaller than that on ΔT because $\delta\theta$ is very small compared to 1 in the convection-dominated flow. Therefore we can neglect the dependence on $\delta\theta$. Moreover, considering the fact that an effective width of the boundary layer is several times as large as its scale, we set the width l as follows:

$$l=2\left(\frac{\nu\kappa H}{g\alpha \Delta T}\right)^{1/4}. \tag{31}$$

If we assume the coefficient $1.3|z_1|/B_1$ is 2 in Eq. (9.3) in McIntyre (1968), estimating from his Fig. 6, the same equation corresponding to (31) is obtained.

References

Fowlis, W.W. and R. Hide, 1965: Thermal convection in a rotating annulus of liquid: effect of viscosity on the transition between axi-symmetric and non-axi-symmetric flow régimes. *J. Atmos. Sci.*, **22**, 541-558.

Held, I.M. and A.Y. Hou, 1980: Nonlinear axially symmetric circulation in a nearly inviscid atmosphere. *J. Atmos. Sci.*, **37**, 515-533.

Hide, R. and P.J. Mason, 1975: Sloping convection in a rotating fluid. *J. Adv. Phys.*, **24**, 47-100.

Hunter, C., 1967: The axi-symmetric flow in a rotating annulus due to a horizontally applied temperature gradient. *J. Fluid Mech.*, **27**, 753-778.

Lorenz, E.N., 1962: Simplified dynamic equations applied to the rotating-basin experiments. *J. Atmos. Sci.*, **19**, 39-51.

Lorenz, E.N., 1963: The mechanics of vacillation. *J. Atmos. Sci.*, **20**, 448-464.

McIntyre, M.E., 1968: The axi-symmetric convective régime for a rigidly bounded rotating annulus. *J. Fluid Mech.*, **32**, 625-655.

Schneider, E.K., 1977: Axially symmetric steady state models of the basic state for instability and climate studies. Part II. Nonlinear calculations. *J. Atmos. Sci.*, **34**, 280-296.

Schneider, E.K. and R.S. Lindzen, 1977: Axially symmetric steady state models of the basic state for instability and climate studies. Part I. Linear calculations. *J. Atmos. Sci.*, **34**, 263-279.

Sugata, S. and S. Yoden, 1991: The effects of centrifugal force on the stability of axi-symmetric viscous flow in a rotating annulus. *J. Fluid Mech.*, **229**, 471-482.

Tokioka, T., 1970: A stability of axi-symmetric flows in a rotating annulus. *J. Meteor. Soc. Japan*, **48**, 293-314.

Williams, G.P., 1967a: Thermal convection in a rotating fluid annulus: part 1. The basic axi-symmetric flow. *J. Atmos. Sci.*, **24**, 144-161.

Williams, G.P., 1967b: Thermal convection in a rotating fluid annulus: part 2. Classes of axi-symmetric flow. *J. Atmos. Sci.*, **24**, 162-174.

回転水槽実験における定常軸対称流とその実験パラメータ依存性

菅田誠治・余田成男
(京都大学理学部)

回転水槽中で水平加熱差によって駆動される定常軸対称流を高解像度の二次元非線形数値モデルを用いて求めた。得られた軸対称流の速度場と温度場が実験パラメータにどう依存しているかを広いパラメータ領域で調べた。

定常軸対称流の速度場と温度場が、与えられたパラメータに対してどのように決まるかを直観的に理解できる診断モデルを構築した。モデルは熱伝導が支配的な流れと対流が支配的な流れの両方に適用でき、どのように熱輸送形態が決まるのかを定性的に説明できる。さらに、このモデルを用いて、子午面循環の強さ、東西流の強さ、および内部領域での水平温度差といった、軸対称流を特徴づけるいくつかの量のパラメータ依存性を求めることができる。これらの結果は非線形モデルで得られた結果をうまく説明する。

発表論文 3

A numerical study on regime transitions of the rotating annulus flow with a semi-spectral model

Seiji Sugata and Shigeo Yoden

A Numerical Study on Régime Transitions of the Rotating Annulus Flow with a Semi-Spectral Model

By Seiji Sugata[1] and Shigeo Yoden

Department of Geophysics, Kyoto University, Kyoto 606-01, Japan
(Manuscript received 29 January 1993, in revised form 7 June 1993)

Abstract

Some of the rotating annulus experiments with radial differential heating show stepwise transitions of flow régimes from steady axi-symmetric flow to vacillation via a steady wave régime as the rotation rate increases. The stepwise régime transitions are investigated numerically with a semi-spectral model of a three-dimensional Boussinesq fluid, and the results are interpreted with bifurcation theories. The transition between axi-symmetric flow and a steady wave régime is characterized by hysteresis; the criterion for the disappearance of an established steady wave differs from the criterion for the onset of the steady wave. The branch of the steady wave solution does not bifurcate from that of the axi-symmetric flow at the point where the axi-symmetric flow becomes unstable. Instead, the steady wave branch has another type of critical point (interpreted as a "limit point") at which it disappears. The transition from steady wave to tilted-trough vacillation is interpreted as a Hopf bifurcation; a periodically fluctuating solution bifurcates from the steady wave branch when the steady wave solution loses its stability.

1. Introduction

Hydrodynamic instabilities and the corresponding transitions of flow régimes have been one of the interesting subjects in contemporary fluid dynamics (*e.g.* Swinney and Gollub, 1981). When an experimental parameter is changed gradually, stepwise transitions from a steady symmetric flow to irregular turbulent flow are observed in some experiments such as the Rayleigh-Bénard convection and the Taylor-Couette flow. Modern technology in laboratory experiments and advanced computing facilities for numerical experiments have improved our understanding of the transitions of flow régimes. Moreover, bifurcation theories and chaos theories have given fundamental concepts of the transitions of flow régimes.

Some of the rotating annulus experiments with radial differential heating, which contain the basic dynamics of the general circulation of the atmosphere, show similar stepwise transitions from steady axi-symmetric flow to irregular turbulent flow via steady wave and vacillation régimes (see *e.g.* Hide and Mason, 1975). A régime diagram obtained by Fowlis and Hide (1965) is shown in Fig. 1 together with recent results by Tamaki and Ukaji (1985; hereafter referred to as TU85) and Ukaji and Tamaki (1989, 1990; hereafter UT89 and UT90, respectively). The flow régimes are mainly dependent on two non-dimensional parameters of the Taylor number, Ta (the abscissa) and the thermal Rossby number, Ro_T (the ordinate). If the rotation rate Ω of the annulus is increased gradually with a constant temperature difference ΔT between the outer and inner walls, say $\Delta T = 3$ K indicated by a straight line in Fig. 1, a sequence of régime transitions are obtained from steady axi-symmetric flow to irregular flow. In some laboratory experiments (*e.g.* Fultz *et al.*, 1959; TU85; Hignett, 1985), hysteresis is observed at the transition from the axi-symmetric to wave régime and in the wave régime; two or more stable states may exist for the same experimental parameters depending on the initial conditions. In addition, a new class of amplitude vacillations, which are adjacent to a transition to the next lowest wavenumber as shown in Fig. 1 with $\Delta T = 8$ K, are also obtained by TU85 and by Hignett (1985).

The transition from axi-symmetric flow to a wave régime was firstly investigated by Lorenz (1962) with a low-order model of a two-layer quasi-geostrophic fluid system. He analyzed a set of nonlinear ordinary differential equations with 8 dependent variables obtained by means of highly truncated Fourier-Bessel series. He proved with the simplified model that the steady axi-symmetric flow is always possible in a mathematical sense but unsta-

[1]Present affiliation: The National Institute for Environmental Studies, Tsukuba, Ibaraki 305, Japan.

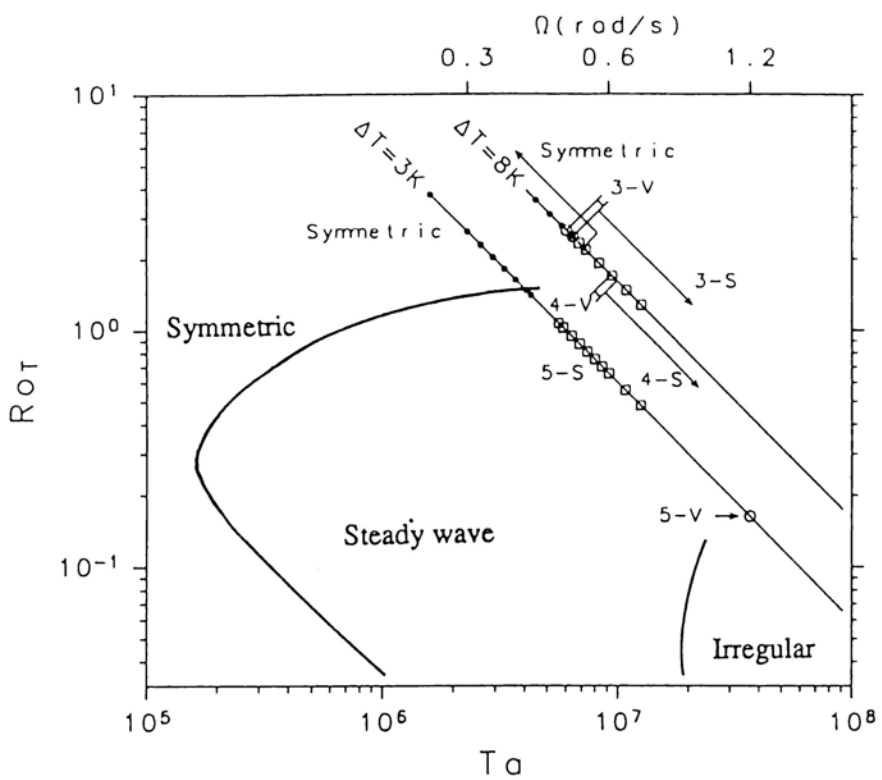

Fig. 1. Régime diagram obtained by Fowlis and Hide (1965), together with the results by Tamaki and Ukaji (1985) and Ukaji and Tamaki (1989, 1990) along two diagonal lines of constant temperature difference $\Delta T = 3$ K and 8 K. Dots denote axi-symmetric flow, m-S a steady wave of the dominant wavenumber m, and m-V vacillation of the dominant wavenumber m.

ble with respect to wave disturbance for certain combinations of Ta and Ro_T, that is, the inside of an anvil-shaped curve in the régime diagram. The transition occurs as a manifestation of baroclinic instability of the axi-symmetric flow. Moreover, hysteresis in the upper transition for large Ta is obtained in his low-order model in agreement with the laboratory experiments by Fultz *et al.* (1959): the criterion for the disappearance of an established steady wave differs from the criterion for the onset of the steady wave. Matsuda and Yoden (1985) illustrated a bifurcation diagram for the hysteresis based on these results.

Lorenz (1963) modified the model to explore further transitions of régimes. The geometry of the cylindrical annulus was changed to an infinite channel with a double-Fourier series and the second lateral mode was retained to get a non-linear system of 14 variables. Numerical solutions of vacillations and irregular flows were obtained by time integrations, in addition to analytic solutions of axi-symmetric flows and steady waves. Extension of this Lorenz model was done by Quinet (1973a, b) and Yoden (1979) with the inclusion of some higher modes to investigate the structure of non-linear processes in the flow régime transitions further. Detailed analysis of the régime transitions in the Lorenz model was done by Ghil and Childress (1987) with bifurcation theory. Figure 2 is a bifurcation diagram showing the dependence of solutions on the external parameter k^{-1} that is regarded as a rotation rate. As k^{-1} is increased in the diagram, the axi-symmetric flow (denoted by H) loses its stability at the point A and a steady wave solution of the first mode (R_1) bifurcates from the point. At the point B the wave solution R_1 becomes unstable and two steady-wave branches of R'_{12} and R''_{12} bifurcate. Solutions R'_{12} and R''_{12} differ from each other only in the sign of the second lateral mode, owing to the spatial symmetry of the mode (Yoden, 1985). A Hopf bifurcation takes place at D′ (D″) and a stable periodic solution UV' (UV'') appears, which is a class of tilted-trough vacillation. Finally, non-periodic chaotic solutions (T) appear after some further bifurcations. The sequence of bifurcations leads to solutions of increasing spatial and temporal complexity, as the simpler solutions lose their stability. A general theory of the symmetry-breaking in spatial structures at bifurcation points was given by Matsuda (1983).

Stepwise transitions from steady axi-symmetric flow to irregular turbulent flow with increasing complexity of flow patterns are *qualitatively* illustrated in the Lorenz model. Detailed analysis of the model is possible because its dependent variables

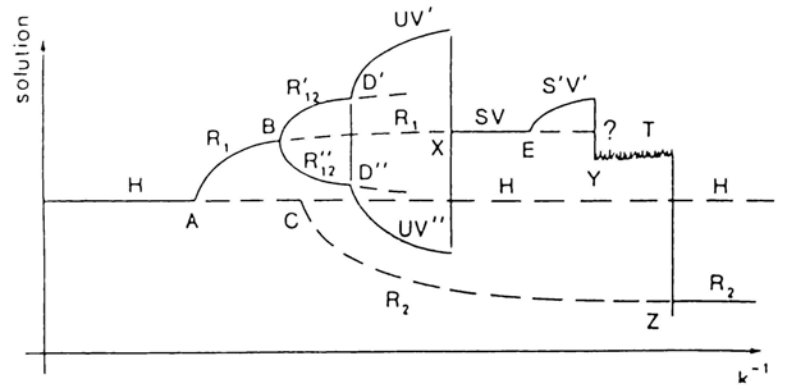

Fig. 2. Bifurcation diagram for the Lorenz (1963) model drawn by Ghil and Childress (1987). The solid line is a branch of the stable solution, the dashed line that of an unstable one. The abscissa is a bifurcation parameter proportional to the rotation rate. See text for details.

are of the order of O (10) owing to the severe truncation. However, several crude assumptions (approximations) were also made to obtain the model: quasi-geostrophy, a two-layer system, Ekman friction, non-existence of lateral boundary layers, and so on.

A quite different approach in numerical studies on the rotating annulus flows originated from Williams (1967a, 1967b, 1969). He solved two- or three-dimensional Navier-Stokes equations numerically without many approximations. Advances in computing facilities over these years have made it possible to compare numerical simulations directly with laboratory measurements (*e.g.* Hignett *et al.*, 1985; UT89; UT90; Sugata and Yoden, 1991). Recently, Miller and Butler (1991) investigated the hysteresis in the transition between axi-symmetric flow and the steady wave régime with a semi-spectral model of Boussinesq fluid. They obtained the hysteresis for large ΔT only in the case of a free surface, which result was consistent with the laboratory experiment by Fein (1973). The spatial structure of the flow field and energetics in the hysteresis were also diagnosed carefully with the three-dimensional data obtained. Investigation of further transitions of flow régimes was left for future study.

In this study, we develop a similar semi-spectral model without many approximations to investigate the stepwise transitions of flow régimes in the rotating annulus experiments. The transition to tilted-trough vacillation is clarified as well as the transition between axi-symmetric flow and steady wave régime. Our model is similar to that introduced by Miller and Butler (1991) but includes wave-wave interactions with the first harmonics. However, the present semi-spectral model has limitations for the study of some vacillations in which side-bands of the dominant wave may play an important rôle (*e.g.* Pfeffer *et al.*, 1980). Numerical results are interpreted with bifurcation theories.

2. The model

We consider water contained between two coaxial cylinders of inner and outer radii a and b, respectively, and two parallel horizontal planes of depth H. The dimensions are $a=4.5$ cm, $b=9.7$ cm and $H=8.0$ cm, which are the same as those in TU85, UT89 and UT90. The top surface is assumed to be a free-slip surface at $z=H$ with no undulation. The other three bonding surfaces are rigid. The inner and outer walls are held at different constant temperatures, T_a and T_b ($T_a<T_b$), to maintain the difference ΔT. The top and bottom boundaries are thermally insulating. The container rotates at a constant rate Ω. Controllable experimental parameters are ΔT and Ω.

The governing equations under the Boussinesq approximation are:

$$u_t + uu_r + \frac{vu_\lambda}{r} + wu_z - \frac{v^2}{r} - 2\Omega v = -p_r + \nu\left[u_{zz} + \frac{1}{r^2}u_{\lambda\lambda} - w_{rz} - \frac{1}{r^2}(rv_\lambda)_r\right], \tag{1}$$

$$v_t + uv_r + \frac{vv_\lambda}{r} + wv_z + \frac{uv}{r} + 2\Omega u = -\frac{p_\lambda}{r} + \nu\left[\left\{\frac{1}{r}(rv)_r\right\}_r + v_{zz} - \left(\frac{u}{r}\right)_{r\lambda} - \frac{1}{r}w_{z\lambda}\right], \tag{2}$$

$$w_t + uw_r + \frac{vw_\lambda}{r} + ww_z = -p_z + \nu\left[\frac{1}{r}(rw_r)_r + \frac{1}{r^2}w_{\lambda\lambda} - \frac{1}{r}v_{z\lambda} - \frac{1}{r}(ru_z)_r\right] + \alpha\Delta T\theta g, \tag{3}$$

$$\theta_t + u\theta_r + \frac{v\theta_\lambda}{r} + w\theta_z = \kappa\left[\theta_{rr} + \frac{1}{r}\theta_r + \frac{1}{r^2}\theta_{\lambda\lambda} + \theta_{zz}\right], \tag{4}$$

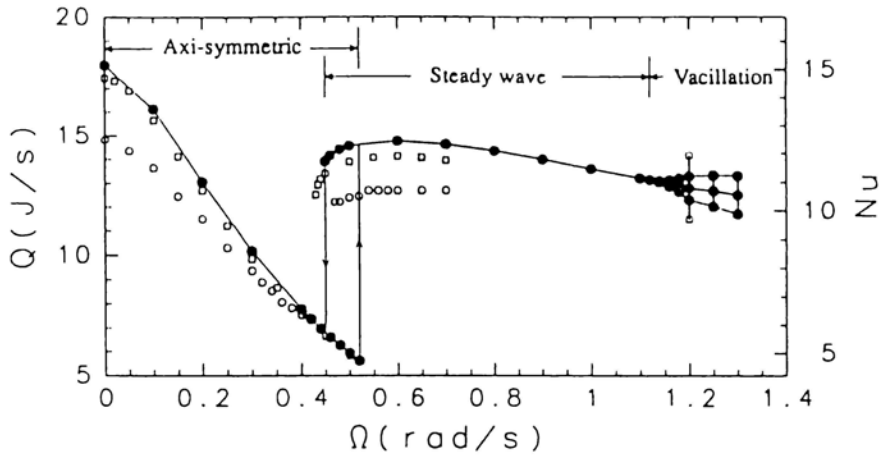

Fig. 3. Dependence of total inward heat flux Q (or, the Nusselt number Nu) on the rotation rate Ω. Symbol •—• is for the present model; ○, laboratory experiment by Ukaji and Tamaki (1989); □, numerical simulation by them. In the vacillation régime the variable range and time average are plotted. The amplitude of the vacillation obtained by Ukaji and Tamaki is overestimated because it is taken from limited plots in their figure.

$$u_r + \frac{u}{r} + \frac{v_\lambda}{r} + w_z = 0, \tag{5}$$

where (r, λ, z) are cylindrical coordinates, and t time. The corresponding velocity components are (u, v, w). Dimensionless temperature θ is defined as $\theta \equiv (T - T_a)/\Delta T$. Density is denoted by ρ, and p is pressure divided by the mean density ρ_0. The viscosity term is not the conventional form in order to avoid a round-off error in computation (Williams, 1969). Physical parameters of water are assumed to be constant at the mean temperature 26.5°C: the kinematic viscosity, $\nu = 8.65 \times 10^{-3}\ \mathrm{cm^2\ s^{-1}}$; the diffusivity of heat, $\kappa = 1.45 \times 10^{-3}\ \mathrm{cm^2\ s^{-1}}$; the coefficient of volume expansion, $\alpha = 2.71 \times 10^{-4}\ \mathrm{K^{-1}}$.

In order to get a semi-spectral form of the equations, we decompose each dependent variable into the axisymmetric part and wave parts as follows:

$$x(r, \lambda, z, t) = X(r, z, t) + \sum_{n=1}^{N} \mathrm{Re}\left[x_n(r, z, t) e^{imn\lambda}\right] \tag{6}$$

where x denotes u, v, w, θ or p. Here periodicity in the azimuthal direction is assumed with $\Delta\lambda = 2\pi/m$, and x_n (r, z, t) is the complex amplitude of a dominant wave $(n=1)$ and its higher harmonics $(n = 2, 3, \cdots)$. Substituting these expressions into (1)–(5) and making a finite difference approximation in r, z and t, we obtain a semi-spectral form of the governing equations. The same finite difference method as in Williams (1969) is adopted. The grid resolution is determined after a convergence test of the solutions; 64 (r-direction) $\times$ 64 (z-direction) and $\Delta t = 2.5 \times 10^{-2}$ s.

The assumption of the azimuthal periodicity is validated with the laboratory experiment by TU85; their careful measurement with a precise apparatus showed that the amplitudes of the side-bands and the longest wave are of the order of 1% of the total temperature variation (~the dominant wave + its higher harmonics) not only in steady wave régime but in vacillation. Moreover, both the laboratory experiment (TU85) and the numerical experiment (UT90) showed that the amplitude of the higher harmonics decreases exponentially with n; the first harmonic is less than 20% of the dominant wave and the second harmonic is less than 10%. Based on this fact, we retain only a few wave components and truncate at $N=2$ for computational efficiency unless otherwise mentioned. The severe truncation in the azimuthal direction limits the application of the model to irregular turbulent flow. However, the model shows good performance in the steady wave and vacillation régimes if we compare our result with the laboratory and numerical experiments by UT89 and UT90.

A renormalization technique to keep the temperature field as $0 \leq \theta \leq 1$ is adopted following Miller and Butler (1991). If we truncate at $N=1$, the model is basically the same as theirs except for the grid resolution and spacing. A two-dimensional model developed by Sugata and Yoden (1992) is used to obtain axi-symmetric flows, and a linearized model by Sugata and Yoden (1991) is also used for the linear stability analysis of the obtained axi-symmetric flow.

Regime transitions are investigated along the line of $\Delta T = 3$ K in Fig. 1; the temperature difference is the same as that imposed by UT89 and UT90 in their laboratory experiment and numerical simulation. The semi-spectral model is integrated for 20 minutes in physical time from an initial condition

which is the flow obtained at slightly different Ω. If the obtained flow is not converged sufficiently to a steady or a vacillating state, additional time integration is done for 20 minutes more. The dominant wavenumber is fixed at $m=5$ from the observation in their laboratory experiment.

3. Results

Figure 3 shows the dependence of the flow régime on the rotation rate Ω obtained with the present semi-spectral model (dots), together with the results in laboratory experiment (open circles) and in numerical simulation (open squares) obtained by UT89. The ordinate is the inward heat flux (scale of the left side), or the Nusselt number (scale of the right side). For small Ω, only the axi-symmetric steady flow is obtained; the heat flux decreases monotonously with increasing Ω. The axi-symmetric flow becomes unstable at $\Omega=0.53$ rad/s, and a three-dimensional steady wave solution is obtained in time-integrations. The heat flux increases from 5.5 J/s to 14.8 J/s at this transition.

Branching of steady wave solutions was explored with changing the external parameter Ω. If Ω is decreases, the régime transition from the steady wave solution to axi-symmetric flow takes place at $\Omega=$ 0.45 rad/s. Therefore the present model has hysteresis between $\Omega=0.45$ rad/s and 0.53 rad/s; two stable solutions are obtained for the same external conditions depending on the initial condition. The numerical simulation by UT89 shows similar hysteresis although their laboratory experiment does not show it explicitly.

If Ω is increased, the steady wave solution becomes unstable at $\Omega=1.12$ rad/s, and vacillation solutions are obtained for higher rotation rates than that. The heat flux fluctuates purely periodically in the vacillation régime and its variable range and time mean are shown in Fig. 3. The variable range of the heat flux fluctuation increases with increasing Ω. A single numerical simulation of the vacillation at Ω $=1.2$ rad/s by UT90 has comparable fluctuation of the heat flux. (They did not show the heat flux in the laboratory experiment for this vacillation.)

The spatial structure of steady wave solutions resembles qualitatively that obtained by Williams (1971, 1972) with different experimental parameters and different grid resolutions, and resembles quantitatively that obtained by UT89 with the same experimental parameters but a different model. Only the streamfunction of the deviatoric horizontal velocity field is shown in Fig. 4 for the steady wave solution at $\Omega=0.45$ rad/s, which is very close to the critical value for the transition. The streamfunction field shows a typical pattern of baroclinic annulus waves; for example, westward tilt of the minimum (maximum) phase with height. The higher harmonic of $n=2$ is not negligible, particularly in middle and

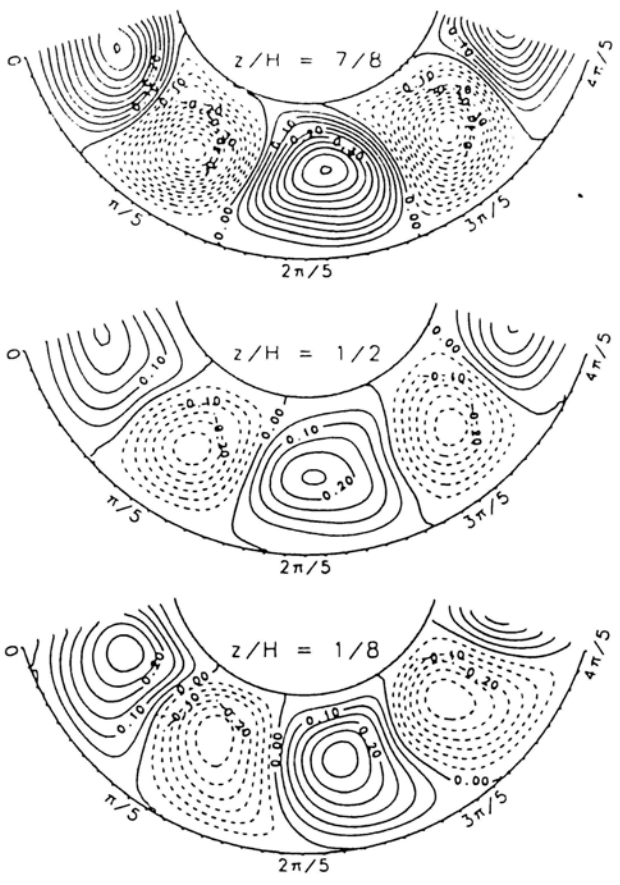

Fig. 4. The streamfunction for the deviatoric horizontal velocity field at three levels. $\Omega=0.45$ rad/s. Positive regions indicate clockwise circulation. The unit is cm^2/s.

upper layers; cyclonic circulation is more intensive than anti-cyclonic circulation and the azimuthal extent of the former is narrower. Tilts of the phase lines in a radial direction indicate non-separable nature in the instability of baroclinic axi-symmetric flow with lateral shear.

In order to investigate the flow régime transitions in the present model further, we take notice of the spatial symmetry of the flow field. The flow field is expanded in an appropriate orthogonal functions, using a Fourier-Bessel series for the present annular geometry, for comparison with Lorenz's results (1962, 1963). The radial structure of some of the lowest modes for the streamfunction is shown in Fig. 5: axisymmetric components (a), wave components for the dominant wave (b), and for the first higher harmonic (c).

Figure 6 shows the amplitude of these components for the streamfunction at the mid-depth for each Ω. The dominant wave has the same order of amplitudes as the axi-symmetric components, but the first higher harmonic is one order smaller than the dominant wave. The first radial mode in each component has the largest amplitude and other modes

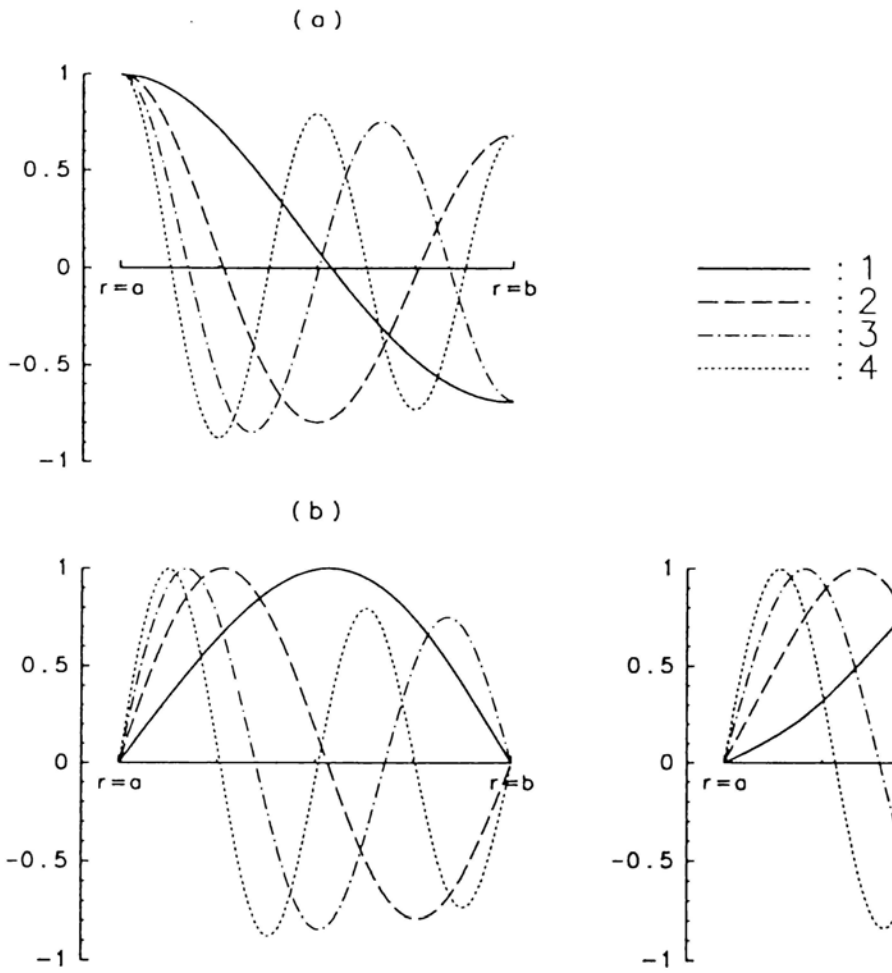

Fig. 5. Radial structure of four lowest modes of the orthogonal functions (Fourier-Bessel functions). (a) the axi-symmetric part, (b) the dominant wave of $m=5$, and (c) its first higher harmonic ($mn=10$).

have small but non-zero amplitudes. Note that all of the solutions we obtained have both odd and even radial modes, in contrast to Lorenz's (1963) result. A steady wave solution with only odd radial mode(s) (R_1 in Fig. 2) can exist as well as that with both modes (R_{12}) in the Lorenz model. Near the transition point $\Omega=0.45$ rad/s, each amplitude varies as $a\sqrt{\Omega}+b$ (a and b are constants), which dependence on Ω reminds us of the limit point of steady solutions (Matsuda, 1983). Moreover, the regime transition from steady wave to vacillation has basic characteristics of Hopf bifurcation; bifurcation of a periodic solution from a steady solution as the latter loses its stability.

The phase relation between any two modes in vacillation is well described by a trajectory projected onto a plane in phase space, which presentation was originally introduced by Lorenz (1963). Figure 7 shows the periodic trajectory of vacillations for $\Omega=1.14$–1.3 rad/s projected onto $\psi_{k0}-\psi_c$ plane where ψ_{k0} and ψ_c have similar definitions to these of Lorenz (1963): ψ_{k0} is the amplitude of the first mode of the dominant wave and ψ_c that of the second axi-symmetric mode. Clearly it is an unsymmetric vacillation (UV) in Lorenz's classification because of the asymmetry of the trajectory with respect to $\psi_c=0$. The present model does not have any correspondence to the pairing of unsymmetric vacillations with opposite sign of even modes obtained in the Lorenz model (1963) (UV' and UV'' in Fig. 2); only one unsymmetric vacillation is obtained for a given external parameter. Nearly elliptic trajectories indicate that the fluctuation of ψ_{k0} leads slightly that of ψ_c for $\Omega\leq 1.2$ rad/s, while it lags slightly for $\Omega=1.25$ and 1.3 rad/s.

The period of the vacillation is 50 s at $\Omega=1.14$ rad/s, and increases slightly up to 56 s at $\Omega=1.3$ rad/s. The period is a half of that obtained by UT90; their result is suggestive of a period-doubling (sub-harmonic) bifurcation of the vacillation solution with the same period of 50 s. We did not obtain any example of such a period doubling nor a non-periodic (chaotic) solution for $\Omega\leq 1.3$ rad/s.

4. Discussion

The régime transitions from steady axi-symmetric

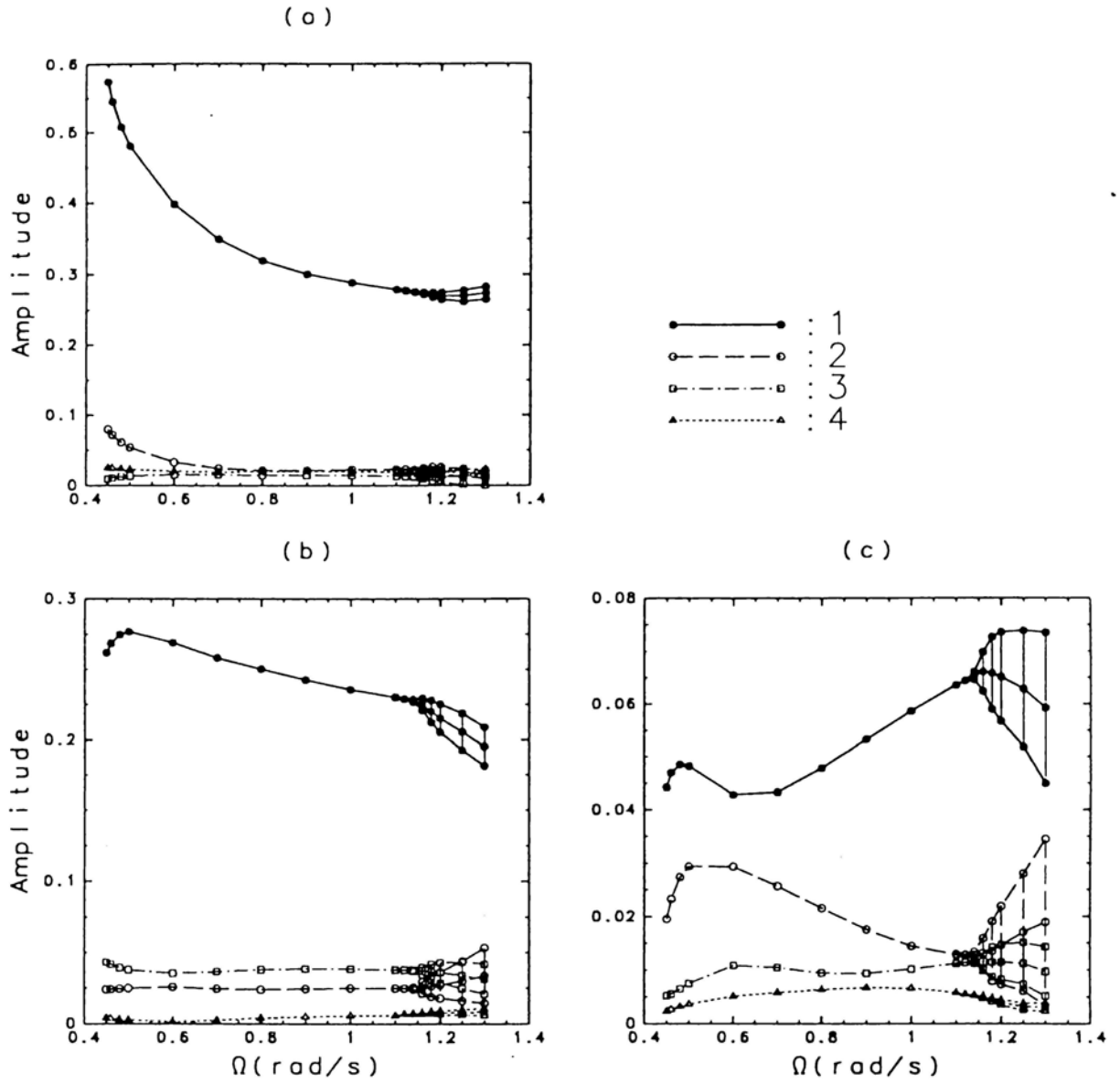

Fig. 6. The amplitude of each mode of the streamfunction for the horizontal velocity at the mid-depth. (a) the axi-symmetric part, (b) the dominant wave of $m=5$, and (c) its first higher harmonic ($mn=10$).

flow to vacillation obtained in this study are summarized in a schematic bifurcation diagram (Fig. 8). A two-dimensional axi-symmetric solution (denoted by H) is obtained for any Ω as in Sugata and Yoden (1992), but it becomes unstable at a certain value of Ω (the point A). An exponentially growing perturbation is obtained by time integrations of the linearized model with respect to the basic axi-symmetric flow. The streamfunction of the horizontal velocity of the growing perturbation near the transition point A is shown in Fig. 9. The spatial pattern of the perturbation differs qualitatively from that of the steady wave solutions (R_{12}^{m+2m}) as shown in Fig. 4, particularly in lower layers. Here, the subscript 12 of R_{12}^{m+2m} stands on both odd and even radial modes, and the superscript $m+2m$ stands on both the dominant wave and its higher harmonics. Note that the basic flow is stable for other wave perturbations except for the wavenumber 5. Non-linear time-integrations of the present model from an initial condition of the unstable basic axi-symmetric flow with the growing perturbation show attraction to the steady wave solution R_{12}^{m+2m}. No stable solution similar to the growing linear perturbation is obtained. Therefore it is concluded from the bifurcation theory (Matsuda, 1983) that this is a subcritical bifurcation of an *unstable* steady wave solution at the point A as denoted by a dashed line R_{12}^{m}.

The steady wave solution (R_{12}^{m+2m}) disappears at another transition point B, which is classified as a limit point from Figs. 3 and 6. Hysteresis is realized by the coexistence of the subcritical bifurcation

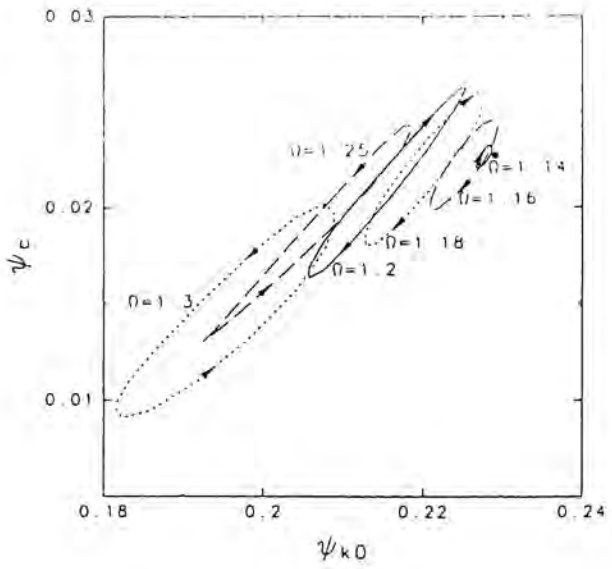

Fig. 7. Trajectories of vacillation projected onto a $\psi_{k0}-\psi_c$ plane (see text) for six rotation rates $\Omega=1.14$–1.3 rad/s. The dot indicates a stable steady wave solution near the critical point $\Omega=1.12$ rad/s.

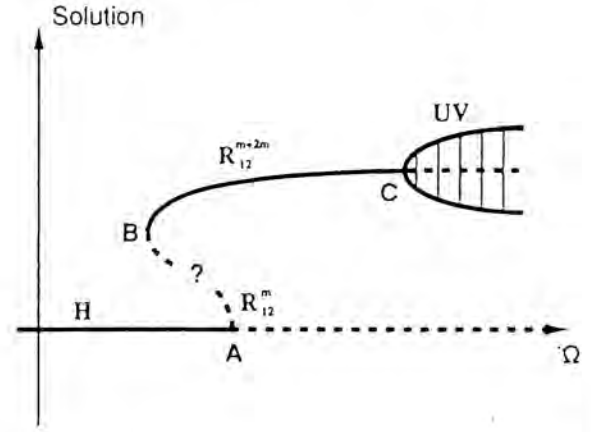

Fig. 8. Bifurcation diagram for the present result. The solid line is a branch of stable solutions, dashed line that of unstable ones. See text for details.

point A and the limit point B. The unstable branch of the steady wave from the point B may not be directly connected with the unstable branch R_{12}^m because of the existence of the higher harmonics. However, it is practically impossible to search for the unstable solutions computationally as in the Lorenz model, because the present model is a huge nonlinear system with degree of freedom of $O(10^5)$.

We did not obtain any steady wave solution which consists of only odd radial modes, in contrast to that in the Lorenz (1963) model (R_1 in Fig. 2). The reason is the difference in the symmetry group of the orthogonal functions. Lorenz (1963) assumed

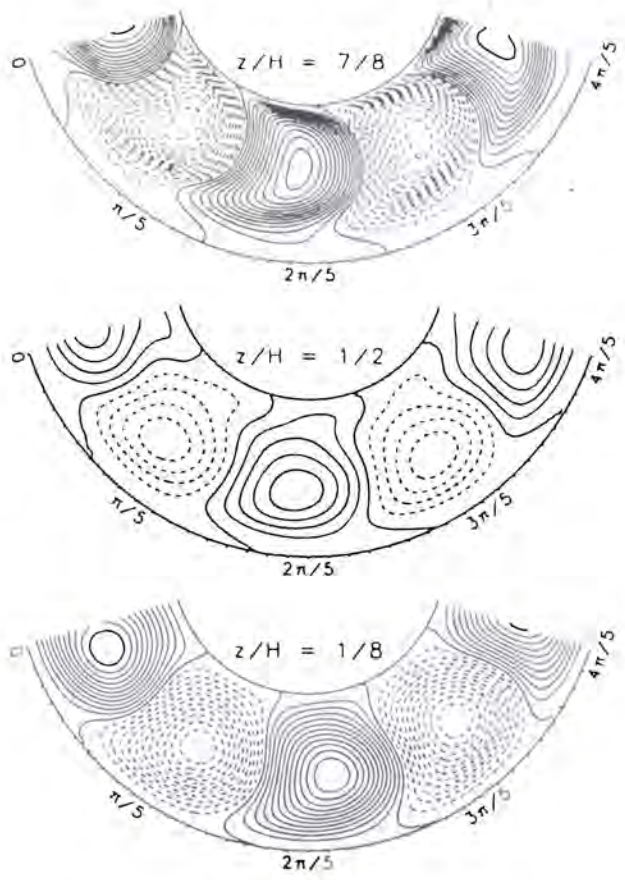

Fig. 9. As in Fig. 4, except for the most unstable wave perturbation obtained in the linear stability analysis of the axi-symmetric flow at $\Omega=0.54$ rad/s. The contour intervals are the same among the three figures.

an infinite channel to expand the field variables in a double-Fourier series, which are divided into two symmetric groups depending on the lateral structure of each mode; symmetric and anti-symmetric groups with respect to the center of the channel (see Yoden, 1985). The symmetric group constitutes a subsystem of the system, setting the anti-symmetric group to be zero. However, the present model does not have such a sub-system because of the spatial structure of the Fourier-Bessel series (Fig. 5). Therefore any steady solution in which some modes are equal to zero was not obtained. In other words, the stepwise transition from the symmetric steady wave solution (R_1) to the mixed wave solutions (R'_{12} and R''_{12}) in the Lorenz model is a spurious result due to the assumption of an infinite channel; such a transition is not possible in the annular geometry.

A vacillation solution bifurcates at the point C in Fig. 8, which is a counterpart of the point D′ (D″) in Fig. 2. The steady wave solution R_{12}^{m+2m} becomes unstable at that point indicating a Hopf bifurcation. A period-doubling bifurcation nor other transition routes to non-periodic solutions were not

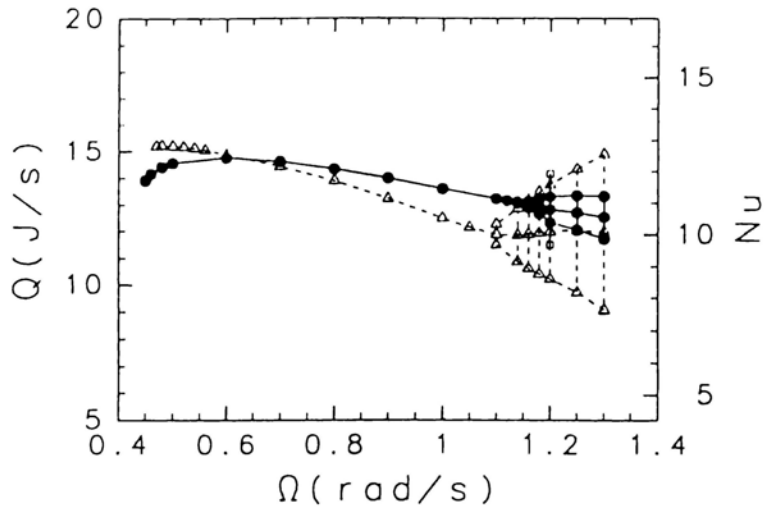

Fig. 10. As in Fig. 3, except that the symbol △---△ is for another truncation $N=1$.

obtained for $\Omega \leq 1.3$ rad/s. If the rotation rate is increased further, such transitions to an irregular régime might be obtained in the present model, even though the assumption of azimuthal periodicity may not be very appropriate.

To investigate the rôle of the first higher harmonics in the transitions of flow régimes, another model with more severe truncation of $N=1$ is used, which is basically the same as that used by Miller and Butler (1991). Figure 10 is a comparison of the inward heat flux for the two results obtained from $N=1$ (dashed line) and $N=2$ (solid line) truncations. Both of the hysteresis between the axi-symmetric and steady wave régimes and bifurcation of vacillation from the steady wave branch are obtained, even in the truncation of $N=1$. The first higher harmonic is not necessary for a qualitative understanding of the transitions from axi-symmetric flow to vacillation, although it is not negligible for quantitative arguments. The spatial structure obtained in these two models is compared with those obtained in the fully three-dimensional model and in the laboratory experiment by UT90. Figure 11 shows an azimuthal vertical cross section of the deviatoric temperature at the mean radius of the annulus for the steady wave at $\Omega=0.6$ rad/s. The $N=2$ model (a) gives a very similar result as the full model (c) and the laboratory experiment (d). However, the $N=1$ model (b) with no higher harmonics has some differences, particularly in the upper layers.

Similar numerical studies were done along the line of $\Delta T=8$ K in Fig. 1, and qualitatively similar results to those for $\Delta T=3$ K were obtained. Any amplitude vacillation adjacent to a transition to the steady axi-symmetric flow, which is observed in the laboratory experiments (Fig. 1), is not obtained in the present model. It is conjectured from bifurcation theories that the sudden disappearance of the vacillation comes from a limit point of a pair of periodic solution (vacillation) branches (see Fig. 1 in Yoden, 1987), but a more sophisticated model is necessary to obtain such a régime transition.

5. Conclusion

Stepwise transitions in flow régimes observed in some of the rotating annulus experiments with radial differential heating were investigated numerically with a semi-spectral model of a three-dimensional Navier-Stokes equation with a Boussinesq approximation, and the results were interpreted with bifurcation theories. Experimental conditions are identical to the laboratory experiments by Tamaki and Ukaji (1985) and Ukaji and Tamaki (1989, 1990). The rotation rate Ω is changed as a bifurcation parameter with other conditions fixed. A schematic bifurcation diagram shown in Fig. 8 is obtained as a summary of our results. Steady, two-dimensional axi-symmetric flow (denoted by H) exists for any Ω, but it becomes unstable at a critical value of Ω (the point A) with respect to a wave perturbation. However, this is a sub-critical bifurcation because no stable steady wave solution similar to the linear growing-mode is obtained near the bifurcation point. Instead, a finite-amplitude steady wave solution (R_{12}^{m+2m}) is obtained in time-integrations at the bifurcation point, the spatial structure of which is different from the linear mode. The steady wave solution disappears at another critical point B at a smaller Ω than the bifurcation point. That is, hysteresis exists between these two critical points; the sub-critical bifurcation point (A) and the limit point (B). As Ω is increased, the steady wave solution becomes unstable at the point C in Fig. 8 with respect to a perturbation which fluctuates purely periodically. Periodic solutions well known as a tilted-trough vacillation are obtained for larger Ω than this

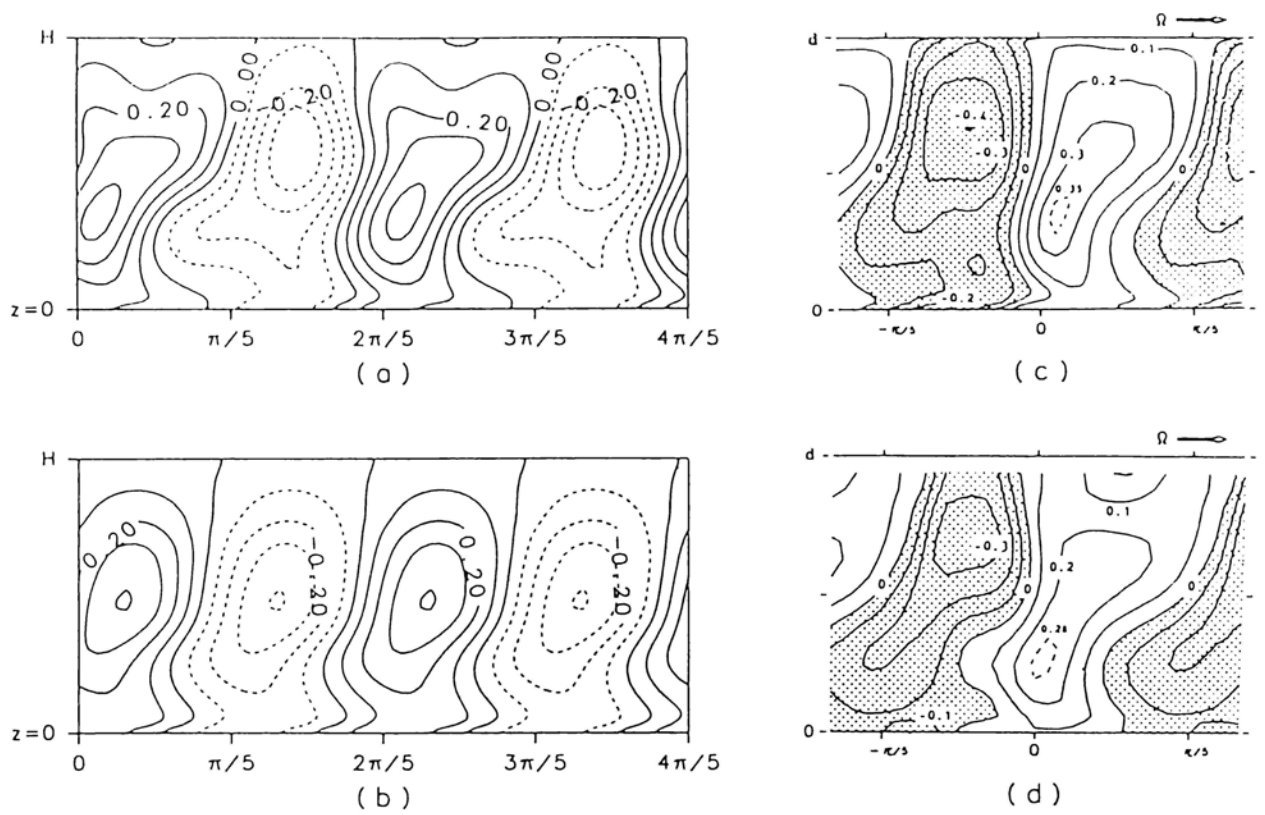

Fig. 11. Azimuthal-vertical cross sections of deviatoric temperature at the mid-radius for $\Omega = 0.6$ rad/s: (a) the present model of $N = 2$, (b) that of $N = 1$, (c) the numerical model by Ukaji and Tamaki (1989), and (d) the laboratory experiment by them. The unit is K.

critical value. This is interpreted as a Hopf bifurcation from the trajectories shown in Fig. 7.

Contrary to the Lorenz (1963) model of a low-order system, bifurcation in the steady wave branch is not obtained in the present model. The spurious bifurcation in the Lorenz model (the point B in Fig. 2) arises from the spatial symmetry of the flow domain. In the geometry of an infinite channel assumed by Lorenz (1963), a group of symmetric components with respect to the mid-channel constitutes a sub-system of the low-order system, and a symmetry-breaking bifurcation takes place with respect to anti-symmetric components. However, such a sub-system does not exist for the present annular geometry, because of the characteristics of the Fourier-Bessel series (Fig. 5) which is the appropriate orthogonal function for this geometry.

Analysis of transitions from vacillation to the irregular régime remains as our future study, for which a full three-dimensional numerical model is necessary.

Acknowledgments

The authors wish to thank Professor I. Hirota for his valuable comments during the work. This study was partly supported by the Grant-in-Aid for Scientific Research, the Ministry of Education, Science, and Culture of Japan. The GFD-DENNOU Library was used for drawing the figures.

References

Fein, J.S., 1973: An experimental study of the effects of the upper boundary condition on the thermal convection in a rotating, differentially heated cylindrical annulus of water. *Geophys. Fluid Dyn.*, **5**, 213–248.

Fowlis, W.W. and R. Hide, 1965: Thermal convection in a rotating annulus of liquid: effect of viscosity on the transition between axisymmetric and non-axisymmetric flow regimes. *J. Atmos. Sci.*, **22**, 541–558.

Fultz, D., R.R. Long, G.V. Owens, W. Bohan, R. Kaylor and J. Weil, 1959: Studies of thermal convection in a rotating cylinder with some implications for large-scale atmospheric motions. *Meteor. Monographs*, **4-21**, 104 pp.

Ghil, M. and S. Childress, 1987: *Atmospheric dynamics, dynamo theory, and climate dynamics*. Springer-Verlag, 73–124.

Hide, R. and P.J. Mason, 1975: Sloping convection in a rotating fluid, *J. Adv. Phys.*, **24**, 47–100.

Hignett, P., 1985: Characteristics of amplitude vacillation in a differentially heated rotating fluid annulus. *Geophys. Astrophys. Fluid Dyn.*, **31**, 247–281.

Hignett, P., A.A. White, R.D. Carter, W.D.N. Jackson and R.M. Small, 1985: A comparison of laboratory measurements and numerical simulations of

baroclinic wave flows in a rotating cylindrical annulus. *Quart. J. Met. Soc.*, **111**, 131–154.

Lorenz, E.N., 1962: Simplified dynamic equations applied to the rotating-basin experiments. *J. Atmos. Sci.*, **19**, 39–51.

Lorenz, E.N., 1963: The mechanics of vacillation. *J. Atmos. Sci.*, **20**, 448–464.

Matsuda, Y., 1983: Classification of critical points and symmetry-breaking in fluid phenomena and its application to dynamic meteorology. *J. Meteor. Soc. Japan*, **61**, 771–788.

Matsuda, Y. and S. Yoden, 1985: Meteorology and catastrophe—Multiple equilibria in dynamic meteorology (in Japanese). Note on Meteorological Research, **151**, 145 pp.

Miller, T.L. and K.A. Butler, 1991: Hysteresis and the transition between axisymmetric flow and wave flow in the baroclinic annulus. *J. Atmos. Sci.*, **48**, 811–823.

Pfeffer, R.L., G. Buzyna and R. Kung, 1980: Time-dependent modes of behavior of thermally driven rotating fluids. *J. Atmos. Sci.*, **37**, 2129–2149.

Quinet, A., 1973a: The structure of non-linear processes. *Tellus*, **25**, 536–544.

Quinet, A., 1973b: Non-linear mechanisms in a non-conservative quasi-geostrophic flow which possesses 30 degrees of freedom. *Tellus*, **25**, 545–559.

Sugata, S. and S. Yoden, 1991: The effects of centrifugal force on the stability of axisymmetric viscous flow in a rotating annulus. *J. Fluid Mech.*, **229**, 471–482.

Sugata, S. and S. Yoden, 1992: Steady axi-symmetric flow due to differential heating in a rotating annulus and its dependence on experimental parameters. *J. Meteor. Soc. Japan*, **70**, 1005–1017.

Swinney, H.L. and J.P. Gollub (eds.), 1981: *Hydrodynamic instabilities and the transition to turbulence.* Springer-Verlag, 292 pp.

Tamaki, K. and K. Ukaji, 1985: Radial heat transport and azimuthally averaged temperature fields in a differentially heated rotating fluid annulus undergoing amplitude vacillation. *J. Meteor. Soc. Japan*, **63**, 168–179.

Ukaji, K. and K. Tamaki, 1989: A comparison of laboratory experiments and numerical simulations of steady baroclinic waves produced in a differentially heated rotating fluid annulus. *J. Meteor. Soc. Japan*, **67**, 359–374.

Ukaji, K. and K. Tamaki, 1990: A numerical study of tilted-trough vacillation observed in a differentially heated rotating fluid annulus. *J. Meteor. Soc. Japan*, **68**, 447–460.

Williams, G.P., 1967a: Thermal convection in a rotating fluid annulus: part 1. The basic axisymmetric flow. *J. Atmos. Sci.*, **24**, 144–161.

Williams, G.P., 1967b: Thermal convection in a rotating fluid annulus: part 2. Classes of axisymmetric flow. *J. Atmos. Sci.*, **24**, 162–174.

Williams, G.P., 1969: Numerical integration of the three-dimensional Navier-Stokes equations for incompressible flow. *J. Fluid Mech.*, **37**, 727–750.

Williams, G.P., 1971: Baroclinic annulus waves. *J. Fluid Mech.*, **49**, 417–449.

Williams, G.P., 1972: The field distributions and balances in a baroclinic annulus wave. *Mon. Wea. Rev.*, **100**, 29–41.

Yoden, S., 1979: Some dynamical properties of non-linear baroclinic waves in a quasi-geostrophic model. *J. Meteor. Soc. Japan*, **57**, 493–504.

Yoden, S., 1985: Multiple stable states of quasi-geostrophic barotropic flow over sinusoidal topography. *J. Meteor. Soc. Japan*, **63**, 1031–1045.

Yoden, S., 1987: Bifurcation properties of a stratospheric vacillation model. *J. Atmos. Sci.*, **44**, 1723–1733.

セミスペクトルモデルを用いた回転水槽中の流れパターンの遷移に関する数値的研究

菅田誠治[1]・余田成男
(京都大学理学部)

いくつかの回転水槽実験で得られた軸対称流—定常波動—バシレーションという段階的な流れパターンの遷移を、3次元ブシネスク流体のセミスペクトルモデルを用いて調べ、分岐理論をもとに考察した。軸対称流—定常波動間の遷移は、ヒステリシスによって特徴づけられる。すなわち、得られた定常波動は、軸対称流が不安定化するところで、そこから分岐するのではなく、別の臨界点（極限点）が存在し、そこで定常波動解が消滅する。また定常波動—ティルティッド・トラフ・バシレーション間の遷移は、定常波動が不安定化するところでのHopf分岐（周期解の定常解からの分岐）によると考えられる。

[1]現在所属：国立環境研究所

投稿予定稿

Lagrangian motion and heat transport in a steady baroclinic annulus wave

By SEIJI SUGATA

The National Institute for Environmental Studies,

Tsukuba,Ibaraki 305, JAPAN

and

SHIGEO YODEN

Department of Geophysics,

Kyoto University,

Kyoto 606-01, JAPAN

Abstract

Lagrangian motion of a fluid particle is investigated for a steady wave in a rotating annulus of fluid. Obtained trajectory shows a chaotic nature but has several typical organized behavior depending on its position in the annulus. The annulus of fluid is divided into seven regions according to the characteristics of the particle motion: an upper-level jet, a lower-level jet, a cyclonically trapped-region, an anticyclonically trapped-region, an inner boundary layer, an outer boundary layer, and a lower boundary layer. Cores of the cyclonically trapped-region and the anticyclonically trapped-region are found to be nearly isolated from the others.

Residence time of the fluid particle in each region and frequency of the transition between the regions are analyzed. A cyclic route of transition which is remarkably preferred is found: the outer boundary layer $\rightarrow$ the upper-level jet $\rightarrow$ the inner boundary layer $\rightarrow$ the lower-level jet *or* the lower boundary layer $\rightarrow$ the outer boundary layer.

Temperature of the fluid particle changes largely in both the inner boundary layer and the outer boundary layer through vertical motions but it changes little in the other regions. Moreover, little correlation exists between the particle's approach toward outer wall and its warming in the jet regions. Lagrangian description of the horizontal heat transport in the steady wave is that a fluid particle which obtained heat during the upward motion in the outer boundary layer is advected nearly adiabatically across the interior region of the fluid and releases the heat during the downward motion in the inner boundary layer. Inward heat flux estimated from the Lagrangian view is comparable with the total inward heat flux obtained in the Eulerian representation.

1 Introduction

Even in a regular flow, Lagrangian motion of fluid particles may be chaotic. Such a regular flow falls into two types; three-dimensional steady flows and periodic two-dimensional flows. An example of the former is a Arnold-Beltrami-Childress (ABC) flow (Dombre et al., 1986). Although ABC flow is a three-dimensional steady flow simply described by linear combination of trigonometric functions with three real parameters, streamlines of particle motions have a complicated Lagrangian structure, and the fluid is divided into an ordered region and a chaotic region in the Poincaré section. An example of the latter is two-dimensional traveling waves with temporally periodic modulation studied by Weiss and Knobloch (1989). They examined a particle transport and mixing in the flow and showed that the fluid is divided into three regions in the frame moving with the wave: a trapped region where particles are carried along with the wave, an untrapped region where particles are left behind by the wave, and a separatrix layer between the two regions where particles chaotically alternate between being trapped and untrapped.

Steady waves in the rotating annulus of fluid with radial differential heating have been investigated in many laboratory experiments (see, *e.g.*, Hide and Mason, 1975). Lagrangian motion in the steady waves may be chaotic because of the three-dimensionality of the flow. However, most of the studies of the steady waves have been done from the Eulerian view and there are only a few studies as to the Lagrangian motion in the steady wave. Figure 1 shows a streak photograph of the top surface of the fluid taken by a camera mounted on the rotating apparatus (Hide and Mason, 1975), where an upper surface jet is traced by long streaks. Trajectories of the fluid motion in the interior were observed in the laboratory experiment by Sakai (1990). Figure 2 is a projection of the trajectories

on a meridional plane, which shows elliptical orbits whose major axes incline up toward the inner wall. Particles rise near the inner cold wall and fall near the outer warm wall. He suggested that the particles in a jet stream move nearly adiabatically with outward motion along a ridge of an iso-therm surface and inward motion along a trough, which may give the observed elliptical orbits in the meridional plane. One of the motivation of this paper is to investigate Lagrangian motion in a three-dimensional steady wave solution in a rotating annulus of fluid numerically.

The other subject focused in this paper is heat transport in the steady wave. A baroclinic wave, such as the steady wave in the rotating annulus of fluid, transports heat toward inward (generally from warm area to cold area), which is commonly explained by correlation between a warm (cold) temperature and inward (outward) velocity in the azimuthal direction. On the analogy of this explanation, many of us (including the authors) have comprehended that every one cycle of wavy motion in a jet stream in the steady wave transports heat: the particle in the jet stream obtains heat near the warm boundary, moves inward along the jet stream, releases the heat near the cold boundary, and moves outward again along the jet stream. Figure 3 is an illustration taken from a textbook of earth science for high school students (Umino et al., 1992), with which the poleward heat transport by westerly jet in the northern hemisphere is illustrated in the same manner. Another motivation of this paper is to discuss propriety of the comprehension of the heat transport for the steady wave in the rotating annulus of fluid.

We numerically trace a fluid particle in a steady wave for a long time interval in order to investigate the Lagrangian motion of the particle and its temperature change following the particle motion. One of the steady wave solutions obtained by Sugata and Yoden (1993) is used for the present study. We will try to get a Lagrangian description

of the heat transport in the steady wave, to which little attention has been paid.

2 Particle motion in a steady wave solution

2.1 *A steady wave solution*

Sugata and Yoden (1993) developed a semi-spectral model and obtained some steady wave solutions. One of the steady wave solutions is focused and investigated in this study. Experimental conditions for the steady wave we investigated are as follows. The dimensions of the apparatus are: inner radius $a = 4.5$ cm, outer radius $b = 9.7$ cm, and height of the fluid $d = 8.0$ cm. Top surface of the working fluid of water is in contact with a free-slip rigid lid and the other three surfaces are non-slip rigid boundaries. Inner and outer walls are kept at different temperature to maintain the difference $\Delta T = 3$ K, and the top and bottom boundaries are thermally insulating. The rotation rate Ω of the apparatus is 0.6 rad/s. The thermal Rossby number $Ro_T = 6.55 \times 10^{-1}$ and the Taylor number $Ta = 9.15 \times 10^6$. The dominant wavenumber of the steady wave is supposed as $m = 5$. Refer to Sugata and Yoden (1993) for further model description and numerical procedure. The wave obtained drifts eastward relative to the apparatus at a constant rotation rate $\omega = 1.67 \times 10^{-2}$ rad/s, which is about 1/36 times as large as the rotation rate of the apparatus Ω. The term 'east' will be used as meaning the azimuthal direction of the rotation of the apparatus from now on.

All computed variables are velocity components (u, v, w), normalized temperature θ, and pressure (divided by the mean density) p. The velocity components (u, v, w) are defined in the cylindrical coordinates (r, λ, z), where r, λ, and z are the radius from the axis of the rotation, the azimuth relative to the apparatus, and the height from the

bottom, respectively.

Structure of steady waves in the rotating annulus of fluid has been clarified numerically with nonlinear models based on the Navier-Stokes equations for Boussinesq fluid (Williams, 1969, 1971, 1972, Ukaji and Tamaki, 1989). Therefore, we here briefly mention the structure of the steady wave investigated in this study. Figure 4 shows (a) (u, v), (b) w, (c) p, and (d) θ, over two wavelengths at two different levels; (I) an upper level $z/d = 3/4$ and (II) a lower level $z/d = 1/8$. A strong westerly jet stream is dominant at the upper level (Fig. 4(a)-I). At the lower level, intensity of the horizontal flow is weaker than that at the upper level owing to the presence of the lower non-slip boundary, and a jet stream is not clear (Fig. 4(a)-II). The horizontal flow is almost parallel with isobars at both levels (Fig. 4(c)) by geostrophy. Axes of the pressure wave slopes westward with height. Large downward motion is found in the western side of the low pressure region except for the inner boundary layer at both levels (Fig. 4(b)). Warm regions locate around the inward flow, and cold regions locate around the outward flow (Fig. 4(a) and (d)). This correlation causes inward heat transport by the baroclinic wave.

Figure 4(e) shows the horizontal velocity (u, v') described in the comoving frame with the azimuth $\lambda' = \lambda - \omega t$, where

$$v' = v - r\omega. \tag{1}$$

Figure 4(e) is prepared for convenience to discuss the flow in the frame with λ'. Compared with Fig. 4(a), the anticyclonic circulation in the high pressure regions is clear at the upper level and an easterly jet stream appears clearly at the lower level, which is due to the addition of the easterly 'apparent' velocity to v (Eq. 1). We simply denote λ' by λ from now on.

2.2 *Numerical procedures of tracing*

A fluid particle is released initially at a point corresponding to the center of the westerly jet stream at the level, $z/d = 3/4$, and is traced in the known velocity field of the wave described in the preceding subsection for 100000s.

Movement of the marked particle is obtained by

$$\mathbf{r}(t + \Delta t) = \mathbf{r}(t - \Delta t) + 2\mathbf{V}(\mathbf{r}(t), t)\Delta t, \tag{2}$$

where t and Δt are time and time increment, respectively, and $\mathbf{r}$ and $\mathbf{V}$ are three-dimensional vectors of position and velocity of the particle relative to the apparatus, respectively. The time increment Δt is 5.0×10^{-3}s.

When the particle is not located just at some grid points in the meridional plane, the velocity is linearly interpolated from that of adjacent four grid points in the meridional plane as follows. Suppose $q_{r,z}$, a variable q at a location (r, z) in the meridional plane. When r and z are denoted, with the radial grid interval Δr and the vertical grid interval Δz, as

$$r = a + \Delta r(i + x), \tag{3}$$

$$z = \Delta z(j + y), \tag{4}$$

where i and j are integers and $0 \leq x < 1, 0 \leq y < 1$. Then the variable $q_{r,z}$ is obtained with the variables given in adjacent four grid points by

$$q_{r,z} = (1 - x)(1 - y)q_{i,j} + x(1 - y)q_{i+1,j} + (1 - x)yq_{i,j+1} + xyq_{i+1,j+1}. \tag{5}$$

However, when the particle is within one grid distance from a boundary, the method of the interpolation must be modified to prevent the particle from penetrate the boundary. In this study, the normal velocity component along the boundary is obtained as follows.

For example, the radial velocity within one grid distance from the inner wall, $u_{r,z}(r = \Delta r \cdot x, z = \Delta z(j + y))$, is denoted, with $u_{0,j} = 0$ and $u_{0,j+1} = 0$ on the wall, as

$$u_{r,z} = x^2(1 - y)u_{1,j} + x^2 y u_{1,j+1}. \tag{6}$$

Mass conservation within one grid distance from the wall is kept by adoption of this definition.

2.3 *Trajectory of the particle*

The trajectory of the particle is projected onto (a) r–λ plane, (b) r–z plane, and (c) λ–z plane in Fig. 5. (Note that λ is the azimuthal position in the comoving frame.) Although it intersects itself many times and its complicated structure shows chaotic motion in each figure, some regularity appears there. For example, two predominant wavy streaks which are out of phase with each other in the azimuthal direction appear in Fig. 5(a). The interior region of the meridional section, Fig. 5(b), is occupied by horizontal streak lines which slightly slope up toward the inner wall, and side boundary layers are occupied by vertical streak lines. The azimuthal section, Fig. 5(c), consists almost of horizontal streak lines, while some diagonal streak lines exist.

In order to investigate the trajectory intensively, we partitioned the horizontal section (Fig. 5(a)) into four sections in different layers and piled on the partitioned trajectory within one wavelength of the steady wave in each layer (Fig. 6), and did the azimuthal section (Fig. 5(c)) into seven sections in different radii (Fig. 7) by the same manner. The residence time in each layer is indicated below each section in Figs. 6 and 7. Although the trajectory appears to cover all the area in Fig. 5, these two figures show the presence of two large blank spaces where the particle have hardly passed through;

one occupies the core of low pressure region (marked by A) and the other occupies the core of the high pressure region (marked by B). Only a few spiral streaks stray into these spaces. Some computations (trajectories are not shown) in which the particle was initially released within the blank spaces show that the particle hardly go out from the spaces. These results mean that the exchange of particles hardly occurs between the blank spaces and the other spaces.

We shall now investigate the characteristics of the trajectory in individual section. In Fig. 6, streak lines are almost parallel with each other except for Fig. 6(c). Layers in Fig. 6(a) and (b) correspond to a strong westerly jet stream in the upper level. The streak lines are basically divided into two categories according to their shape and motion indicated. One is streak lines forming approximately closed circles around pressure extremes, where the particle circulates clockwise around the high pressure and anticlockwise around the low pressure. The other is streak lines situated along the jet stream (see also Fig. 4(e)-I) on which the particle is advected eastward. The former corresponds to the trapped region and the latter does to the untrapped region according to the categorization in Flierl (1981).

A layer in Fig. 6(c) includes a steering level of the steady wave. Since horizontal velocity components are smaller than those in the other layers, and besides, the deviatoric vertical velocity is larger in this layer as the characteristics of baroclinic waves, relative importance of the vertical movement compared to the horizontal one is larger (see also Fig. 7). That is the reason this layer can not be clearly divided into a trapped region and an untrapped region in contrast to the other layers.

The particle is advected westward in the untrapped region in the lower layer (Fig. 6(d), and see also Fig. 4(e)-II). The trapped region is smaller than that in the upper

layers. This can be essentially explained by the theory in Flierl (1981). He showed that a trapped region appears when the deviatoric velocity of the wave exceeds the phase velocity of the wave in some area and that the ratio of the region to the whole fluid increases with increasing wave strength. In this study, although the amplitude of the phase velocity of the steady wave relative to zonal mean flow is comparable between the upper and lower layer, the deviatoric azimuthal velocity is smaller in the lower layer and exceeds the phase velocity in smaller area.

In azimuthal sections of the interior region (Fig. 7(b)–(f)), horizontal streak lines are dominant at all heights except the middle layer. On the other hand, many of streak lines are diagonal near the side boundaries (Fig. 7(a) and (g)), which is indicative of large vertical movement within the side boundary layers. The particle is advected westward with downward motion near the inner boundary (Fig. 7(a)), and is advected westward with upward motion near the outer boundary (Fig. 7(g)). The reason the particle goes west in both layers is that the particle moving slowly near the non-slip walls is observed in the comoving frame moving eastward with the wave.

2.4 *Definition of regions*

Time variations of the position (r, λ, z), normalized temperature θ, and pressure p of the particle were investigated. Figure 8 shows these variations from $t = 20000$s to 40000s. Although each variable shows chaotic variation, some typical organized behaviors appear alternatively. Hereafter these behaviors are investigated individually.

When λ increases with time, r oscillates largely with its center of oscillation shifting inward gradually and z oscillates small in the upper layer (see, *e.g.*, the middle between marks (1) and (6) above Fig. 8). The trajectory corresponding to such behavior is shown

by a line between marks (3) and (4) in Fig. 9 in a bird's-eye view, on which the particle is advected eastward by the westerly jet stream. We will refer to such an untrapped region in the upper layer as an 'upper-level jet'. The particle typically stays in this region during making one round of the annulus.

When λ decreases with time, r oscillates largely but with its center shifting outward gradually and z oscillates small in the lower layer (see, *e.g.*, a period around (1) or (6) above Fig. 8). Lines during (1)–(2) and (5)–(6) in Fig. 9 correspond to parts of such behavior. The particle is advected westward by the lower easterly jet stream. We will refer to such an untrapped region in the lower layer as a 'lower-level jet'. The particle typically stays in this region during making two rounds of the annulus.

When λ oscillates around a nearly constant value, r also oscillates with its center changing little (see, *e.g.*, periods indicated by marks (a)–(d) above Fig. 8). Figure 10 shows a bird's eye view of the trajectory during these periods. The particle is trapped around the high-pressure extreme and spirals clockwise up during (a)–(b) and down during (b)–(c). On the other hand, it is trapped around the low-pressure extreme and spirals up anticlockwise during (c)–(d). We will refer to the former as an 'anticyclonically trapped-region' and the latter as a 'cyclonically trapped-region'.

When the particle keeps its position within a certain distance from a boundary for a while, it is confined in the boundary layer. The trajectory in Fig. 11 corresponds to such period. The particle is confined in the inner boundary layer during (A)–(B), where large downward motion is shown. We will refer to this as an 'inner boundary layer'. Then the particle enters the lower boundary layer and goes outward during (B)–(C). We will refer to this as a 'lower boundary layer'. The particle enters the outer boundary layer at last and shows large upward motion during (C)–(D). We will refer to this as an 'outer

boundary layer'.

The particle motion falls into the seven regions defined above: the upper-level jet, the lower-level jet, the cyclonically trapped-region, the anticyclonically trapped-region, the inner boundary layer, the outer boundary layer, and the lower boundary layer. The whole period is divided into 459 episodes under the definite criterion. Table 1 lists the result: total number of appearance, total residence time, average residence time for one stay, and average temperature variation for one stay for each region.

The total number of appearance shows that the most frequently preferred regions are the upper-level jet, the inner boundary layer, and the outer boundary layer. The lower-level jet is the next most preferred after these three regions. The sum of these four regions account for about four-fifth of the total episodes.

Since average residence times for one stay for both trapped-regions are longer than those for other regions, total residence times are relatively large for the regions in spite of the small total appearance numbers. That is because the particle in the regions repeats the spiral motion with smaller speed than that in the other regions.

Average residence time for the outer boundary layer are longer than that for the inner boundary layer because the vertical velocity in the outer boundary layer is smaller than that in the inner boundary layer due to the curvature of the annulus.

The temperature change will be discussed in the following section.

2.5 *Transition of the region*

The number of transition from one region to another region is counted in Table 2 as a transition matrix. Much more frequently preferred are two transitions; the outer boundary layer $\rightarrow$ the upper-level jet and the upper-level jet $\rightarrow$ the inner boundary layer. In

addition, four transitions occur more frequently than the others; the inner boundary layer → the lower-level jet, the lower-level jet → the outer boundary layer, the inner boundary layer → the lower boundary layer, and the lower boundary layer → the outer boundary layer. These six transitions indicated by boldface in the table account for more than three-fourth of all the transitions, and form the cyclic route of the transition, where the route partly bifurcates; the outer boundary layer → the upper-level jet → the inner boundary layer → the lower-level jet *or* the lower boundary layer → the outer boundary region. This cyclic route is illustrated also by thick arrows in Fig. 12. If the lower-level jet and the lower boundary layer are regarded as the same region, the numbers of transitions associated with the unified region are comparable to those associated with the upper-level jet. Table 3 is a transition matrix that picks out the transition concerning with both the side boundary layers. This shows the particle goes back and forth 90 times in the whole period, and Fig. 12 means that the most of the 90 times is carried by the typical cyclic route mentioned above.

3 Lagrangian view of the heat transport

Total inward heat flux in the present wave is about 0.19 cm^3/s, as is shown in Fig. 13. Conductive heat flux plays a vital role near the side boundaries and mean circulation transports heat between the side boundary layers and the adjacent regions. Deviatoric flux is very important in the interior region. Around the mean radius, roughly 3/2 of the total inward flux is transported by the deviatoric flux and the remains of $-1/2$ is transported by mean circulation flux with indirect circulation.

It is not clear how the temperature of the particle changes with its motion and

how the variation contributes to the total inward heat transport. In this section, we investigate time variation of the temperature following the particle to examine where the particle obtains and releases heat and to clarify a mechanism of the heat transport from the Lagrangian view.

Figure 14 shows the time variation of the temperature following the particle and its time derivative during t = 25000s - 32000s. This period includes the periods when the trajectory was shown in Figs. 10, 9, and 11. Remarkably large changes of the temperature occur when the particle stays in the side boundary layers with large vertical motions. Though temperature varies also in other regions, its variation is rather smaller than that in the side boundary layers. This is confirmed also by values of average temperature variation for one stay shown in Table 1. The values in the side boundary layers are more than 0.6 and much larger than those in other regions. Even the next largest value, 0.12, in the cyclonically trapped-region is about one-fifth of that in the side boundary regions.

As for the time variation during an individual episode in each region, there is no correlation between the adjacency of the particle toward the outer (inner) boundary and the increase (decrease) of the temperature in both the jet regions. Therefore, every one cycle of the motion in these regions does not contribute to the total inward heat transport. Although there is some correlations in both the trapped-regions (see around t = 29500s or 31500s in Fig. 14), a sum of individual inward heat transport due to every one cycle with the correlation is apparently much smaller than that due to the temperature changes in the side boundary layers.

Fig. 15 shows the trajectory during the lower-level jet. The length of perpendicular lines drawn from the trajectory to an isothermal surface shows that the particle moves nearly along the surface, in other words, nearly adiabatically. The particle moves inward

along a trough of the isothermal surface and outward along a ridge. This supports the validity of the suggestion by Sakai (1990) with Fig. 2.

4 Discussion

The preceding two sections clarified the following. The particle's motion falls into seven regions according to its position, and the particle transits among the regions. There is remarkably frequently preferred route of the transition, which departs from the outer boundary layer for the inner boundary layer via the upper-level jet and then comes back to the outer boundary layer via the lower two regions, i.e., the lower-level jet and the lower boundary layer. The particle gets and releases heat in the side boundary layers and moves nearly adiabatically in other regions. From these results, the inward heat transport in the steady wave can be illustrated in the Lagrangian representation as follows. The particle gets large quantity of heat through a diabatic upward motion in the outer boundary layer. The particle finds its way into the inner boundary layer at last after a few transitions conserving the heat. The particle releases the heat through the diabatic downward motion in the inner boundary layer and goes back to the outer boundary layer.

We try to quantitatively relate the above Lagrangian illustration of the inward heat transport to the value of the flux obtained in Eulerian sense, 0.19 cm^3/s, as was shown in the preceding section with Fig. 13. The inward heat flux can be estimated in the Lagrangian sense as follows. Suppose that a unit volume of the fluid transports heat of $\Delta\Theta$ every T seconds in average. Since all the volume of the fluid per unit radian is $(b^2 - a^2)d/2$ (cm^3), total inward heat flux is obtained as;

$$\frac{\Delta\Theta}{T}\frac{(b^2 - a^2)d}{2}(\mathrm{cm}^3/\mathrm{s}). \tag{7}$$

When we suppose that the heat obtained in the outer boundary layer is transported into the inner boundary layer with its quantity conserved, $\Delta\Theta$ is estimated as 0.6 at least from Table 1. Since the particle goes back and forth between the side boundary layers more than 90 times during 100000s (Table 3), T is estimated as 100000s/90. Then we get the heat flux by Eq. (7),

$$0.16\mathrm{cm}^3/\mathrm{s}. \tag{8}$$

This is more than four-fifth of the value obtained in Eulerian sense. It is speculated that the computational error and the accumulation of heat transport with every cycle of motion in the trapped-regions account for the large part of this discrepancy.

The point is that heat is transported by the particle's warming in the outer boundary layer, its adiabatic movement across the interior region, and its cooling in the inner boundary layer. Through this description, jet streams merely play a role of the passage way of the particle across the interior region. It is concluded that the comprehension of the inward heat transport by every one cycle of wavy motion in the jet stream, which was mentioned in Section 1 with Fig. 3, is not appropriate for the steady wave in the rotating annulus of fluid.

Although zonal mean meridional circulation forms 3-cells circulation in the steady wave; two direct cells near the side boundaries and an indirect weak cell between the direct cells (see Fig. 4 in Williams, 1971 and Fig. 15 in Ukaji and Tamaki, 1989), cyclic route of the transition, as shown by the thick arrows in Fig. 12, implies the presence of direct one-cell circulation in Lagrangian sense.

5 Conclusion

Lagrangian motion of a fluid particle was investigated for a steady wave in a rotating annulus fluid. Obtained trajectory was plotted in a frame comoving with the steady wave. The trajectory shows a chaotic nature but has several typical organized behaviors depending on its position in the annulus. The annulus of fluid was divided into seven regions: an upper-level jet, a lower-level jet, a cyclonically trapped-region, an anticyclonically trapped-region, an inner boundary layer, an outer boundary layer, and a lower boundary layer. The upper-level (lower-level) jet is an untrapped region corresponding to the westerly (easterly) jet stream in the upper-level (lower-level), where the particle advects eastward (westward) and drifts inward (outward) gradually. The cyclonically trapped-region and anticyclonically trapped-region are trapped regions around the low pressure extreme and high pressure extreme, respectively. The particle spirals up and down in these regions. In the inner and outer boundary layers, the particle shows a large vertical movement. Cores of the cyclonically trapped-region and the anticyclonically trapped-region are nearly isolated from the others.

The particle motion during the whole period falls into the seven regions defined above and the number of appearance of each regime was counted. Four regions appear very frequently: the upper-level jet, the lower-level jet, the inner boundary layer, and the outer boundary layer. Average residence time of the particle in both the trapped-regions is longer than that in the other regions.

Frequency of the transition between regions are analyzed. A cyclic route of the transition, which is partly branches out into two routes, are remarkably preferred: the outer boundary layer $\rightarrow$ the upper-level jet $\rightarrow$ the inner boundary layer $\rightarrow$ the lower-level

jet *or* the lower boundary layer → the outer boundary layer.

Temperature of the fluid particle was investigated. The particle gets large quantity of heat in the outer boundary layer through diabatic upward motion and releases large quantity of heat in the inner boundary layer through diabatic downward motion. Temperature of the particle changes little in the other regions. Since there is not markable correlation between the temperature change and radial movement in both the jet regions, heat is not transported by every one cycle of the motion in the regions. There is a little correlation between them in both the trapped-regions, but its contribution to the total inward heat flux is very small.

In Lagrangian sense, the essence of the inward heat flux by the steady wave in the rotating fluid annulus is that the particle which obtains heat in the outer boundary layer goes nearly adiabatically across the interior region to the inner boundary layer and releases the heat there.

An estimation of the inward heat flux using frequency of the appearance of the side boundary layers and temperature change in the layers is comparable to the value calculated in Eulerian sense. Most of the heat transport is carried by the cyclic route via upper-level jet, lower-level jet, and the lower boundary layer.

Acknowledgments

We wish to thank Professor I.Hirota for his valuable comments and encouragement. We also wish to thank Drs. A. Numaguchi and M. Satoh for valuable advice. Thanks are due to Dr. S. Sakai for providing us with data. The GFD-DENNOU Library was used for drawing the figures.

References

Dombre, T., U. Frisch, J. M. Greene, M. Henon, A. Mehr and A. M. Soward, 1986 : Chaotic streamlines in the ABC flows. *J. Fluid Mech.*, **167**, 353–391.

Flierl, G. R., 1981 : Particle motions in Large-amplitude wave Fields. *Geophys. Astrophys. Fluid Dynamics*, **18**, 39–74.

Hide, R. and P. J. Mason, 1975 : Sloping convection in a rotating fluid. *J. Adv. Phys.*, **24**, 47–100.

Sakai, S., 1990 : (personal communication).

Sugata, S. and S. Yoden, 1993 : A numerical study on regime transitions of the rotating annulus flow with a semi-spectral model. *J. Meteor. Soc. Japan*, **71**, 491–501.

Ukaji, K. and K. Tamaki, 1989 : A comparison of laboratory experiments and numerical simulations of steady baroclinic waves produced in a differentially heated rotating fluid annulus. *J. Meteor. Soc. Japan*, **67**, 359–374.

Umino, W., S. Ueda, and M. Komabayashi, 1992 : *Earth Science (revised edition).* Tokyoshoseki Co. Inc.

Weiss J. B., and E. Knobloch, 1989 : Mass transport and mixing by modulated traveling waves. *Phys. Rev. A*, **40**, 2579–2589.

Williams, G. P., 1969 : Numerical integration of the three-dimensional Navier-Stokes equations for incompressible flow. *J. Fluid Mech.*, **37**, 727–750.

Williams, G. P., 1971 : Baroclinic annulus waves. *J. Fluid Mech.*, **49**, 417–449.

Williams, G. P., 1972 : The field distributions and balances in a baroclinic annulus wave.

Mon. Wea. Rev., **100**, 29–41.

Figure captions

Fig. 1. A streak photograph of trajectories of the suspended particles at a depth of 0.5 cm below the upper surface, taken from Hide and Mason (1975).

Fig. 2. Trajectories of particles projected onto a meridional plane obtained by tracing the motion of suspended balls of acrylic resin in the rotating annulus experiment performed by Sakai (1990). Marks ∘ and × indicate initial and final positions of the tracing particles, respectively. Dimensions of the annulus are $a = 3.5$ cm, $b = 7.5$ cm, and $d = 7$ cm.

Fig. 3. An illustration in a textbook of Earth science for high school students.

Fig. 4. Horizontal sections of (a) horizontal velocity fields, (b) vertical velocity (units: cm/s), (c) pressure divided by mean density (units: cm^2/s^2), (d) normalized temperature, and (e) horizontal velocity fields in the comoving frame. (I) $z/d = 3/4$ and (II) 1/8. Each section is described over two wavelengths in the azimuthal direction. Amplitudes of the unit vector and contour intervals are equal between sections for each variable.

Fig. 5. Projections of a trajectory of a fluid particle during 100000s onto (a) r-λ plane, (b) r-z plane, and (c) λ-z plane, where λ is the azimuthal position in the comoving frame. The particle is initially released at a cross mark.

Fig. 6. Trajectory divided into four different layers: $z/d =$ (a) 1 - 3/4, (b) 3/4 - 1/2, (c) 1/2 - 1/4, and (d) 1/4 - 0. Residence time in each level is indicated below each figure. Marks A and B indicate nearly-isolated areas.

Fig. 7. As in Fig. 6 except for seven sections by its radial position: $(r - a)/(b - a) =$ (a) 0 - 1/16, (b) 1/16 - 1/4, (c) 1/4 - 3/8, (d) 3/8 - 5/8, (e) 5/8 - 3/4, (f) 3/4 - 15/16, and (g) 15/16 - 1.

Fig. 8. Time variations of (a) radius r (units: cm), (b) azimuthal position in the comoving frame λ (units: rad), (c) height z (units: cm), (d) pressure divided by mean density p (units: cm^2/s^2), and (e) normalized temperature θ of the traced particle during t = 20000s – 40000s.

Fig. 9. Bird's-eye view of the trajectory for the upper-level jet and the lower-level jet. Labels correspond to times; t = (1) 25590s, (2) 25748s, (3) 25794s, (4) 26100s, (5) 26136s, and (6) 26260s. Each interval between the labels corresponds to; (1)–(2) the lower-level jet; (2)–(3) the outer boundary layer; (3)–(4) the upper-level jet; (4)–(5) the inner boundary layer; (5)–(6) the lower-level jet. Vertical lines are perpendicular lines drawn from the trajectory to the upper boundary or to the lower boundary every two seconds, whose direction is changed according to whether the height of the particle exceeds the half level or not.

Fig. 10. As in Fig. 9. except for the anticyclonically trapped-regime and the cyclonically trapped-region. Labels correspond to times; t = (a) 29148s, (b) 29676s, (c) 30904s, and (d) 31931s. Each interval between the labels corresponds to; (a)–(c) the anticyclonically trapped-region and (c)–(d) the cyclonically trapped-region. The mark (b) corresponds to the maximum height during the anticyclonically trapped-region. The trajectory between (b) and (c) is drawn by a broken line. Perpendicular lines are partly drawn to the lower boundary every two seconds during t = 29148s – 29246s, 30904s – 30992s.

Fig. 11. As in Fig. 9. except for the inner boundary layer → the lower boundary layer → the outer boundary layer. Labels correspond to times; t = (A) 28286s, (B) 28342s, (C) 28431s, and (D) 28492s. Perpendicular lines are drawn to the lower boundary every two seconds.

Fig. 12. Illustration of the transition of regions. Thick arrows indicate transitions whose count

exceeds 30. Thin arrows indicate the transition whose count exceeds 7.

Fig. 13. Radial distributions of inward heat flux per unit radian divided by fluid density and by specific heat; mean meridional circulation flux (solid line), deviatoric flux (long broken line), conductive flux (short broken line), and total flux (dash-dotted line).

Fig. 14. Time variations of (a) normalized temperature θ (solid line) and time-derivative of the temperature $D\theta/Dt$ (shaded zone), and (b) radius r (solid line) and height z (broken line) during t = 25000s–32000s. Vertical lines drawn in each figure indicate the times when the radius has the local maximum (solid line) or minimum (broken line). Triangle marks in the upside and downside of each figure indicate the time when the particle approaches maximumly close the outer and inner boundary, respectively, within 1/16 distance of width of the annulus from the boundaries. Labels **1**–**6**, **A**–**D**, and **a**–**d** corresponds to the labels in Figs.9, 11, 10, respectively.

Fig. 15. Bird's-eye view of the trajectory (thick line) of the particle in the lower-level jet during ∘ : 25327s–× : 25427s and □ : 25589s–△ : 25704s. Thin curved lines indicate the iso-therm lines at each radii. Perpendicular lines are drawn from the trajectories toward the iso-therm surface every one second. The trajectory is drawn by a solid line when the particle moves on this side of the iso-therm surface and by a broken line when on the opposite side.

	Appearance	Total residence (s)	Average residence (s)	Temp. change
Upper-level jet	101	21457	212.4	-0.04
Lower-level jet	64	19531	305.2	-0.01
Cyc. trapped	22	15732	715.1	0.12
Anticyc. trapped	34	26597	782.2	-0.04
Inner boundary	96	4907	51.1	-0.65
Outer boundary	103	8971	87.1	0.62
Lower boundary	36	2805	77.9	0.08
Sum	456	100000	219.3	

Table 1: Total number of appearance, total residence time, average residence time for one stay, and average of temperature change for one stay are shown for each regions.

		To						
		U.J	L.J	C.T	A.T	I.B	O.B	L.B	Sum
From	Upper-level jet	–	3	5	3	**88**	2	0	101
	Lower-level jet	1	–	4	0	2	**57**	0	64
	Cyc. trapped	2	4	–	4	4	8	0	22
	Anticyc. trapped	9	10	10	–	2	2	0	33
	Inner boundary	0	**47**	1	12	–	0	**36**	96
	Outer boundary	**88**	0	0	15	0	–	0	103
	Lower boundary	0	0	2	0	0	**34**	–	36
	Sum	100	64	22	34	96	103	36	455

Table 2: Transition matrix. The number of transitions from one region to another region is counted during the total periods.

		To		
		Inner boundary	Outer boundary	Sum
From	Inner boundary	5	91	96
	Outer boundary	90	12	102
	Sum	95	103	198

Table 3: Transition matrix but for the number of transitions concerning with the side boundary layers. Transitions are counted by focusing the layers only and neglecting the other regions.

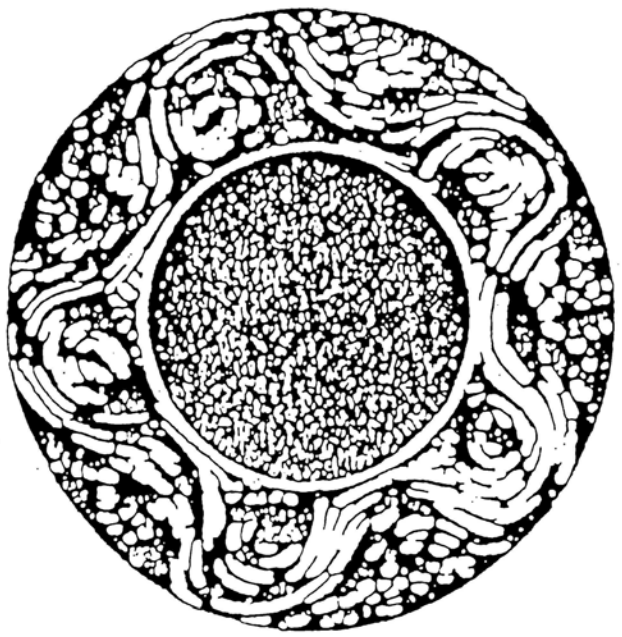

Fig. 1. A streak photograph of trajectories of the suspended particles at a depth of 0.5 cm below the upper surface, taken from Hide and Mason (1975).

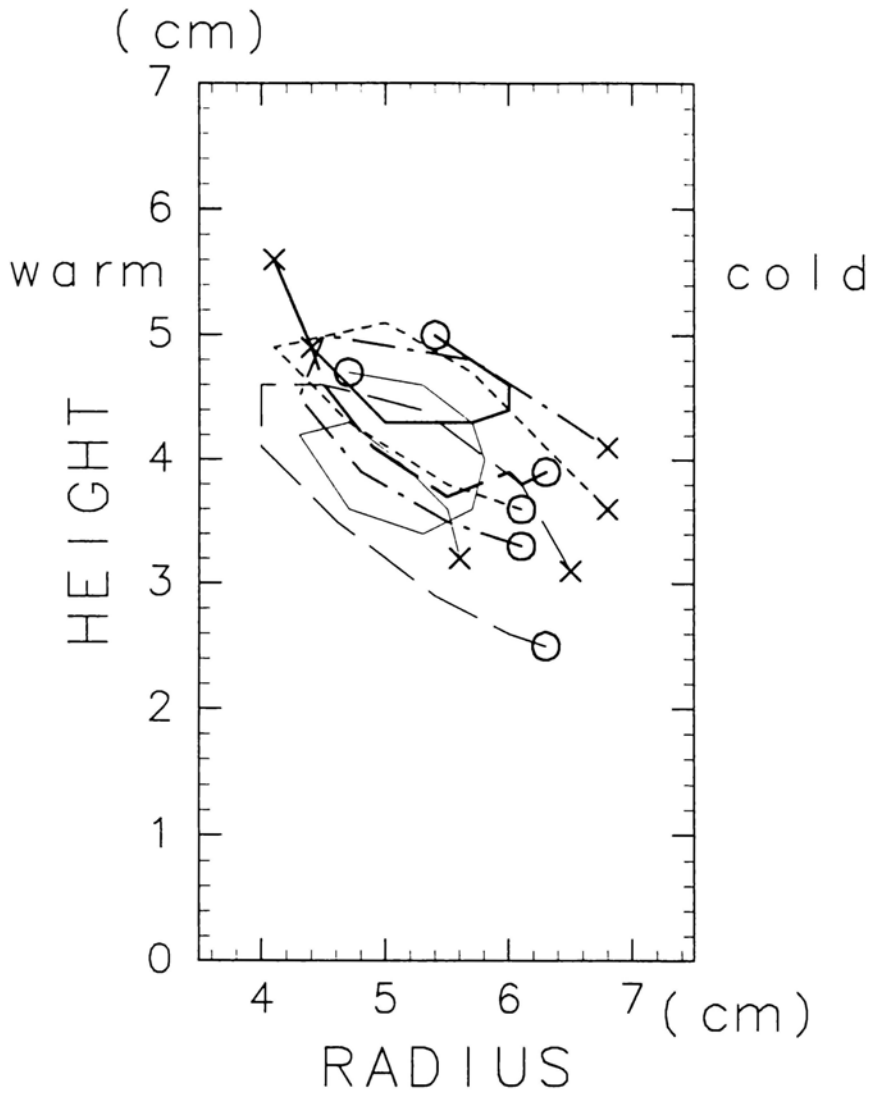

Fig. 2. Trajectories of particles projected onto a meridional plane obtained by tracing the motion of suspended balls of acrylic resin in the rotating annulus experiment performed by Sakai (1990). Marks ∘ and × indicate initial and final positions of the tracing particles, respectively. Dimensions of the annulus are $a = 3.5$ cm, $b = 7.5$ cm, and $d = 7$ cm.

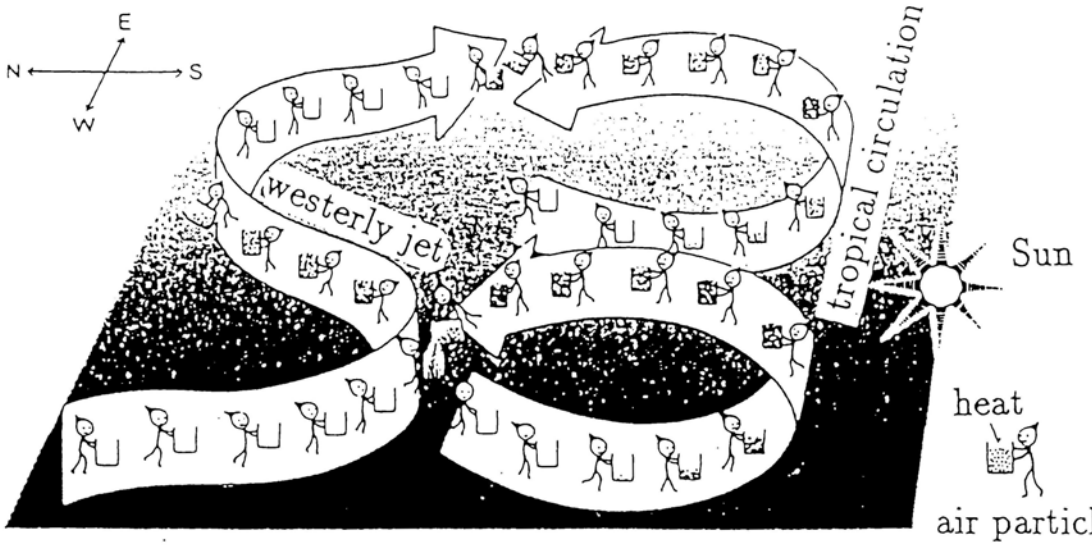

Fig. 3. An illustration in a textbook of Earth science for high school students.

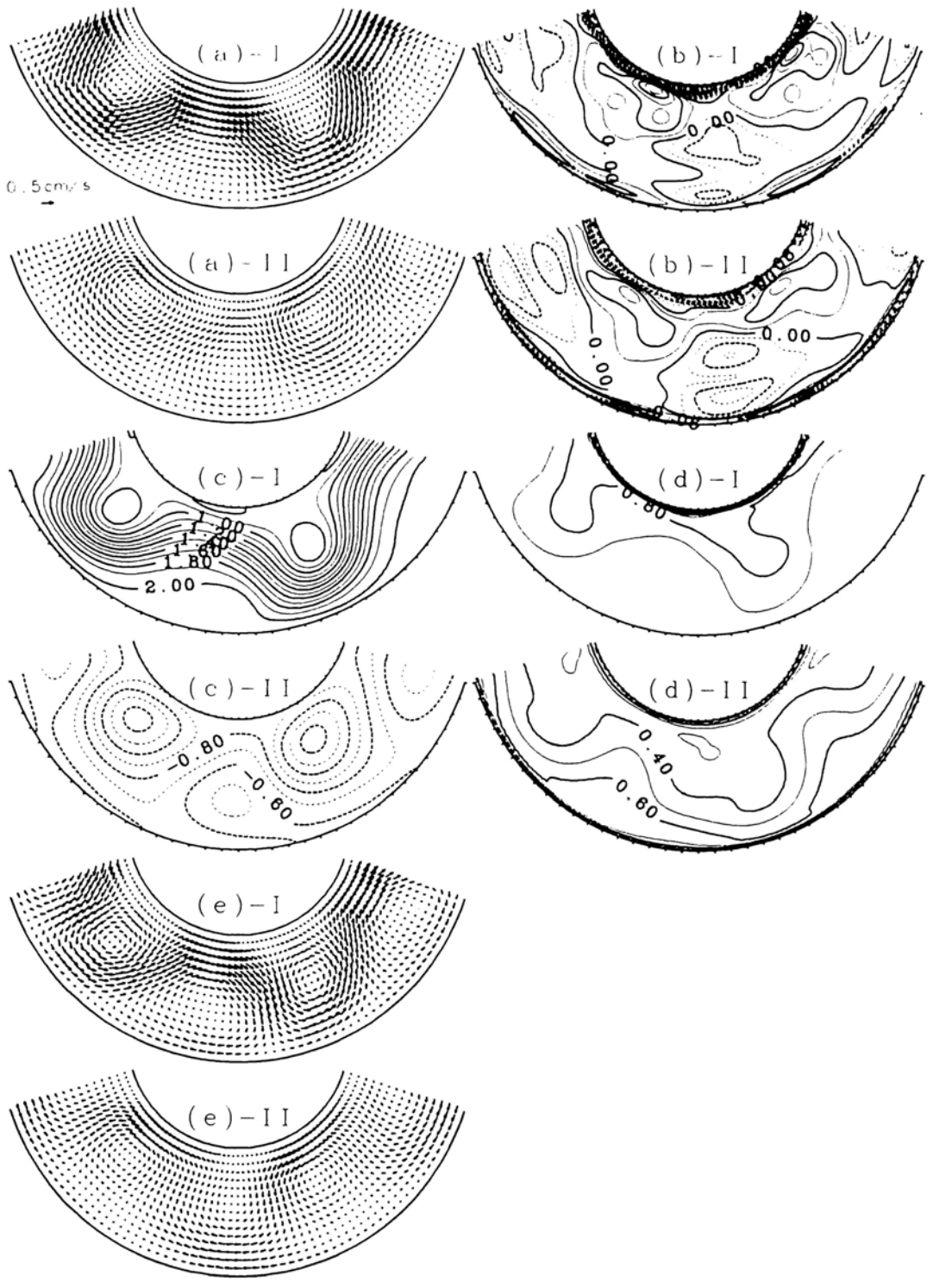

Fig. 4. Horizontal sections of (a) horizontal velocity fields, (b) vertical velocity (units: cm/s), (c) pressure divided by mean density (units: cm^2/s^2), (d) normalized temperature, and (e) horizontal velocity fields in the comoving frame. (I) $z/d = 3/4$ and (II) 1/8. Each section is described over two wavelengths in the azimuthal direction. Amplitudes of the unit vector and contour intervals are equal between sections for each variable.

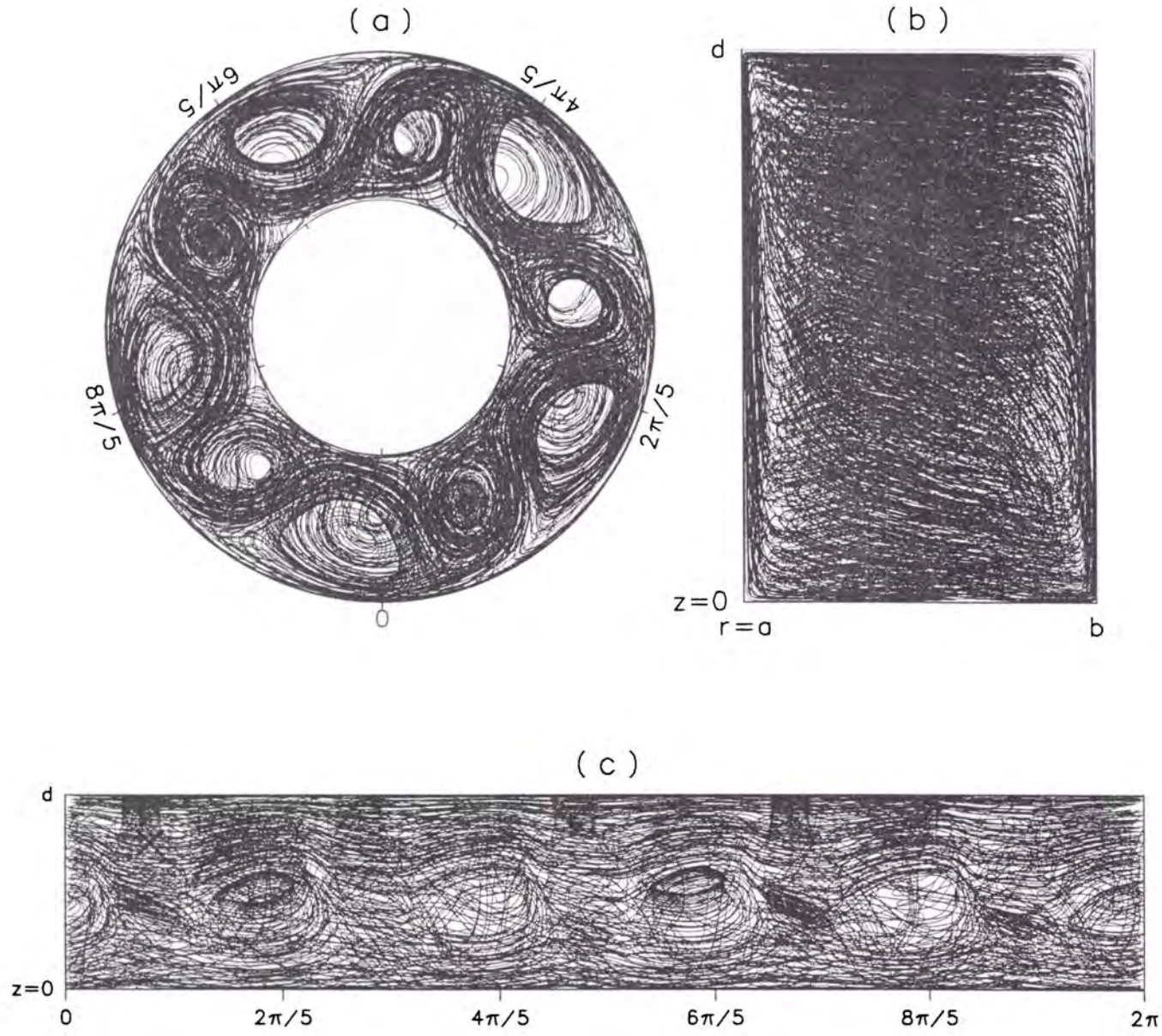

Fig. 5. Projections of a trajectory of a fluid particle during 100000s onto (a) r-λ plane, (b) r-z plane, and (c) λ-z plane, where λ is the azimuthal position in the comoving frame. The particle is initially released at a cross mark.

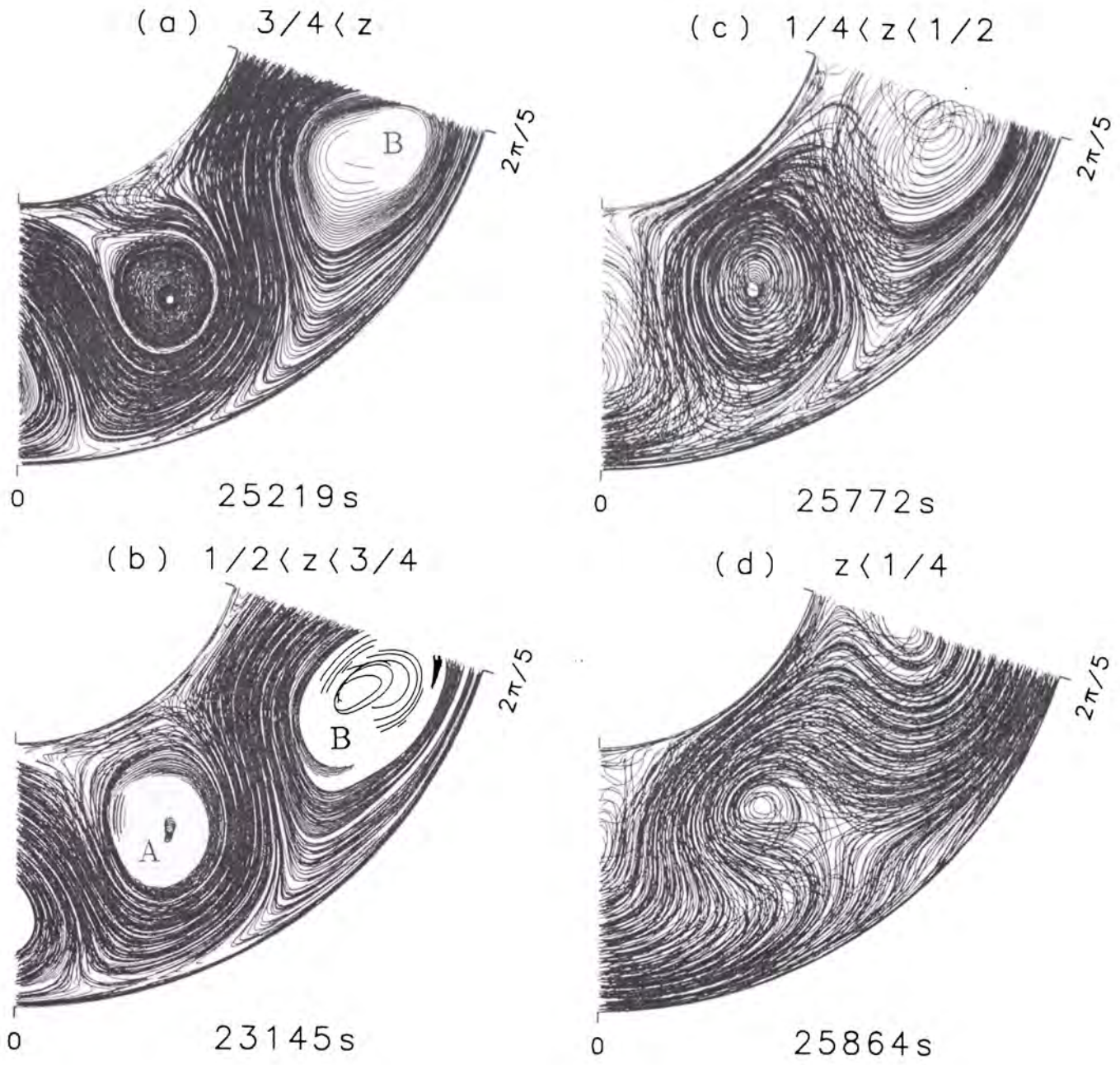

Fig. 6. Trajectory divided into four different layers: z/d = (a) 1 – 3/4, (b) 3/4 – 1/2, (c) 1/2 – 1/4, and (d) 1/4 – 0. Residence time in each level is indicated below each figure. Marks A and B indicate nearly-isolated areas.

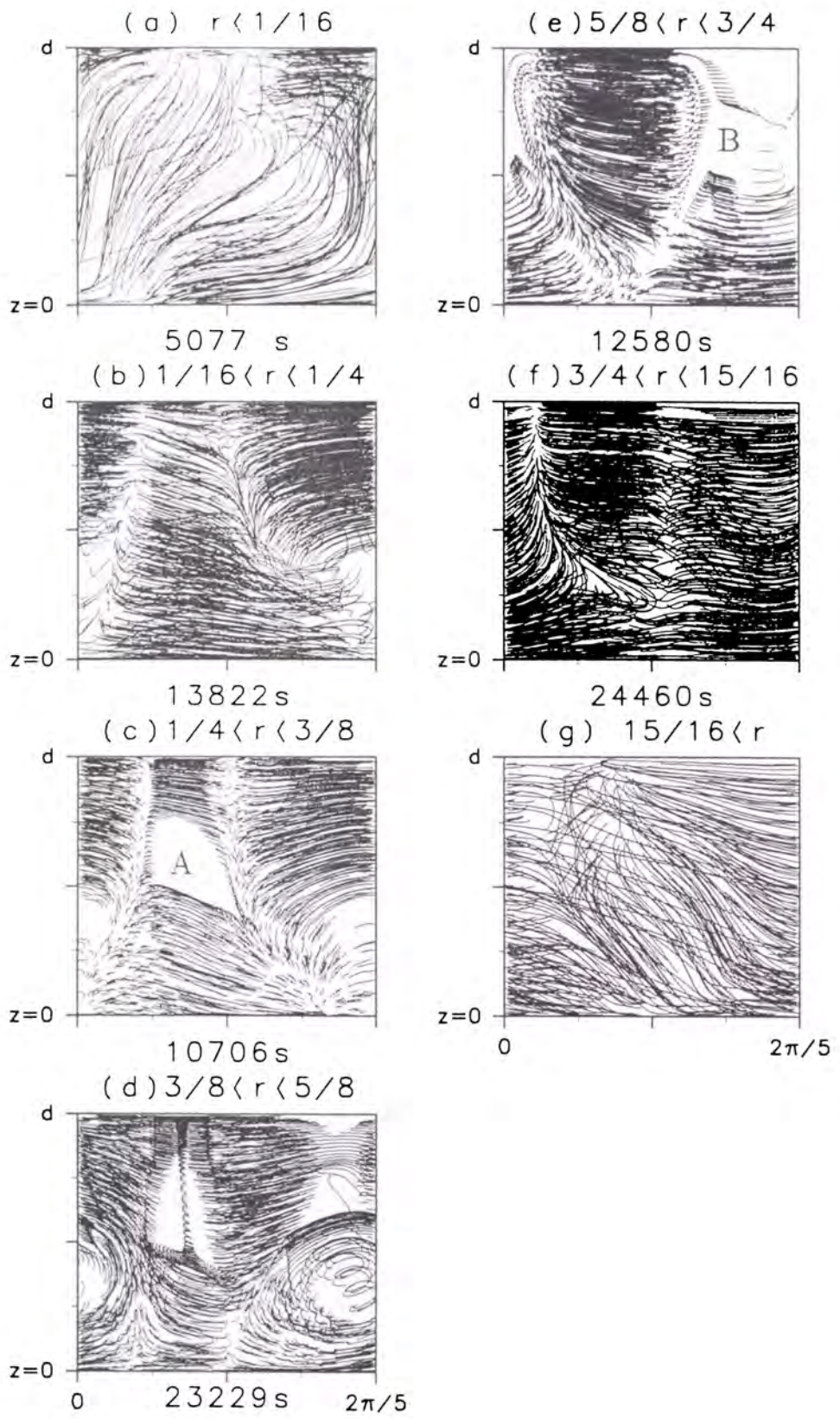

Fig. 7. As in Fig. 6 except for seven sections by its radial position: $(r-a)/(b-a)$ = (a) 0 – 1/16, (b) 1/16 – 1/4, (c) 1/4 – 3/8, (d) 3/8 – 5/8, (e) 5/8 – 3/4, (f) 3/4 – 15/16, and (g) 15/16 – 1.

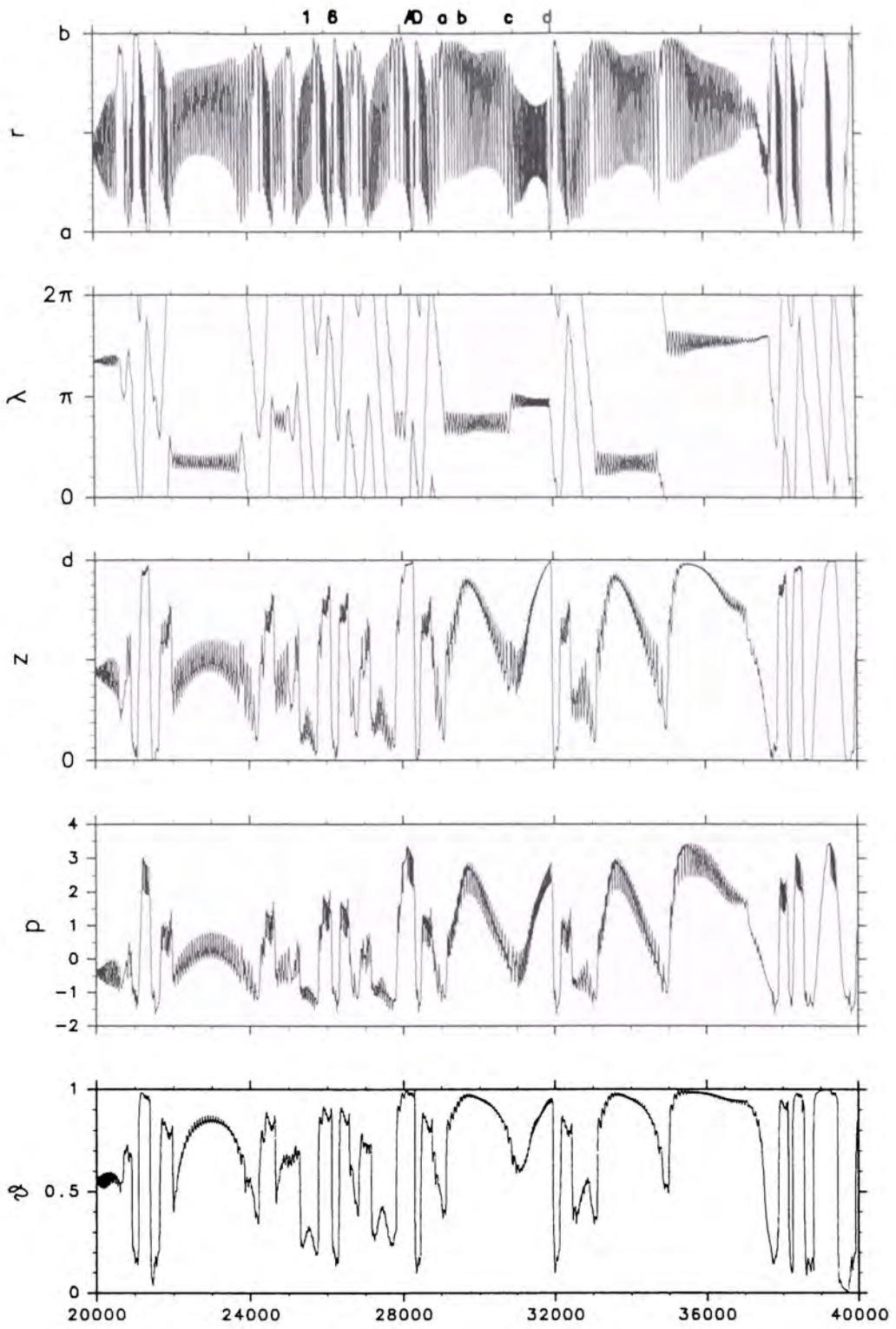

Fig. 8. Time variations of (a) radius r (units: cm), (b) azimuthal position in the comoving frame λ (units: rad), (c) height z (units: cm), (d) pressure divided by mean density p (units: cm^2/s^2), and (e) normalized temperature θ of the traced particle during t = 20000s – 40000s.

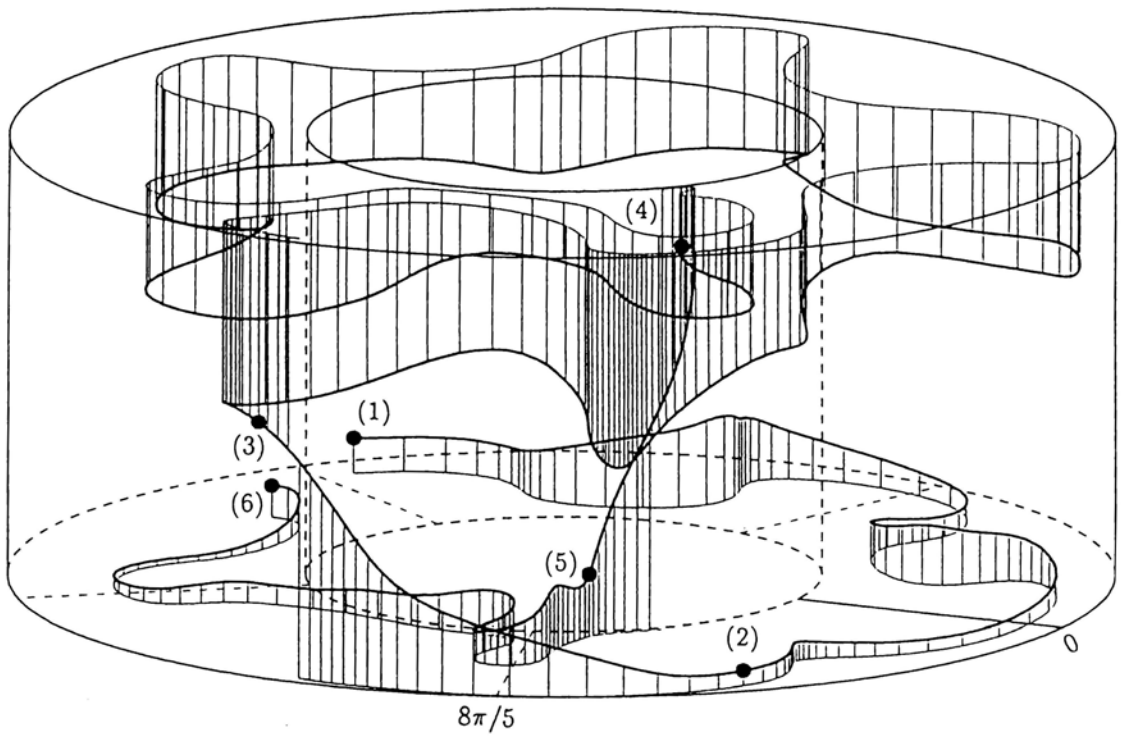

Fig. 9. Bird's-eye view of the trajectory for the upper-level jet and the lower-level jet. Labels correspond to times; t = (1) 25590s, (2) 25748s, (3) 25794s, (4) 26100s, (5) 26136s, and (6) 26260s. Each interval between the labels corresponds to; (1)–(2) the lower-level jet; (2)–(3) the outer boundary layer; (3)–(4) the upper-level jet; (4)–(5) the inner boundary layer; (5)–(6) the lower-level jet. Vertical lines are perpendicular lines drawn from the trajectory to the upper boundary or to the lower boundary every two seconds, whose direction is changed according to whether the height of the particle exceeds the half level or not.

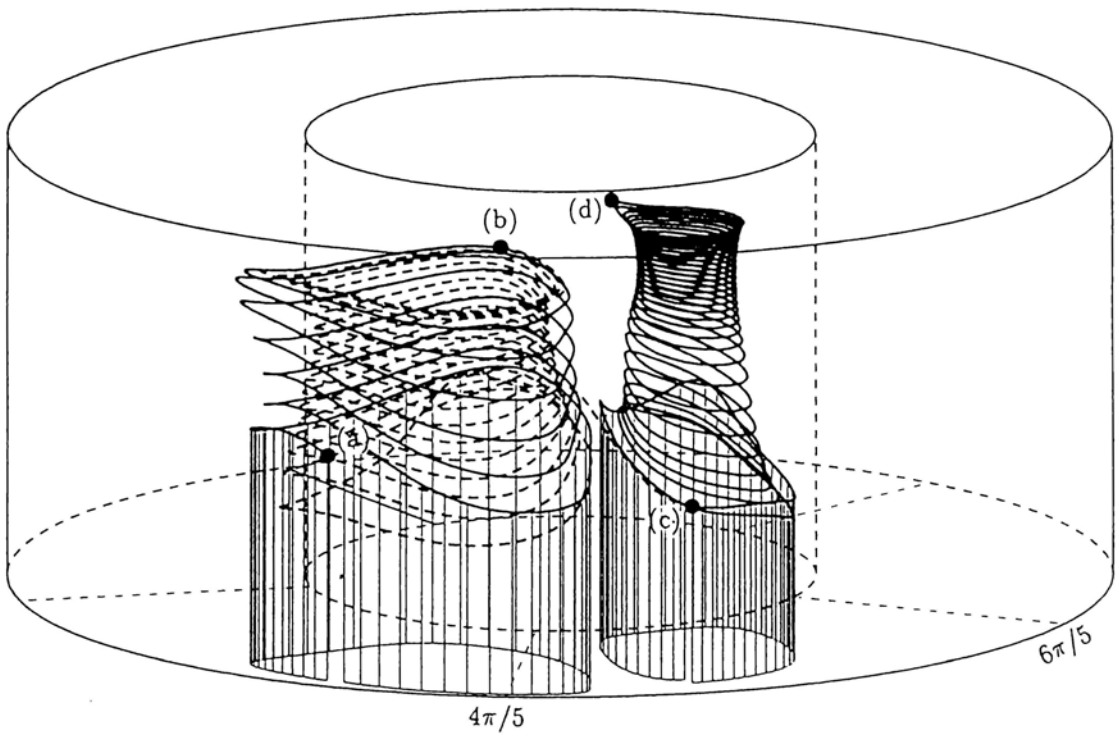

Fig. 10. As in Fig. 9. except for the anticyclonically trapped-regime and the cyclonically trapped-region. Labels correspond to times; t = (a) 29148s, (b) 29676s, (c) 30904s, and (d) 31931s. Each interval between the labels corresponds to; (a)–(c) the anticyclonically trapped-region and (c)–(d) the cyclonically trapped-region. The mark (b) corresponds to the maximum height during the anticyclonically trapped-region. The trajectory between (b) and (c) is drawn by a broken line. Perpendicular lines are partly drawn to the lower boundary every two seconds during t = 29148s – 29246s, 30904s – 30992s.

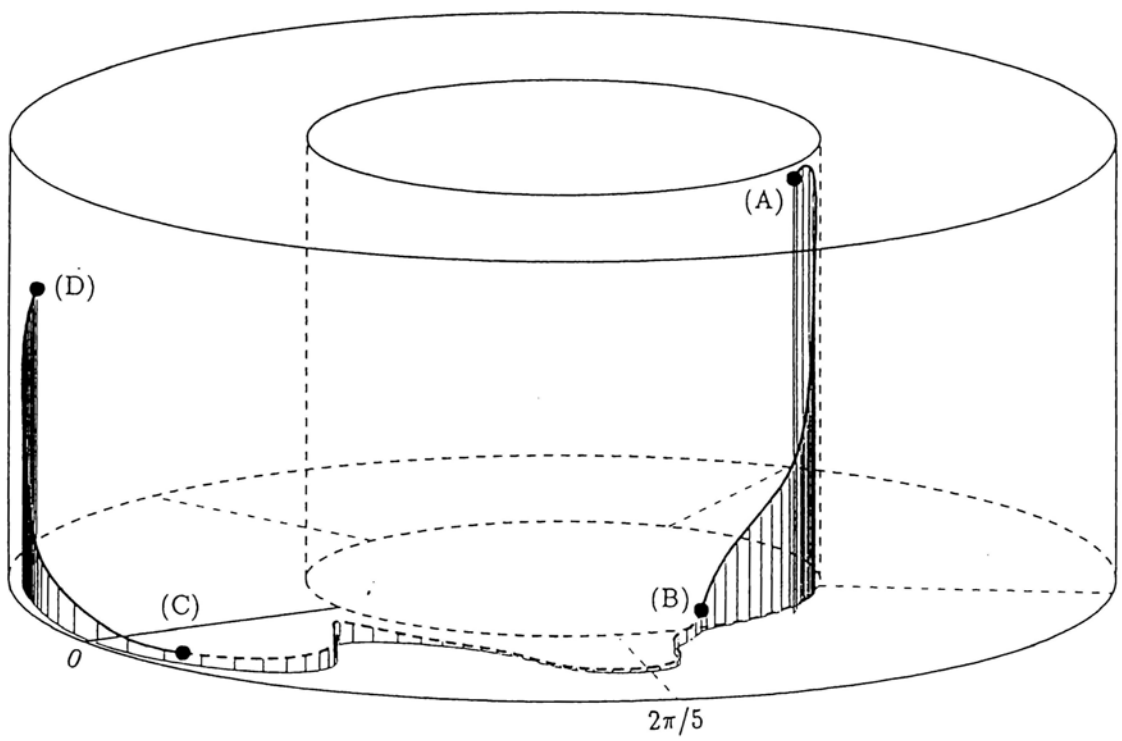

Fig. 11. As in Fig. 9. except for the inner boundary layer → the lower boundary layer → the outer boundary layer. Labels correspond to times; t = (A) 28286s, (B) 28342s, (C) 28431s, and (D) 28492s. Perpendicular lines are drawn to the lower boundary every two seconds.

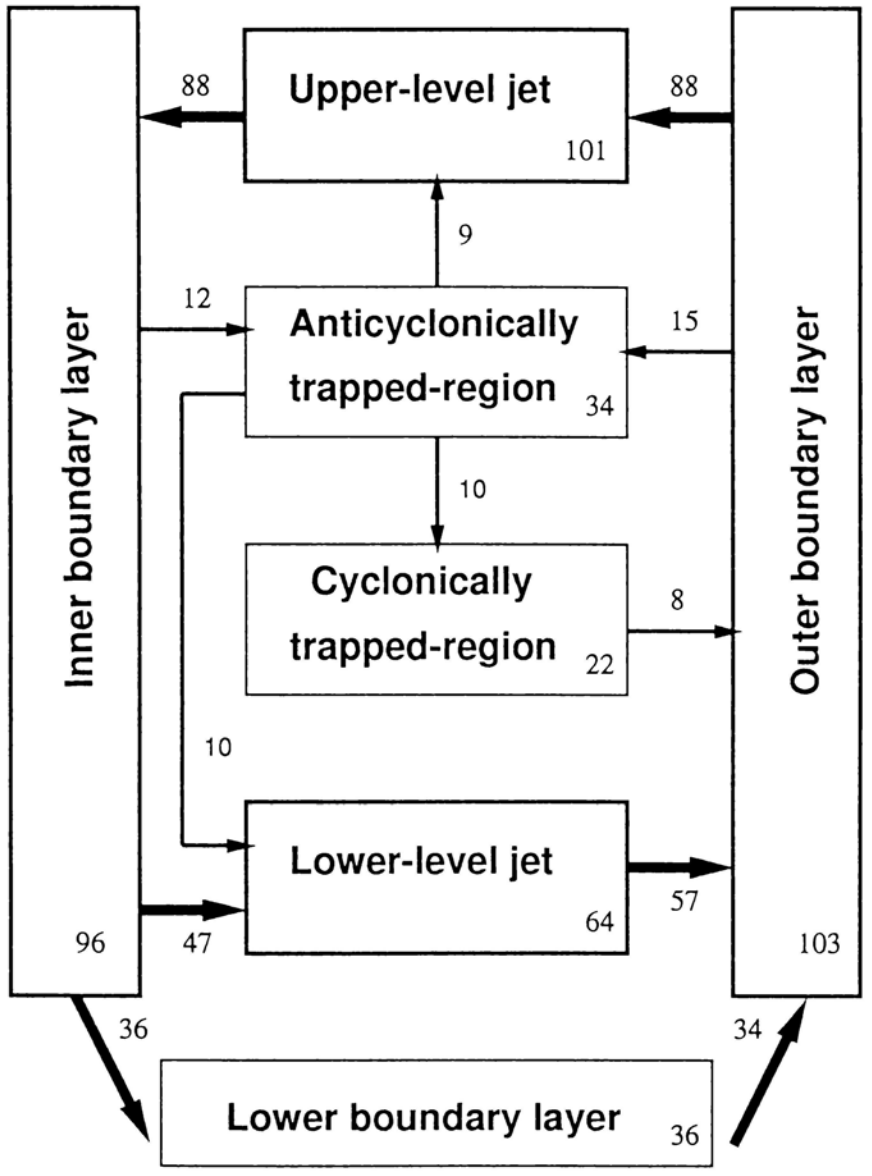

Fig. 12. Illustration of the transition of regions. Thick arrows indicate transitions whose count exceeds 30. Thin arrows indicate the transition whose count exceeds 7.

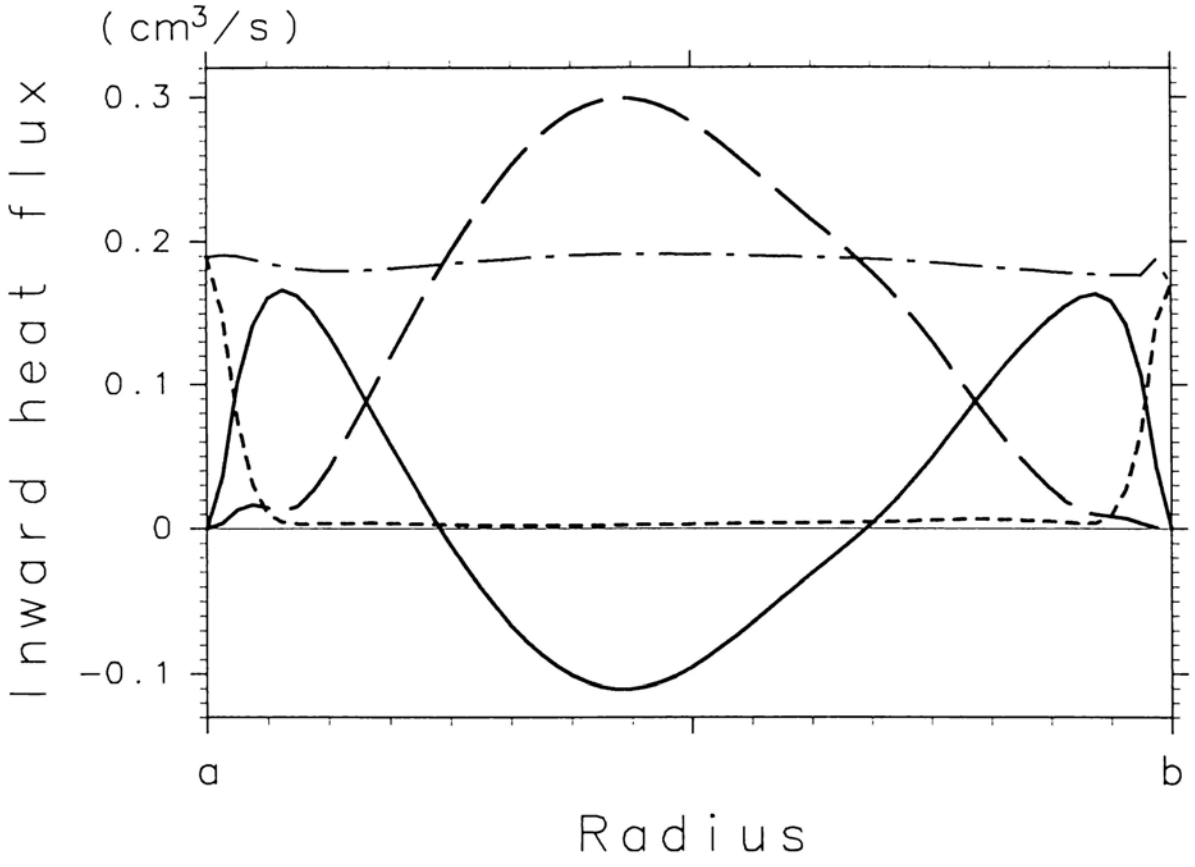

Fig. 13. Radial distributions of inward heat flux per unit radian divided by fluid density and by specific heat; mean meridional circulation flux (solid line), deviatoric flux (long broken line), conductive flux (short broken line), and total flux (dash-dotted line).

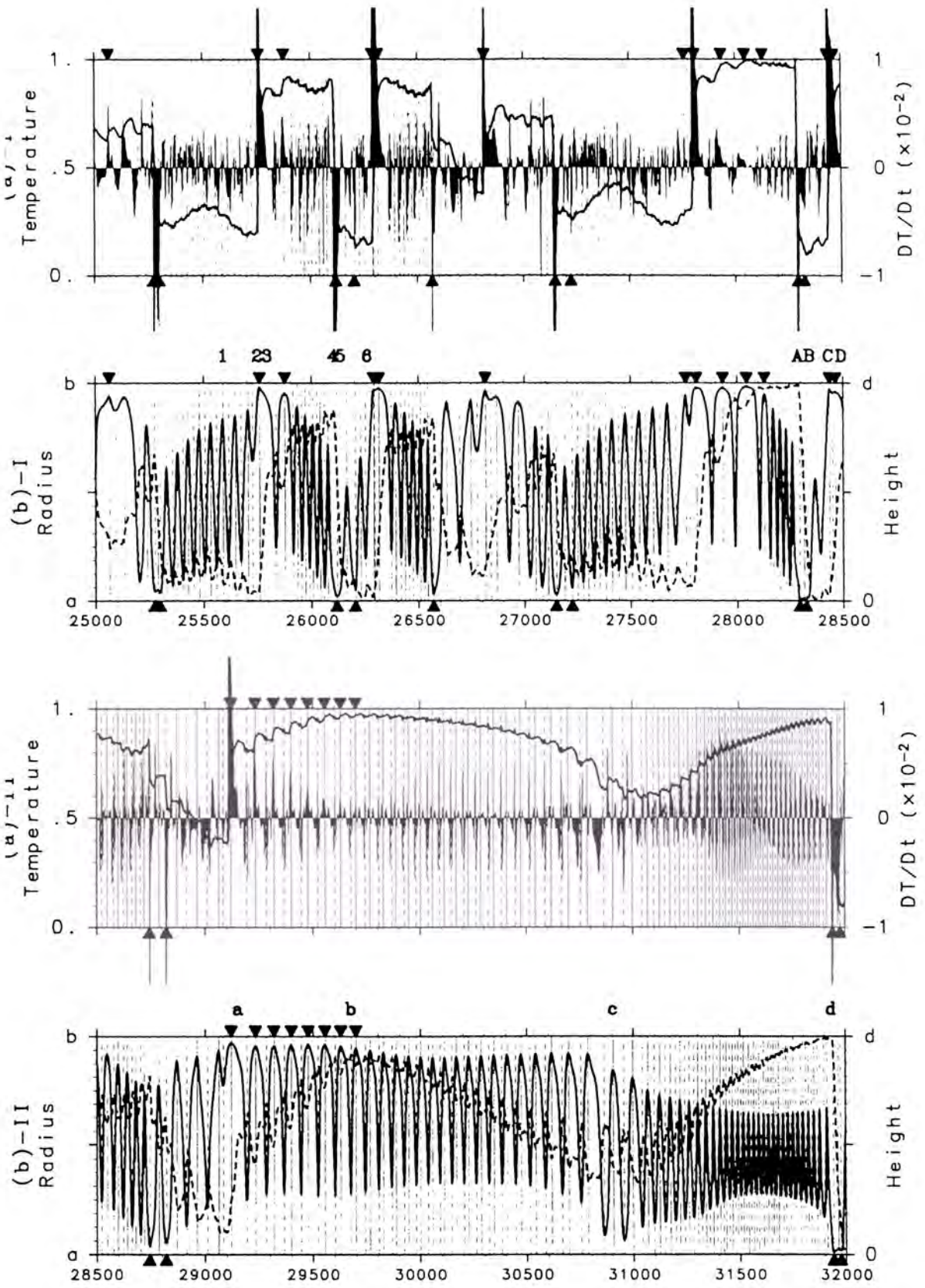

Fig. 14. Time variations of (a) normalized temperature θ (solid line) and time-derivative of the temperature $D\theta/Dt$ (shaded zone), and (b) radius r (solid line) and height z (broken line) during t = 25000s–32000s. Vertical lines drawn in each figure indicate the times when the radius has the local maximum (solid line) or minimum (broken line). Triangle marks in the upside and downside of each figure indicate the time when the particle approaches maximumly close the outer and inner boundary, respectively, within 1/16 distance of width of the annulus from the boundaries. Labels **1**–**6**, **A**–**D**, and **a**–**d** corresponds to the labels in Figs.9, 11, 10, respectively.

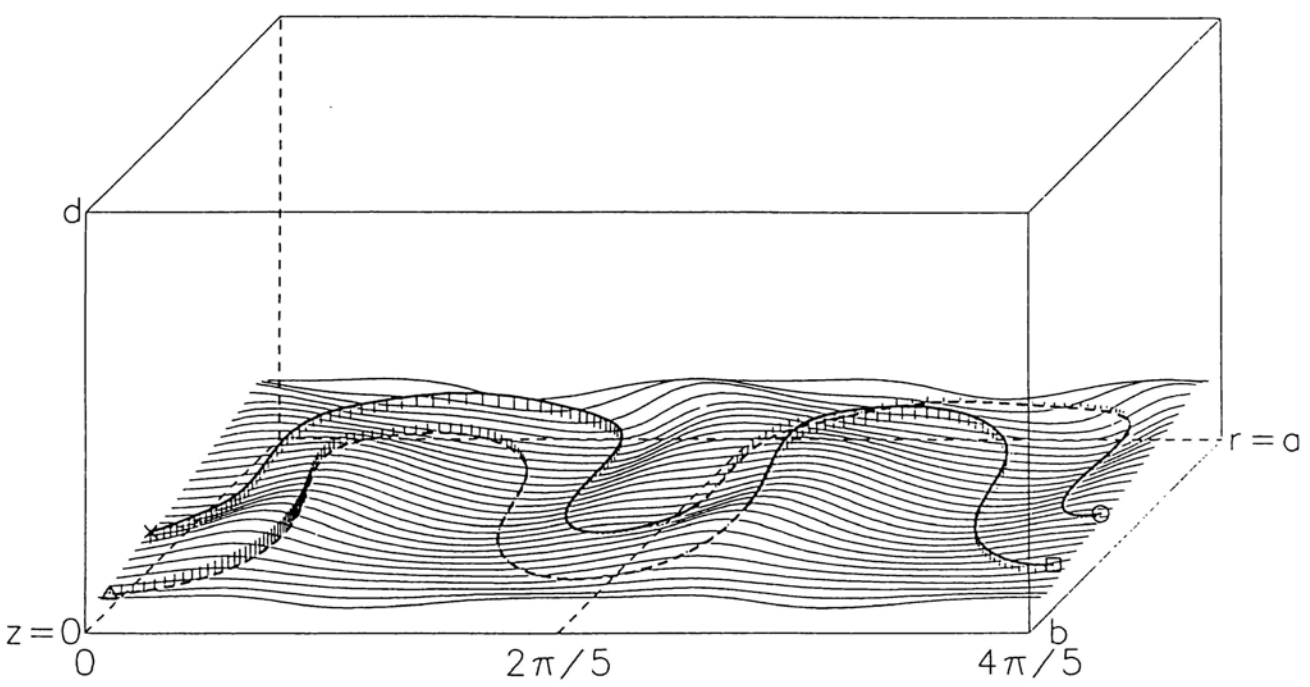

Fig. 15. Bird's-eye view of the trajectory (thick line) of the particle in the lower-level jet during ○ : 25327s–× : 25427s and □ : 25589s–△ : 25704s. Thin curved lines indicate the iso-therm lines at each radii. Perpendicular lines are drawn from the trajectories toward the iso-therm surface every one second. The trajectory is drawn by a solid line when the particle moves on this side of the iso-therm surface and by a broken line when on the opposite side.